A Search for R-Parity Violating Supersymmetric Particles at HERA using the ZEUS Detector

by

Raphael Galea

A thesis submitted in conformity with the requirements
for the degree of Doctor of Philosophy
Graduate Department of Physics
University of Toronto

Copyright © 2001 by Raphael Galea

Abstract

A Search for R-Parity Violating Supersymmetric Particles at HERA using the ZEUS Detector

Raphael Galea
Doctor of Philosophy
Graduate Department of Physics
University of Toronto
2001

Squarks produced via an R-parity violating interaction in e^+p collisions at a centre-of-mass energy of 300 GeV have been sought with the ZEUS detector at HERA. Squarks produced in e^+ quark fusion could decay to e-quark or gaugino-quark via a supersymmetric gauge decay, resulting in a final state with multiple jets and a lepton that could be a positron, electron ($e^\pm$) or a neutrino (ν). No evidence for squark production was found and limits were set on the R-parity violating coupling as a function of the squark mass and the SUSY parameters μ and M_2.

Dedication

For Nannu Kille.

Acknowledgements

Experimental High Energy physics is a collaborative effort and I must thank an enormous number of people. For this reason, should a name be missing in these acknowledgements, it will certainly be found in Appendix C which contains the author list for the ZEUS collaboration.

My thanks must first go to my advisor Dr. John Martin, whose unfailing support has been present throughout my studies. I am also grateful for the guidance of Dr. David Bailey and Dr. Mike Luke, and for the encouragement I received from Dr. Sampa Bhadra. Thank you, Dr. Bob Orr, for introducing me to the graduate program.

In Germany, I learned a great deal through collaboration with the past and present coordinators of the Exotics and Rare Phenomena Physics group: Dr. Stefan Schlenstedt, Dr. Masahiro Kuze, Dr. Roberto Sacchi, Dr. Luca Stanco and Dr. Bruce Straub. I worked closely with Dr. Stefan Polenz and benefited from his expertise and friendship. Thanks also to the other Canadian group Research Associates Dr. Bill Schmidke, Dr. Garry Levman and Dr. Gerd Hartner. Dr. Emmanuelle Perez deserves a great deal of credit for her pioneering work at H1 on this topic and her important contributions to the HERA Monte Carlo workshop.

Thanks must also go to the secretariat at DESY, Frau Bahr and Frau Bretzke. I am also grateful to Winnie Kam and Maianne Khurana at the University of Toronto Physics Department for their guidance and help throughtout my time in the School of Graduate Studies.

The Italian group at DESY were like family to me. I have to especially mention my house mates, Dr. Salvatore DePasquale, Dr. Stefano '*Nostro Huomo*' Dusini, Dr. Nicola '*Cippolone*' Coppola and of course Vincenzo, whose nickname is unprintable. Alberto, Silvia, Polini, Maria Carmela, Antonio, Enrico, Marta, Daniella, Davide and the rest of their compatriots never let me forget where I was born. There is life outside DESY and my friends Sonja, Kristina, Carsten, Petra, Dominik, Ida, GiGiLs and the Spanish crowd helped me to experience it.

I have to also thank Andreas '*THE OX*', my friend, house mate, and member of the Canadian group. Vielen Dank für alles. I must not forget to acknowledge the entire Canadian ZEUS cluster, it was truly a group which reflected Canada's cultural diversity. Marc, Pat, Laurel, Mohsen, Peter, Michael, Sanjay and Thorsten, I'll never forget the '*good old days*'.

To Christian, Steve, Ali, Daniel, Dr. Pepper and Sneaky Dees, we started and almost finished together. The 'Heir Apparent', Etienne, Amita and especially Amit helped me to remember to take time for myself.

Thanks to Gina and Alison for continually fine-tuning the Feng-shui in our house until this thesis was complete.

And finally I must thank my parents for providing me with all the necessary characteristics to succeed and enjoy my choices in life. Equally important to my success was my sister, Serena, whose support, emotionally, financially and otherwise has always been unyielding.

Fl-aħħar

Contributions to the ZEUS Experiment

I arrived at DESY to begin my work at the ZEUS experiment in September 1996. Upon arrival I worked on the Third Level Trigger (TLT). I became responsible for the maintenance and upgrade of the software and hardware for the TLT along with a Research Associate (RA) from the University of Toronto. I was on call during data taking for any online problems relating to the TLT. In the winter shutdown between 1996 and 1997, I helped in integrating a new architecture into the system and I performed a major reorganization of the monitor and filter software code. Over the years more demand has been made on the TLT in terms of processing power. Along with the RA, I ported many offline data quality checks to the TLT.

In 1997, I managed the Canadian cluster comprised of several platforms and operating systems. That same year I joined the Exotic and Rare Phenomena physics group. In 1998, I became the group's trigger representative. Along with my trigger responsibilities for the Exotics group, I initiated the Data Quality Monitoring (DQM) for the exotic physics triggers. In 1998, the DQM consisted of the Event of the Week (EOTW) project, in which the highest energy most interesting events are selected and scanned. In 1999, I implemented a simpler version of the EOTW selection code online, at the TLT, and created the Event of the Day (EOTD), which performs a real time exotic selection. This allows the two person shiftcrew an added visual opportunity to look at the data, which has made spotting potential detector problems easier.

I have represented the ZEUS and H1 collaborations at two international conferences, DIS99[1] and LLWI2000[2]. In 1998 I participated in the year long HERAMC[3] workshop in which I worked on generators of R-parity violating supersymmetry at HERA.

Finally, I participated and assisted in a meeting of the ZEUS collaboration in Toronto in June, 2000. I designed and managed the meeting web page and addressed any computing concerns of our collaborators.

Contents

1 Introduction **1**

2 The Standard Model **3**

2.1 Basic Elements of the Standard Model . . . 3

2.1.1 Generation of mass . . . 4

2.2 Problems with the Standard Model . . . 5

3 Phenomenology of Supersymmetry **6**

3.1 The Minimal Supersymmetric extension to the Standard Model (MSSM) . . . 7

3.1.1 Neutralino Sector . . . 8

3.1.2 Chargino Sector . . . 9

3.2 R-Parity . . . 10

3.3 Phenomenology of Supersymmetry at HERA . . . 12

3.3.1 Resonant production of Squarks . . . 12

3.4 Squark Decays . . . 15

3.4.1 $\not{R}_p$ Squark Decays . . . 16

3.4.2 R-parity conserving or Gauge Squark Decays . . . 17

3.5 Neutralino and Chargino Decays . . . 19

3.5.1 Neutralino Decays . . . 19

3.5.2 Chargino Decays . . . 20

3.6 Possible Final State Topologies . . . 21

3.7 Summary . . . 22

4 The Experimental Setup **25**

4.1 HERA: Hadron Elektron Ring Anlage . . . 25

4.2 The ZEUS Detector . . . 28

4.2.1 The Central Tracking Detector . . . 29

4.2.2 The Uranium Calorimeter . . . 30

4.2.3 Other Components . . . 33

4.2.4 The Luminosity Monitor . . . 34

4.3 Trigger and Data Acquisition System . . . 35

4.3.1 The First and Second Level Trigger . . . 35

4.3.2 The Third Level Trigger . . . 35

5 HERA Kinematics and Event Reconstruction **45**

5.1 Physics at HERA . . . 45

5.1.1 Deep Inelastic Scattering (DIS) . . . 45

5.1.2 Reconstruction of Kinematical Variables . . . 48

5.1.3 Reconstruction of Global Quantities . . . 49

5.2 Track and Vertex Reconstruction . . . 50

5.3 Corrections . . . 50

5.4 Electron/Positron Finding . . . 52

5.5 Jet Finding . . . 54

5.6 Squark Mass Reconstruction . . . 56

5.6.1 Channels with a $e^{\pm}$ in the final state . . . 56

5.6.2 Channels with a ν in the final state . . . 56

6 Monte Carlo Simulation **58**

6.1 Background Simulation . . . 58

6.2 SUSY Simulation . . . 59

6.3 Detector Simulation . . . 63

7 Event Selection **65**

7.1 Search Strategy . . . 65

7.2 Cut Optimization . . . 67

7.3 NC-like . . . 68

7.3.1 Preselection . . . 68

7.3.2 Further NC Selection . . . 69

7.3.3 Jet Cuts . . . 73

7.3.4 e jet Sample . . . 73

7.3.5 e jets Sample . . . 74

7.3.6 Selection Efficiencies and Squark Mass Resolutions . . . 76

7.3.7 Final NC-like Event Samples . . . 76

7.4 CC-like . . . 77

7.4.1 Cleaning cuts . . . 78

7.4.2 Selection cuts 81
7.4.3 Signal Enhancement 87

8 Limit Setting Procedure **90**
8.1 Inclusion of systematic uncertainties 91
8.2 Interpolation and limits in the SUSY phase space 91
8.3 Systematic Uncertainties 92

9 Results **95**
9.1 Limits 95
9.2 Other experiments 97

10 Conclusion **100**

A CC-like Cleaning Cuts **101**
A.1 Calorimeter Timing cuts 101
A.2 NC positron/electron criteria 102

B Branching Ratios and Signal Efficiencies **103**

C The ZEUS Collaboration **107**

D Glossary **114**

Bibliography **116**

List of Tables

2.1 The fermions of the Standard Model. 3
2.2 The bosons of the Standard Model. 4

3.1 Particle content of MSSM. 9
3.2 Squark production processes at HERA via $\not{R}_p$ λ'_{1jk} couplings with a positron beam. 14
3.3 Squark decay channels in $\not{R}_p$ SUSY which were considered. 23
3.4 Squark Decay Channels in $\not{R}_p$ SUSY classified by distinct topologies. 24

4.1 HERA design and 1997 running parameters. 26

5.1 Notation. 48

6.1 Summary of generated background Monte Carlo samples. 59
6.2 Summary of generated signal Monte Carlo samples with multijet final states. 60
6.3 Summary of generated signal Monte Carlo samples with single jet final states. 60

7.1 Summary of data sample event numbers and expectation from Monte Carlo background simulations for events with a reconstructed $e^{\pm}$. 77
7.2 Summary of the cleaning and selection cuts for the CC DIS sample. 83
7.3 Summary of data sample event numbers and expectation from Monte Carlo background simulations for events with $\not{P}_T$. 88

8.1 Summary of systematic uncertainties considered. 94

List of Figures

3.1 Radiative corrections to the Higgs mass in a supersymmetric model. 7
3.2 The evolution of the $SU(3)$, $SU(2)$, and $U(1)$ couplings in the (a) the Standard Model and (b) the Minimal Supersymmetric Extension to the Standard Model. 8
3.3 Neutralino masses given at fixed (a) $M_2 = 100$ GeV (b) $M_2 = 200$ GeV and $\tan\beta = 2$ as a function of μ. 10
3.4 Chargino masses given at fixed (a) $M_2 = 100$ GeV (b) $M_2 = 200$ GeV and $\tan\beta = 2$ as a function of μ. 11
3.5 Decay of a Proton via $LQ\bar{D}$ and $U\bar{D}\bar{D}$. 12
3.6 Interaction vertices via λ'_{ijk} couplings. 13
3.7 Production cross sections for $\tilde{u}_L$ and $\bar{\tilde{d}}_R$ for $\lambda' = 0.1$ in ep collisions. 15
3.8 Squark $\not{R}_p$ production and decay diagrams. 16
3.9 Regions in the SUSY phase space (M_2, μ) corresponding to a charged LSP and a neutral LSP dominated by its $\tilde{\gamma}$, $\tilde{Z}$ or $\tilde{H}^0$ components, for $\tan\beta = 2$. . 18
3.10 Dominant gauge decay mode for a 150 GeV $\tilde{u}_L$ squark in the phase space plane (M_2, μ) for $\tan\beta = 1$. 19
3.11 Representative diagrams from the $\not{R}_p$ decay of the $\tilde{\chi}^0_n$ for a non-zero λ'_{ijk}. . . 20
3.12 Gauge Decays of the $\tilde{\chi}^0_n$. 21
3.13 Gauge decay modes for the $\tilde{\chi}^\pm_n$. 22

4.1 Layout of the HERA accelerator complex and injection system. 25
4.2 The integrated luminosity recorded by HERA for 1992-2000. 28
4.3 Cutaway view of the ZEUS detector. 29
4.4 One octant of the CTD showing the field and sense wires. 30
4.5 The ZEUS calorimeter (y-z projection). 33
4.6 The Layout of the ZEUS luminosity monitor. 34
4.7 Schematic diagram of the ZEUS trigger and data acquisition system. 36
4.8 The TLT hardware design. 37
4.9 The TLT software design. 38

4.10 Flow chart outlining the TLT trigger decision. 40
4.11 Time measurements for ep and beam-gas interactions. 41
4.12 Time distributions of RCAL times versus the FCAL minus RCAL time. . . . 42
4.13 Examples of cosmic and halo muons in the ZEUS detector. 43
4.14 The CPU processing time required by the TLT. 44

5.1 A schematic view of the Deep Inelastic Scattering Process at HERA. 45
5.2 A schematic view of the s-channel resonance production at HERA. 47
5.3 Display of a charged current Monte Carlo event. 52
5.4 y_{JB} as compared to $y_{regularized}$ for a high Q^2 charged current Monte Carlo sample. 53
5.5 The positron finding efficiency as a function of energy, polar angle and $\log_{10}(Q^2)$. 55

6.1 Examples of leading order diagrams for (a) direct and (b) resolved photoproduction processes. 61
6.2 Graphical view of the generated signal Monte Carlo sets in the gaugino mass space. 62
6.3 Effect of initial and final state parton showers on the mass reconstruction of a 200 GeV squark undergoing the $\not{R}_p$ decay $\tilde{q} \to eq$. 63
6.4 $\sigma(e^+d \to q\tilde{\chi}^0_1)$ as a function of the SUSY parameter μ for fixed M_2 and fixed squark mass. 64

7.1 Jet distributions for Monte Carlo signal simulations with $e^\pm$ and multijet topologies. 66
7.2 Jet distributions for Monte Carlo neutral and charged current background simulations. 67
7.3 Jet distributions for Monte Carlo signal simulations for e and single jet topologies. 68
7.4 Jet Distributions for the preselected data sample. 70
7.5 Kinematic distributions for the preselected data sample. 71
7.6 $\log_{10}(Q^2)$ and reconstructed mass distributions for the preselected data sample. 72
7.7 The E_T distribution of the highest E_T jet as a function of the invariant mass of the e + jet(s) system. 74
7.8 (a) The y distribution for neutral current DIS compared to a sample cascade decay (e jets) and a sample $\not{R}_p$ decay (e jet. (b) The y distribution as a function of the invariant mass. 75

7.9 The $\log_{10}(Q^2)$ distribution for neutral current DIS compared to that of a cascade squark. 76
7.10 The experimental efficiencies for squark decays as a function of squark mass. 77
7.11 The mass resolution for squark decays as a function of squark mass. 78
7.12 The reconstructed mass distribution for the e jet final sample. 79
7.13 The reconstructed mass distribution for the e^+ jets final sample. 80
7.14 Distributions of events in the (number of good tracks)-(number of all tracks) plane. 83
7.15 The (a) $\not{P}_T(-1ir)$ and (b) $\not{P}_T$ distributions before the application of their selection. 84
7.16 Control plots comparing data and Monte Carlo background simulation expectation for the number of good jets, y, $\not{P}_T$ and E_T distributions after preselection. 85
7.17 Control plots comparing data and Monte Carlo background simulation expectation for the $\log_{10}(Q^2)$ and invariant mass distributions after preselection . 86
7.18 (a) The efficiencies and (b) resolutions for cascade squark decays into ν jets as a function of the squark mass. 88
7.19 The reconstructed mass distribution for the ν jets final sample. 89

8.1 The systematic uncertainty of variation of the selection cuts on the selection efficiency. 93

9.1 λ'_{1j1} limits as a function of $M_{\tilde{q}}$ for fixed $M_2 = 290$ GeV, $\mu = -200, 200$ GeV and $\tan\beta = 2$. 96
9.2 The 95% CL upper limit on λ'_{1j1} in the SUSY parameter (M_2, μ) space for $M_{\tilde{q}} = 200$ GeV. 97
9.3 95% CL exclusion upper limits on the $\not{R}_p$ coupling λ'_{ijk} as a function of the squark mass. 98
9.4 Diagram for the selection squark production process at HERA. 99

B.1 Branching ratios at fixed $M_2 = 90$ GeV, $\mu = -200$ GeV and $\tan\beta = 2$. . . . 104
B.2 Branching ratios at fixed $M_2 = 190$ GeV, $\mu = -200$ GeV and $\tan\beta = 2$. . . . 104
B.3 Branching ratios at fixed $M_2 = 240$ GeV, $\mu = 100$ GeV and $\tan\beta = 10$. . . . 105
B.4 Branching ratios at fixed $M_2 = 290$ GeV, $\mu = 200$ GeV and $\tan\beta = 10$. . . . 105
B.5 Efficiency as a function of squark mass at fixed $\tan\beta = 2$ and $\mu = -200$ GeV 106
B.6 Efficiency as a function of squark mass at fixed $\tan\beta = 10$ and $\mu = 200$ GeV 106

Chapter 1

Introduction

In 1999, I presented a preliminary study of this analysis along with other exotic particle searches performed at ZEUS [1], at the Workshop on Deep Inelastic Scattering in Berlin, Germany. At the conference dinner, I was sitting along side a senior member of our collaboration. He asked me what the topic of my thesis was and I told him that I was looking for Supersymmetry. To this I received the comment *"SUSY (Supersymmetry) is the only model which has survived over 25 years without a single piece of experimental proof".*

The point is well taken in the context of the great accomplishments by theorists and experimentalists in the field of particle physics. The Standard Model (SM) of particle physics, which is briefly discussed in chapter 2, has been the culmination of the successes of the field and has been able to explain a wealth of precise experimental data. The discovery of the top quark[4] and first direct observation of the tau neutrino[5] have filled in the last gaping holes of the SM particle spectrum, with one exception. This is the important Higgs particle which by most indications seems to be right around the proverbial corner. Existing measurements have already ruled out the Higgs particle up to a mass of 108 GeV[6] and the Tevatron run II and anticipated experiments at the planned Large Hadron Collider (LHC) are expected to discover the Higgs particle or push its mass limit to up to the level of 1 TeV[7].

Despite its success, the SM is not a Theory of Everything (TOE). There are experimental data[8] which suggest that neutrinos have mass, which is strictly not a part of the SM, by design. The SM and some other shortcomings of the SM are outlined in chapter 2. One proposed answer to physics beyond the SM is SUSY. A minimal supersymmetric model's most dramatic effect is in doubling the known particle spectrum. Each fermion in the SM has a scalar superpartner and each boson has a fermionic superpartner. SUSY searches have been performed at all the major experiments around the world and the search for SUSY at HERA is the topic of this thesis. HERA (see chapter 4) has a unique opportunity to test SUSY models involving the concept of $R-$parity violating ($\not{R}_p$) supersymmetric quarks

(squarks). The search for $\not{R}_p$ squarks is promising at HERA because they can be produced right up to the kinematical limit (300 GeV). This phenomenology is described in chapter 3. In the search described in this thesis, no signal is observed for the production of $\not{R}_p$ squarks in 47.7 pb^{-1} of e^+p data taken by the ZEUS experiment from 1994-1997. Chapters 5 and 6 describe the tools and methods by which data is reconstructed and in chapter 7 the event selection is explained. Limits are set on the strength of $\not{R}_p$ couplings as a function of the squark mass and parameters which define the models under study. Chapter 8 outlines the methodology used in the setting of the limits. The results and their discussion can be found in chapters 9 and 10.

I can understand the frustration expressed by my senior collaborator because this SUSY search does not rule out a model but instead only sets limits. This is preparatory work for the upcoming experiments which will further push the frontiers of the SM and perhaps begin to rule out or confirm SUSY models. To answer the comment regarding lack of experimental evidence for SUSY, I responded with an anonymous quote: *"The pessimist would say that no SUSY particles have been discovered. The optimist would say that half of them have".*

Chapter 2

The Standard Model

Particle physics phenomena are extremely well described within the SM of elementary particles and their fundamental interactions. The SM provides an elegant theoretical framework which has successfully passed very precise tests, some of which like $\sin\theta_W = 0.23147(16)$ have reached the level of 0.1% [9].

2.1 Basic Elements of the Standard Model

The SM describes elementary particles as the point-like constituents of matter. There are two types of basic building blocks, the matter particles and the interaction particles. The matter fields are fermions of spin 1/2 and are classified into leptons and quarks grouped into three generations. They are summarized in table 2.1. The leptons have integral charge and

Generation	Quarks	Charge (e)	Leptons	Charge (e)
1	up u	2/3	electron-neutrino ν_e	0
	down d	-1/3	electron e	-1
2	charm c	2/3	muon-neutrino ν_μ	0
	strange s	-1/3	muon μ	-1
3	top t	2/3	tau-neutrino ν_τ	0
	bottom b	-1/3	tau τ	-1

Table 2.1: *The fermions of the Standard Model and their principal characteristics.*

the quarks have fractional charge.

The quarks have an additional quantum number called colour, which comes in three varieties. The quarks must be confined into the experimentally observed matter particles,

called hadrons, which are colourless. These colourless composite particles are classified into baryons, fermions made up of three quarks, and mesons, bosons (integral spin particles) made up of one quark and one anti-quark.

All interactions in the SM are mediated by the exchange of one of several interaction particles, which are elementary bosons. These particles and the forces they mediate are summarized in table 2.2.

Interaction	Bosons	spin	Charge (e)	Mass (GeV)
Electromagnetic	photon γ	1	0	0
Weak	$W^{\pm}$	1	$\pm$ 1	80.2
Weak	Z^0	1	0	91.2
Strong	gluons g_i $(i = 1..8)$	1	0	0

Table 2.2: *The bosons of the Standard Model and their principal characteristics*[9]. *Throughout this thesis the convention of natural units ($c = \hbar = 1$) is applied.*

The SM is a quantum field theory (QFT) based on the gauge symmetry $SU(3) \times SU(2) \times U(1)$. This group includes the symmetry group of the strong interaction, $SU(3)$. This theory is known as Quantum Chromo Dynamics (QCD). The symmetry group of the electromagnetic interaction, $U(1)$, is a subgroup of $SU(2) \times U(1)$, the gauge group for the electroweak theory of Glashow, Weinberg and Salam[10, 11, 12], which unifies the electromagnetic and weak sectors.

2.1.1 Generation of mass

If the symmetry $SU(2) \times U(1)$ were unbroken, the $W^{\pm}$ and Z^0 would be massless which is not the case. If mass terms were added to the SM lagrangian, the theory's gauge invariance would be lost. Instead a scalar particle, the Higgs boson (H), is added to the theory. Through a mechanism called spontaneous symmetry breaking, the Higgs boson generates the particle masses while preserving the gauge invariance of the theory.

One assumes the scalar particle H, which is electrically neutral, appears as a doublet of $SU(2)$ and has Yukawa couplings to both gauge bosons and fermions. The SM potential is chosen such that at the minimum, the H has a non-zero mass in the vacuum. The symmetry $SU(2) \times U(1)$ is spontaneously broken and the particles acquire a mass.

Several of the SM particles in tables 2.1 and 2.2 were predicted long before their discovery, and are therefore testaments to the success of the SM. These include the gluon at Deutsches Elektronen-SYnchrotron (DESY), the W and Z bosons at Centre European

Recherche Nucléaire (CERN) and the *top* quark and τ neutrino at Fermilab. Only the Higgs boson has not yet been observed.

2.2 Problems with the Standard Model

The SM has been tested thoroughly by many particle physics experiments. Yet, without the discovery of the Higgs boson it is still incomplete. There are also other theoretical aspects of the theory which make most believe that it is not the final chapter of particle physics:

- Hierarchy Problem
  Why is the weak scale so small compared with the scale of Grand Unified Theories (GUTs): $M_W \sim 10^{-17} M_{Planck}$?

- Fine-Tuning Problem
  Radiative corrections to the Higgs boson masses have quadratic divergences. The corrections to the Higgs masses are many orders of magnitude larger than the Higgs mass itself. These divergences can be renormalized away by careful adjustment of corrections and this must be done to all orders in perturbation theory.

- Unification of couplings.
  In a gauge theory the couplings scale with energy. A necessary requirement of all GUTs is that these couplings meet at a single point. After precise measurements of the $SU(3) \times SU(2) \times U(1)$ couplings, and the extrapolation of these couplings to high energies, unification has been excluded by more than eight standard deviations[13].

- Gravity
  Gravity, along with the electromagnetic, weak and strong forces, make up the four fundamental forces of nature. Gravity is conspicuous by its absence in the SM.

Chapter 3

Phenomenology of Supersymmetry

One of the problems alluded to in section 2.2 was the problem of *fine-tuning*: if the fermion and scalar couplings of the theory are carefully adjusted, it is possible to cancel the quadratically divergent contributions to the Higgs mass. A symmetry can be imposed on the theory which results in this cancellation to occur to all orders in perturbation theory [14]. It is this symmetry which is referred to as *supersymmetry*.

Supersymmetry (SUSY) relates the masses and couplings of particles with different spins. SUSY is a leading contender for an extension to the SM. It is a generalization of the space-time symmetries of Quantum Field Theory (QFT) that transform fermions into bosons and bosons into fermions. SUSY therefore groups particles with the same mass and other quantum numbers, but which differ by $\pm 1/2$ unit of spin, into a *superfield*.

$$Q|fermion\rangle = |boson\rangle, \quad Q|boson\rangle = |fermion\rangle, \tag{3.1}$$

where Q are fermionic generators which satisfy:

$$\{Q, \bar{Q}\} = -2\gamma_\mu P^\mu \tag{3.2}$$

$$[Q, P^\mu] = \{Q, Q\} = \{\bar{Q}, \bar{Q}\} = 0, \tag{3.3}$$

where P^μ is the momentum operator and γ_μ are the Dirac matrices.

The building of supersymmetric lagrangians will not be covered here but is discussed extensively in the literature [15].

- **SUSY solves the *Hierarchy and fine-tuning problems.***
  As previously mentioned there exist quadratic divergences to the Higgs mass which lead to $\Delta M_H^2 \approx O(M_{Planck}^2)$. However, according to the Feynman rules in SUSY, loop corrections contain both fermions and bosons, which contribute by a relative negative sign (as illustrated in figure 3.1) such that:

$$\Delta M_H^2 \approx O(\alpha)|M_B^2 - M_F^2| \approx O(10^{-2})M_{SUSY}^2, \tag{3.4}$$

where M_{SUSY} is a typical SUSY mass scale. The fine tuning problem disappears if the mass scale for SUSY is of the order of 1 TeV[16]. In other words, the *fine-tuning* which was required in order to keep radiative corrections under control is no longer necessary.

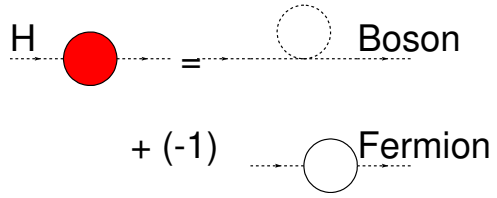

Figure 3.1: *Radiative corrections to the Higgs mass in a supersymmetric model.*

- **Unification of coupling constants.**
  Probably the most favored reason by theorists for the support of a supersymmetric theory is that within a SUSY model, unification of the strong, weak and electromagnetic couplings can be achieved at a common value of 10^{16} GeV[13]. This perfect unification can be obtained as long as the SUSY masses are of the order of 1 TeV. Figure 3.2 illustrates this circumstantial evidence for SUSY. The discontinuity at $\mathcal{O}(100$ GeV) is due to the dissociation of the unified electroweak force into electromagnetism and the weak nuclear force.

- **SUSY naturally incorporates gravity.**
  The SUSY algebra contains P_μ generators which are translations of space-time. Requiring local gauge invariance under such transformations leads to the Einstein theory of gravitation[13]. SUSY naturally is a theory of gravity.

3.1 The Minimal Supersymmetric extension to the Standard Model (MSSM)

The MSSM is defined to be the supersymmetric extension to the Standard Model which contains the minimal number of new particles and interactions that are consistent with the

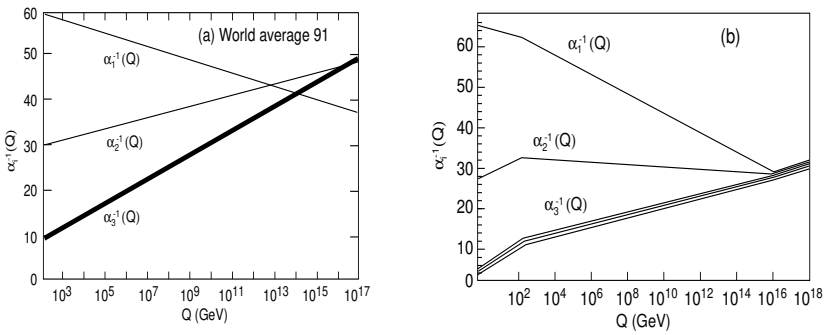

Figure 3.2: *The evolution of the $SU(3)$, $SU(2)$, and $U(1)$ couplings in the (a) the SM and (b) the Minimal Supersymmetric Extension to the SM.*

standard model gauge group. The cost of introducing SUSY is the doubling of the entire SM particle spectrum. See table 3.1.

There is one notable feature in table 3.1 which requires clarification. In the SM, one Higgs doublet is required to give mass to the quarks and leptons. In SUSY, two Higgs doublets are needed in order to give mass to the up-type and down-type quarks.

3.1.1 Neutralino Sector

In the neutral fermion sector, the neutral fermionic partners of the γ and Z^0 gauge bosons, $\tilde{\gamma}$ and $\tilde{Z}$, can mix with the neutral fermionic partners of the Higgs bosons, $\tilde{H}^0_{1,2}$, to form the mass matrix 3.5. Therefore the physical mass states $\tilde{\chi}^0_i$, termed neutralinos, are found by diagonalizing this mass matrix:

$$M_{\tilde{\chi}^0_i} = \begin{pmatrix} M_1 & 0 & -M_Z\cos\beta\sin\theta_W & M_Z\sin\beta\sin\theta_W \\ 0 & M_2 & M_Z\cos\beta\cos\theta_W & -M_Z\sin\beta\cos\theta_W \\ -M_Z\cos\beta\sin\theta_W & M_Z\cos\beta\cos\theta_W & 0 & -\mu \\ M_Z\sin\beta\sin\theta_W & -M_Z\sin\beta\cos\theta_W & -\mu & 0 \end{pmatrix}, \tag{3.5}$$

where θ_W is the electroweak mixing angle. This matrix[17] contains some parameters of the MSSM:

- M_1 and M_2 are the mass parameters of the gauginos associated with the $U(1)_Y$ and $SU(2)_L$ respectively.

Particle		spin	Sparticle		spin
quark	q	1/2	squarks	$\tilde{q}_{L,R}$	0
charged lepton	l	1/2	charged sleptons	$\tilde{l}_{L,R}$	0
neutrino	ν	1/2	sneutrino	$\tilde{\nu}$	0
gluon	g	1	gluino	$\tilde{g}$	1/2
photon	γ	1	photino	$\tilde{\gamma}$	1/2
	Z^0	1	zino	$\tilde{Z}$	1/2
neutral higgs	h, H, A	0	neutral higgsino	$\tilde{H}^0_{1,2}$	1/2
	$W^\pm$	1	wino	$\tilde{W}^\pm$	1/2
charged higgs	$H^\pm$	0	charged higgsino	$\tilde{H}^\pm$	1/2
$\tilde{W}^\pm, \tilde{H}^\pm$ mix to form 2 chargino mass eigenstates $\tilde{\chi}^\pm_1, \tilde{\chi}^\pm_2$					
$\tilde{\gamma}, \tilde{Z}, \tilde{H}^0_{1,2}$ mix to form 4 neutralino mass eigenstates $\tilde{\chi}^0_{1,2,3,4}$					

Table 3.1: *Particle content of MSSM.*

- μ is the Higgs mixing parameter.
- $\tan\beta$ is the ratio of Vacuum Expectation Values (VEV) of the Higgs scalars.

In order to reduce the number of free parameters in the theory a grand unified theory relation is used which relates the gaugino mass parameters M_1 and M_2 [13].

$$M_1 = \frac{5}{3}\tan^2\theta_W M_2. \tag{3.6}$$

In general, the mass eigenstates do not correspond to $\tilde{\gamma}$, $\tilde{Z}$, $\tilde{H}^0_1$ and $\tilde{H}^0_2$ but given values for μ, M_2 and $\tan\beta$, the complicated mixtures of the states is defined. One can get an idea of the behaviour of the neutralino masses as a function of the SUSY parameters in figure 3.3. The masses are defined such that $M_{\tilde{\chi}^0_1} < M_{\tilde{\chi}^0_2} < M_{\tilde{\chi}^0_3} < M_{\tilde{\chi}^0_4}$. A further discussion of the neutralino mass sector can be found in [17].

3.1.2 Chargino Sector

As in the neutralino sector, the physical mass states of the fermionic partners of the $W^\pm$ charged bosons, $\tilde{\chi}^\pm_{1,2}$, called charginos, are defined as linear combinations formed by the diagonalization of the mass matrix:

$$M_{\tilde{\chi}^\pm_i} = \begin{pmatrix} M_2 & \sqrt{2}M_W\sin\beta \\ \sqrt{2}M_W\cos\beta & \mu \end{pmatrix}, \tag{3.7}$$

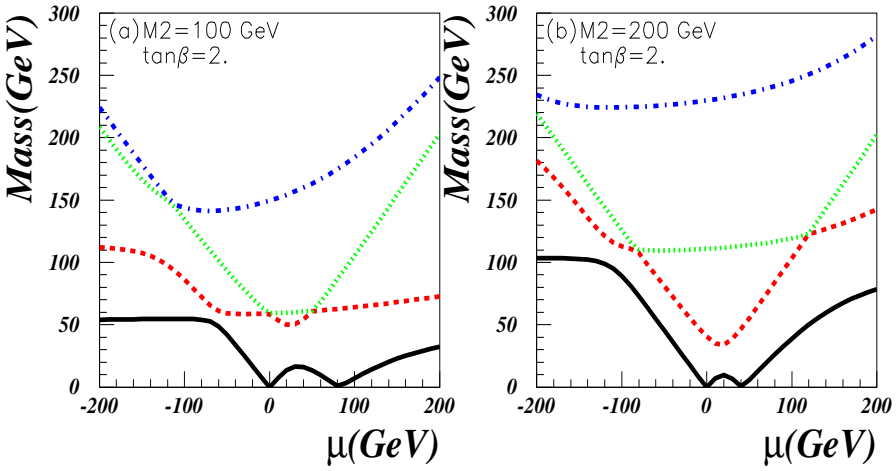

Figure 3.3: *Neutralino masses given at fixed (a) $M_2 = 100\ GeV$ (b) $M_2 = 200\ GeV$ and $\tan\beta = 2$ as a function of μ. $\tilde{\chi}_1^0$ (solid), $\tilde{\chi}_2^0$ (dashed), $\tilde{\chi}_3^0$ (dotted) and $\tilde{\chi}_4^0$ (dash-dot).*

such that

$$M^2_{\tilde{\chi}^\pm_{1,2}} = \frac{1}{2}\left(M_2^2 + \mu^2 + 2M_W^2 \mp \sqrt{(M_2^2-\mu^2)^2 + 4M_W^4\cos^2 2\beta + 4M_W^2(M_2^2+\mu^2+2M_2\mu\sin 2\beta)}\right). \tag{3.8}$$

Figure 3.4 shows the mass of the lightest chargino as a function of μ for representative choices for the value of M_2 and $\tan\beta$. By convention the $\tilde{\chi}_1^\pm$ is the lighter chargino.

3.2 R-Parity

The general SUSY superpotential contains terms which violate baryon and lepton number of the following form:

$$\lambda_{ijk}L_iL_j\bar{E}_k + \lambda'_{ijk}L_iQ_j\bar{D}_k + \lambda''_{ijk}U_i\bar{D}_j\bar{D}_k, \tag{3.9}$$

where ijk are generational indices, L, Q are the left-handed lepton and quark doublet superfields respectively and the $\bar{E}, \bar{D}$ and $\bar{U}$ are the right-handed charged lepton, down-type and up-type quark singlet superfields respectively. The first two terms of equation 3.9 violate lepton number and the thrid violates baryon number. The MSSM framework not only considers minimal particle content but also requires the theory to be minimal in terms of allowed

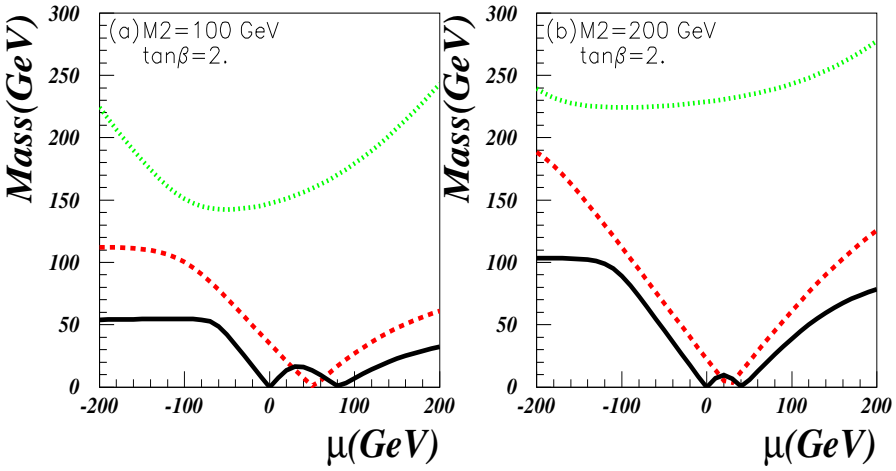

Figure 3.4: *Chargino masses given at fixed (a) $M_2 = 100\ GeV$ (b) $M_2 = 200\ GeV$ and $\tan\beta = 2$ as a function of μ. $\tilde{\chi}_1^\pm$ (dashed) and $\tilde{\chi}_2^\pm$(dotted). The (solid) $\tilde{\chi}_1^0$ mass is plotted as a reference.*

couplings. The extra couplings given in 3.9 can be avoided by imposing a strict conservation of R-parity thereby achieving the goal of minimizing the number of allowed couplings. R-parity is a multiplicative discrete symmetry defined as $R_p = (-1)^{3B+L-2S}$, where B and L are baryon and lepton number respectively and S is spin. It is defined such that $R_p = 1$ for particles and $R_p = -1$ for supersymmetric particles (sparticles). Allowing these R_p violating couplings can lead to rapid proton decay, as illustrated in figure 3.5 for a non-zero λ' and λ'', which is experimentally very constrained[18]. An *ad hoc* way to solve this, is to impose R_p conservation. Another viable[19] and less restrictive symmetry is B-parity which ensures baryon number conservation ($\lambda'' = 0$) and hence proton stability. It should be noted that in the SM this problem of lepton and baryon number violating processes does not arise since such interactions are forbidden by the gauge symmetries of the model.

The consequences of assuming R-parity conservation are two-fold. Since it is a multiplicative quantum number the number of SUSY particles must be conserved modulo 2. In other words, sparticles can only be pair produced from SM particles. Secondly, a sparticle will decay in a cascade until the Lightest Supersymmetric Particle (LSP) is produced, which is necessarily stable. Hence, a model with R-parity conservation will have a LSP which is

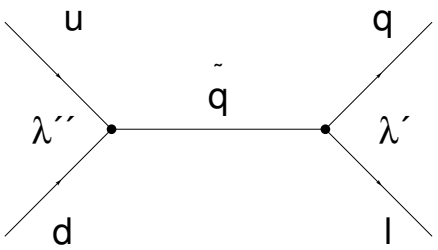

Figure 3.5: *Decay of a Proton via $LQ\bar{D}$ and $U\bar{D}\bar{D}$.*

stable.

The consequences of R-parity violation ($\not{R}_p$) are opposite to the consequences of R-parity conservation. Namely the LSP will not be stable and can decay to ordinary particles. Although the simultaneous presence of lepton and baryon number violating terms (see equation 3.9) is severely constrained by existing limits[20] on the proton lifetime, $\not{R}_p$ searches nonetheless offer a new and rich phenomenology.

3.3 Phenomenology of Supersymmetry at HERA

Models in which R-parity is violated via the $\lambda' L_i Q_j \bar{D}_k$ term hold the most promise for discovery at HERA. This is because the leptonic and hadronic flavours in the initial state at HERA make it an ideal machine for such a search. The cases in equation 3.9 where $\lambda' \neq 0$ are especially promising as they could lead to resonant production of squarks via $e-q$ fusion, with a mass right up to the kinematical limit.

The search for $\not{R}_p$ SUSY is the subject of this thesis. The following sections will outline the phenomenology of the search performed at HERA from the production to the expected final state topologies. A similar search has already been performed by H1[21].

3.3.1 Resonant production of Squarks

One can expand the term $L_i Q_j \bar{D}_k$ in terms of its matter fields [22]:

$$\mathcal{L}_{L_iQ_j\bar{D}_k} = \lambda'_{ijk}[-\tilde{e}^i_L u^j_L \bar{d}^k_R - e^i_L \tilde{u}^j_L \bar{d}^k_R - (\tilde{e}^i_L)^c u^j_L \tilde{d}^{k*}_R + \tilde{\nu}^i_L d^j_L \bar{d}^k_R + \nu_L \tilde{d}^j_L \bar{d}^k_R + (\tilde{\nu}^i_L)^c d^j_L \tilde{d}^{k*}_R] + h.c., \quad (3.10)$$

where the superscripts c denote the charge conjugate spinors and the superscripts $*$ denote the complex conjugate of the scalar fields. The indices L and R, for the scalars, distinguish

the independent superpartner fields of the left and right-handed fermions.

The interactions outlined in equation 3.10 are depicted in figure 3.6 for λ'_{ijk}. Among the 27 possible λ'_{ijk} couplings, only the cases with $i = 1$ are of special interest at HERA because a $e^{\pm}$ in the initial state allows for the s-channel production of squarks through $e^{\pm}$-quark fusion as in graphs (c) and (f) of figure 3.6.

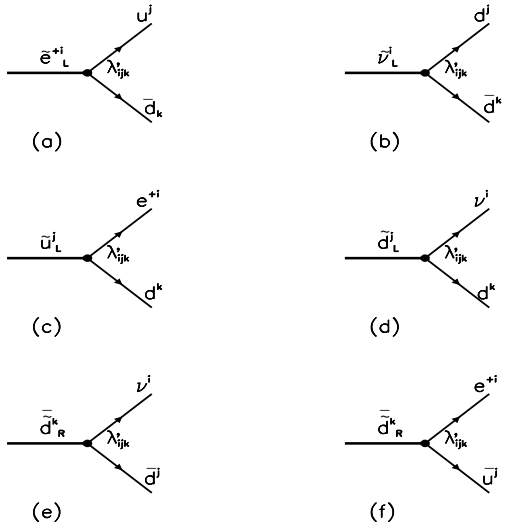

Figure 3.6: *Interaction vertices via λ'_{ijk} couplings.*

Furthermore, HERA is more sensitive to the λ'_{1j1} couplings because they allow for the fusion of the lepton in the initial state with a valence quark from the proton.

Positrons and electrons probe different squark couplings. In the case of e^+ scattering, $e^+d \to \tilde{u}_L$−type squarks dominate the production. As this thesis is based on the data taken from 1994 to 1997, when HERA was operating with a positron beam, the focus of this thesis is a search for $\tilde{u}_L$−type squarks. Table 3.2 lists all pertinent resonant squark production mechanisms at HERA for a positron beam. For e^- scattering, $e^-u \to \tilde{d}_R$−type squarks dominate. A search in e^- scattering at HERA awaits the accumulation of more e^- data.

The cross section for squark production at HERA depends on the square of the strength of the coupling λ'_{ijk}. If this is sufficiently small then the cross section can be approximated by

λ_{1jk}	Production process	
111	$e^+ + \bar{u} \to \bar{\tilde{d}}_R$	$e^+ + d \to \tilde{u}_L$
112	$e^+ + \bar{u} \to \bar{\tilde{s}}_R$	$e^+ + s \to \tilde{u}_L$
113	$e^+ + \bar{u} \to \bar{\tilde{b}}_R$	$e^+ + b \to \tilde{u}_L$
121	$e^+ + \bar{c} \to \bar{\tilde{d}}_R$	$e^+ + d \to \tilde{c}_L$
122	$e^+ + \bar{c} \to \bar{\tilde{s}}_R$	$e^+ + s \to \tilde{c}_L$
123	$e^+ + \bar{c} \to \bar{\tilde{b}}_R$	$e^+ + b \to \tilde{c}_L$
131	$e^+ + \bar{t} \to \bar{\tilde{d}}_R$	$e^+ + d \to \tilde{t}_L$
132	$e^+ + \bar{t} \to \bar{\tilde{s}}_R$	$e^+ + s \to \tilde{t}_L$
133	$e^+ + \bar{t} \to \bar{\tilde{b}}_R$	$e^+ + b \to \tilde{t}_L$

Table 3.2: *Squark production processes at HERA via $\not{R}_p$ λ'_{1jk} couplings with a positron beam.*

the Narrow Width Approximation (NWA) [23] for s-channel production of a scalar resonance:

$$\sigma(e^+p \to \tilde{q}) = \frac{\pi}{4s}\lambda'^2_{1jk}\int q(x)\delta\left(x - \frac{M^2}{s}\right)dx \quad (3.11)$$

$$= \frac{\pi}{4s}\lambda'^2_{1jk}q\left(x = \frac{M^2}{s}\right), \quad (3.12)$$

where $q(x) \approx q(x, m^2_{e^+q})$ is the quark (or anti-quark) momentum density in the proton and s is the centre of mass energy of HERA. It is evaluated at $x = m^2_{e^+q}/s$ and at a virtuality scale of $m^2_{e^+q}$. So for example, $\sigma(e^+d \to \tilde{u}_L)$ depends on the value of λ'_{111} and the d quark momentum density in the proton. For $\bar{\tilde{d}}_R$ squark production simply substitute the $\bar{u}$ quark momentum density in the proton.

For a given coupling strength, the production cross sections for $\tilde{u}_L$ and $\bar{\tilde{d}}_R$ are shown in figure 3.7. The figure illustrates that $\tilde{u}_L$-type squark production dominates for e^+ scattering, as a direct consequence of the relative magnitude of the quark and anti-quark densities inside the proton. Due to the drop in cross section with the squark mass, HERA will be sensitive to low couplings at low masses and higher couplings are high masses.

Two assumptions are made at this point to simplify the search strategy:

- Only one of the $\not{R}_p$ coupling λ'_{1jk} is non-zero. Allowing more than one coupling to exist would complicate the phenomenology. By isolating one coupling at a time and in the absense of any observed signal, a direct limit can be derived on the strength of coupling. Separate analyses[24] have been performed at HERA, which set limits on the product of two couplings but are made in the context of specific topologies, more specific than the search with which this thesis is concerned.

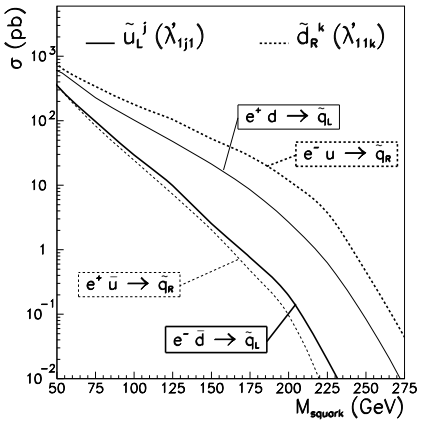

Figure 3.7: *Production cross sections for $\tilde{u}_L$ and $\bar{\tilde{d}}_R$ for $\lambda' = 0.1$ in ep collisions.*

- The gluino, the SUSY partner of the gluon, is much heavier than the squark so that the decays $\tilde{q} \to \tilde{g}q$ are kinematically not possible. The thrust of this analysis is to cover the SUSY parameter space. Hence, since M_3, which is the gaugino mass parameter associated with $SU(3)$ does not enter into the gaugino mass matrices 3.5 and 3.7 this assumption allows us to be insensitive to this parameter. There are additional GUT relations[13] (where $M_3 \approx m_{\tilde{g}}$) which ensure the mass of the gluino is much heavier than the other gauginos thus making this assumption all the more valid.

The number of free parameters in SUSY models is immense and such assumptions are made in an attempt to reduce this number, while covering the broadest possible set of models. The search is in general a topological one, with the primary goal to look for signals which cannot be account for by any SM process. The existence or absense of any signal can then be interpreted in terms of the SUSY models discussed in this chapter.

3.4 Squark Decays

The phenomenology of decay of squarks produced by $\not{R}_p$ is dependent on the strength of the $\not{R}_p$ coupling. If the coupling strength is greater than that of the gauge decays then the squarks will decay via the same $\not{R}_p$ coupling by which they were created. Otherwise they can undergo a gauge decay into a neutralino or chargino, which are the only accessible decays in

MSSM.

3.4.1 $\not{R}_p$ Squark Decays

The width for the $\not{R}_p$ decay of a squark is

$$\Gamma_{\tilde{q}\to qe} = \frac{1}{16\pi}\lambda'^2_{111} M_{\tilde{q}}. \tag{3.13}$$

This width[21] is very small: for a squark mass of 200 GeV and $\lambda'_{111} = 0.1$, it is approximately 40 MeV.

Squark decay, via the $\not{R}_p$ coupling, is shown in figure 3.8. The production and decay of squarks in this fashion is very similar to that of leptoquarks. Data selection and optimization for such topologies is similar to the leptoquark analysis [25]. The final state is characterized

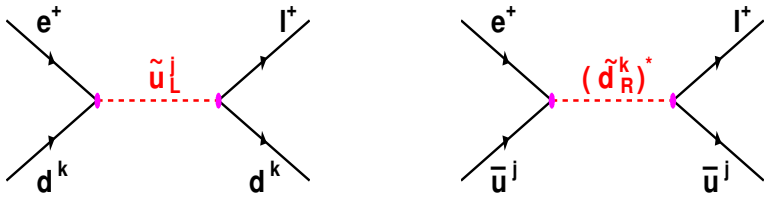

Figure 3.8: *Squark $\not{R}_p$ production and decay diagrams.*

by a positron at high transverse energy (E_T) and a jet. On an event by event basis this final state is indistinguishable from Neutral Current (NC) and Charged Current (CC) deep inelastic scattering (DIS). Nonetheless, in the analysis, one can take advantage of two physical characteristics of scalar squarks:

- The x distribution of a squark produced by and decaying via $\not{R}_p$ coupling should be peaked at $x = \frac{M^2}{s}$. Hence the search strategy focuses on searching for a localized excess above the expected NC and CC x distributions.
- A scalar particle in its rest frame will decay isotropically. Hence the cross section for this decay will be independent of the decay angle θ^* in the centre of mass frame of the particle. θ^* is related to y, which will be explained in chapter 5, in the following manner:

$$\cos\theta^* = 1 - 2y \tag{3.14}$$

Thus one would expect a flat y distribution from a squark decaying via $\not{R}_p$. However, the y distribution for NC DIS, the major background for these processes, drops like $1/y^2$, allowing for a very good signal to background separation.

3.4.2 R-parity conserving or Gauge Squark Decays

Once produced the squarks can undergo decays in which R-parity is conserved. Such decays are the only ones permitted in MSSM models with R-parity conservation and as such they will decay into a particle and a sparticle. These gauge decays, which play an important role when the $\not{R}_p$ coupling is small, depend greatly on the nature of the gauginos.

Choice for the Lightest Supersymmetric Particle

The identity of the LSP is important to the phenomenology of $\not{R}_p$ SUSY. There are favorable cosmological constraints which imply that the LSP is the lightest neutralino [26]. The lightest neutralino, as the LSP, in models which conserve R-parity is a good candidate for *dark matter* since it is necessarily stable. However, such considerations are no longer valid once R-parity is violated. Nevertheless, the LSP is assumed to be the $\tilde{\chi}^0_1$.

There is a small portion of phase space in which $\tilde{\chi}^\pm_1$ is lighter than the lightest neutralino (see figure 3.9). Since the assumption for this analysis is that the $\tilde{\chi}^0_1$ is the LSP, this search is not valid in that small portion of phase space, even though choosing the $\tilde{\chi}^+_1$ as the LSP would not significantly change the final state topologies in this portion of phase space. Figure 3.9 shows which component of the $\tilde{\chi}^0_1$ dominates as a function of the phase space parameters (M_2, μ) at a fixed value of $\tan\beta = 2$.

The decay $\tilde{q} \to q\chi^0_i$

The width for the sfermion gauge decay into a quark and neutralino is given by equation 3.15[27].

$$\Gamma_{\tilde{q}\to q\tilde{\chi}^0_1} = \frac{1}{8\pi}(C^2) M_{\tilde{q}} \left(1 - \frac{M^2_{\tilde{\chi}^0_1}}{M^2_{\tilde{q}}}\right)^2 \tag{3.15}$$

where the factor C depends on the $\tilde{\gamma}$, $\tilde{Z}$ and $\tilde{H}$ components of the $\tilde{\chi}^0_i$. Detailed expressions for C as well as the Feynman rules governing such MSSM reactions can be found in [17]. This decay becomes more significant as the difference in mass between the squark and neutralino increases.

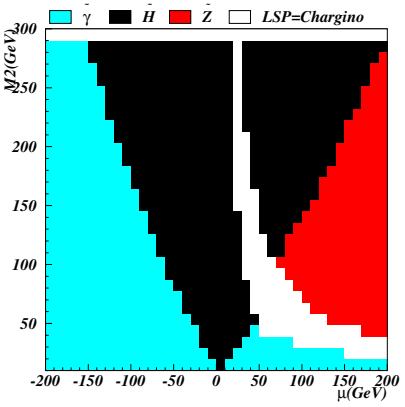

Figure 3.9: *Regions in the SUSY phase space* (M_2, μ) *corresponding to a charged LSP and a neutral LSP dominated by its* $\tilde{\gamma}$, $\tilde{Z}$ *or* $\tilde{H}^0$ *components, for* $\tan\beta = 2$.

The decay$\tilde{q} \to q' \chi_i^+$

Charginos are mixtures of the charged wino ($\tilde{W}^\pm$) and charged higgsino ($\tilde{H}^\pm$) states. It is important to make a distinction at this point between the radically different dynamics of $\tilde{q}q'\tilde{\chi}^\pm$ couplings depending on whether the decaying squark is the SUSY partner of a left or right-handed squark. Take the right-handed squark for example. The weak interaction only couples to left-handed fermions, so the $W^\pm$ does not couple to right-handed fermions. Similarly in SUSY, one cannot couple a wino to a right-handed squark. In the case of a charged higgsino coupling to a right-handed squark, the vertex will be proportional to the mass of the quark (q'). The width of the decay $\tilde{q}_R \to q'\tilde{H}^\pm$ is proportional to $m_{q'}^2$. Should the quark be in the first or second generations this width is negligible. Therefore whether the $\tilde{\chi}^\pm$ is $\tilde{W}^\pm$ or $\tilde{H}^\pm$ dominated, it is unlikely to have a significant probability of occurring.

For a left-handed squark (the dominant production in this analysis) the coupling to a wino is not forbidden. A higgsino dominated $\tilde{\chi}^\pm$ will suffer from suppressions similar to those for $\tilde{q}_R$ decay. The $\tilde{q}_L$ decay width is given by [27]:

$$\Gamma_{\tilde{q}_L \to q'\tilde{\chi}_i^\pm} = \frac{1}{8\pi}(C^2) g^2 M_{\tilde{q}}, \tag{3.16}$$

where the details of C are give in [17]. The $\tilde{q}_L$ decay mode is dominated by its decay into a chargino as soon as it is kinematically possible. This is demonstrated in figure 3.10 where

the dominant gauge decay mode is represented for a 150 GeV $\tilde{u}_L$ squark in the phase space plane (M_2, μ) for $\tan\beta = 2$.

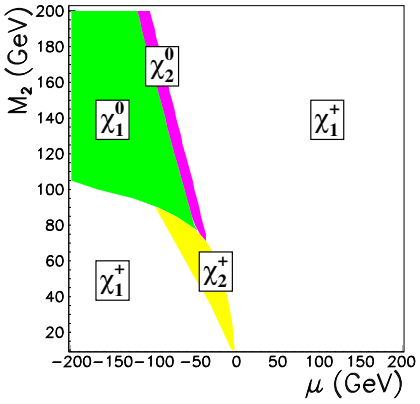

Figure 3.10: *Dominant gauge decay mode for a* 150 GeV $\tilde{u}_L$ *squark in the phase space plane* (M_2, μ) *for* $\tan\beta = 1$[28].

3.5 Neutralino and Chargino Decays

It is necessary to study the decays of the gauginos in order to determine the possible final state topologies when the $\not{R}_p$ produced squark has a gauge decay.

3.5.1 Neutralino Decays

In order to study the decays of the neutralinos it is essential to discuss the dynamics of the LSP. In models of the MSSM in which R-parity is conserved, the LSP is stable. Hence any final state topology for such models consists of a characteristic missing transverse momentum ($\not{P}_T$) coming from the LSP which escapes undetected. On the contrary, in models with $\not{R}_p$, the LSP is in general not stable and may decay into a fermion and a virtual sfermion which subsequently decays through an $\not{R}_p$ coupling. Such decay chains are represented in figure 3.11. When the $\tilde{\chi}_n^0$ decays into a charged lepton it can decay with equal probability to e^+ or e^-. The *wrong* sign lepton ($e^+p \to e^- +$ multijets) is the most unambiguous and background free signature for the production of a squark via $\not{R}_p$.

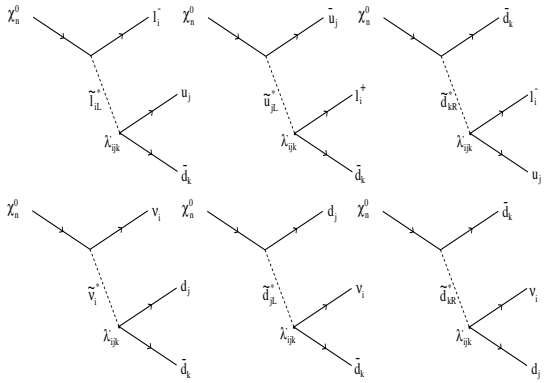

Figure 3.11: *Representative diagrams from the $\not{R}_p$ decay of the $\tilde{\chi}_n^0$ for a non-zero λ'_{ijk}. For $n = 1$ these diagrams represent the decays of the LSP and the final stage of any cascade. The charge conjugate diagrams are not drawn.*

The branching ratios for which $\tilde{\chi}_1^0$ decay is dominant depends on the nature of the $\tilde{\chi}_1^0$, i.e., which component dominates the mixture: the $\tilde{\gamma}$, $\tilde{Z}$ or $\tilde{H}^0$. Recall figure 3.9. The branching ratio for the $\tilde{\chi}_1^0 \to e^{\pm} jets$ is maximum when the $\tilde{\chi}_1^0$ is dominated by its $\tilde{\gamma}$ component and hence the coupling strength is proportional to the charge of the lepton.

If we consider the decay of $\tilde{\chi}_n^0$ where $n > 1$, they can also decay directly via $\not{R}_p$ as shown in figure 3.11. In addition there can be radiative decays such that $\tilde{\chi}_n^0 \to \gamma$ or Z $\tilde{\chi}_1^0$, as illustrated in figure 3.12. The $\tilde{\chi}_{n>1}^0$ are allowed to undergo a gauge decay where R-parity is conserved. The $\tilde{\chi}_1^0$ will decay as described above.

3.5.2 Chargino Decays

Chargino decays become very important once they are kinematically possible as already illustrated in figure 3.10 and are the dominant decay mode in most of the considered phase space. As in the case of $\tilde{\chi}_{n>1}^0$, the $\tilde{\chi}_n^{\pm}$'s can decay via $\not{R}_p$ λ'_{1jk} couplings in a similar fashion to the decays shown in figure 3.11 or undergo gauge decays as in the examples shown in figure 3.13. The $\tilde{\chi}_1^0$ subsequently decays in the assumption of $\not{R}_p$ as described in the previous section resulting in another cascade decay.

There is an enormous number of possible decay modes and an effort was made to consider the most significant modes in order to make the most comprehensive search possible. In that

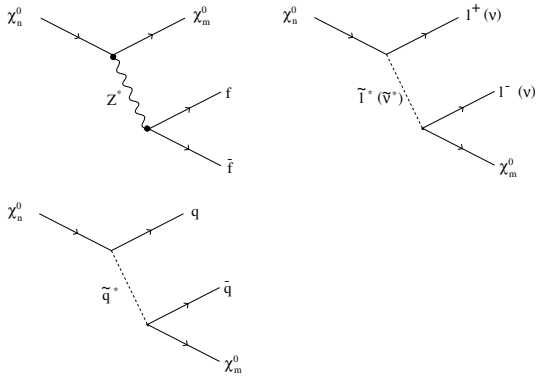

Figure 3.12: *Gauge Decays of the $\tilde{\chi}_n^0$ for $n > 0$, $m < n$.*

respect, cascade decays involving the $\tilde{\chi}_{n>2}^0$ and $\tilde{\chi}_2^+$ were not considered. That is to say that the assumption is made that in this analysis they are not observed. They can occur but the efficiency for their detection is effectively zero. This is reasonable because $\tilde{q} \to q\tilde{\chi}_{n>2}^0$ and $\tilde{q} \to q'\tilde{\chi}_2^+$ channels are rarely or even never a dominant squark decay mode as seen in figure 3.10.

3.6 Possible Final State Topologies

The different decay modes discussed above can be classified into separate topologies depending on their final states. The topologies considered in this search are summarized in table 3.3. Table 3.4 summarizes other distinct topologies which were not included in this search. With positrons in the initial state the $\tilde{u}_L$-type squark production dominates. Hence the final state from $\tilde{\bar{d}}_R \to \nu q$, consisting of one jet and high $\not{P}_T$ is not considered.

Table 3.3 shows all the final states considered in this search which differ in the lepton identity and the number of quarks. Experimentally no distinction is made between two or more reconstructed jets in the final state. Hence, one can see that although there are seven quoted final states, there are only four reconstructed channels. All the final states are considered in terms of efficiency of detection but separate optimizations for the separate multijet topologies are not made. This is discussed further in chapter 7 where the analysis methods are explained. The example decay processes are also representative and not exhaustive.

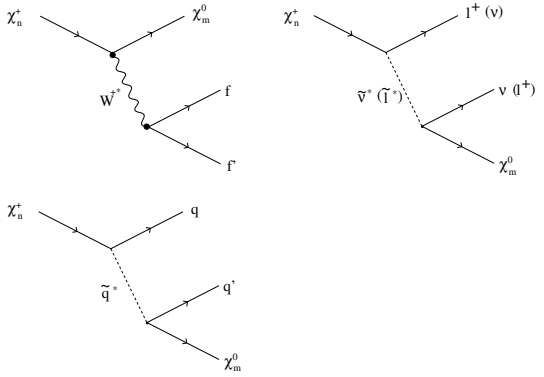

Figure 3.13: *Gauge decay modes for the* $\tilde{\chi}_n^{\pm}$.

3.7 Summary

SUSY is a compelling theory for an extension to the SM, but as yet has no experimental support. The phenomenology of $\not{R}_p$ SUSY at HERA has been outlined and the assumptions made in this particular search were described. The main points are summarized here for convenience.

- The SUSY process under study is the resonant production of a squark through the fusion of a positron incident on a quark from the proton. This mode violates R-parity via an $L_i Q_j \bar{D}_k$ operator.
- In order to study this particular SUSY model the following assumptions were made:
  - The LSP is the lightest neutralino.
  - The gluinos are much heavier than the squarks produced so the decay $\tilde{q} \to \tilde{g} q$ is not kinematically allowed.
  - Only one of the λ'_{1jk} couplings in equation 3.10 is dominant.
  - Although each λ'_{1jk} coupling allows for the production of two unique squarks, $\tilde{q}_L$ and $\tilde{q}_R$, the production is dominated by $\tilde{u}_L$-type squarks when HERA is operating with a positron beam (see figure 3.7).
- The squark may decay via $\not{R}_p$ or gauge decay.

Decay Process		Reconstructed Channel	Final State
$\tilde{q} \xrightarrow{\lambda'} e^+ q'$		High P_T e^+ + 1 jet	$e^+ q$
$\tilde{q} \to q$	$\tilde{\chi}^{0,+}_{1/2,1}$ $\xhookrightarrow{\lambda'} e^+ q' q''$	High P_T e^+ + multijets	$e^+ qqq$
$\tilde{q} \to q$	$\tilde{\chi}^0_{1/2}$ $\xhookrightarrow{\lambda'} e^- q' q''$	High P_T e^- + multijets	$e^- qqq$
$\tilde{q} \to q$	$\tilde{\chi}^+_1 / \tilde{\chi}^0_2$ $\to W^+/Z$ $\tilde{\chi}^0_1$ $\hookrightarrow q' q''$ $\xhookrightarrow{\lambda'} e^+ q' q''$	High P_T e^+ + multijets	$e^+ qqqqq$
$\tilde{q} \to q$	$\tilde{\chi}^+_1 / \tilde{\chi}^0_2$ $\to W^+/Z$ $\tilde{\chi}^0_1$ $\hookrightarrow q' q''$ $\xhookrightarrow{\lambda'} e^- q' q''$	High P_T e^- + multijets	$e^- qqqqq$
$\tilde{q} \to q$	$\tilde{\chi}^{0,+}_{1/2,1}$ $\xhookrightarrow{\lambda'} \nu q' q''$	High $\not{P}_T$ + multijets	νqqq
$\tilde{q} \to q$	$\tilde{\chi}^+_1 / \tilde{\chi}^0_2$ $\to W^+/Z$ $\tilde{\chi}^0_1$ $\hookrightarrow q' q''$ $\xhookrightarrow{\lambda'} \nu q' q''$	High $\not{P}_T$ + multijets	$\nu qqqqq$

Table 3.3: *Squark decay channels in* $\not{R}_p$ *SUSY which were considered, classified by their final states and their reconstructed topologies. This list is only representative and not exhaustive.*

  - After making the assumption in equation 3.6, the neutralino and chargino sectors are defined by three SUSY parameters: M_2, the mass term for the $SU(2)$ gaugino, μ, the Higgs mixing parameter and $\tan\beta$, the ratio of VEVs of the Higgs scalars.
  - The model considered is an unconstrained MSSM with $\not{R}_p$. The sfermion masses are free parameters and are taken to be mass degenerate.
  - By allowing for $\not{R}_p$, the LSP is not stable and can decay as illustrated in figure 3.11.

The final state topologies considered are listed in table 3.3. All cascade decays involving $\tilde{\chi}^0_{1,2}$ and $\tilde{\chi}^+_1$ were taken into account. Four distinct reconstructed channels are searched for:

- e^+ + 1 jet
- e^+ + multiple jets

Nature of LSP $\tilde{\chi}_1^0$	Decay process				Topology
$\tilde{\gamma}$, $\tilde{Z}$, $\tilde{H}^0$	$\bar{\tilde{d}}_R \xrightarrow{\lambda'} \nu q'$				Missing P_T + 1 jet
$\tilde{H}^0$	$\tilde{q} \to q$	$\tilde{\chi}_1^0$			
$\tilde{H}^0$	$\tilde{q}_L \to q'$	$\tilde{\chi}_1^+$			High P_T e^+ or μ^+
		$\hookrightarrow$	W^+	$\tilde{\chi}_1^0$	$+\not{P}_T$+ 1 jet
			$\hookrightarrow l^+\nu$		
$\tilde{\gamma}$,$\tilde{Z}$	$\tilde{q}_L \to q'$	$\tilde{\chi}_1^+$			High P_T $e^\pm$
		$\hookrightarrow$	W^+	$\tilde{\chi}_1^0$	+ High P_T e^+ or μ^+
			$\hookrightarrow l^+\nu$	$\xhookrightarrow{\lambda'} e^\pm \bar{q}' q''$	+ $\not{P}_T$+ multijets
$\tilde{\gamma}$, $\tilde{Z}$	$\tilde{q}_L \to q'$	$\tilde{\chi}_1^+$			High P_T e^+ or μ^+
		$\hookrightarrow$	W^+	$\tilde{\chi}_1^0$	+ $\not{P}_T$+ multijets
			$\hookrightarrow l^+\nu$	$\xhookrightarrow{\lambda'} \nu \bar{q}' q''$	

Table 3.4: *Squark Decay Channels in $\not{R}_p$ SUSY classified by distinct topologies*[27]. *These channels are not considered in the search and as in table 3.3 this list is not exhaustive.*

- e^- + multiple jets
- $\not{P}_T$+ multiple jets

Chapter 4

The Experimental Setup

Particle accelerators and colliders have provided the experimental evidence for the basis of the SM. They will also be the key to providing hints of new physics beyond the SM, or perhaps even stimulate the development of new theories. The Hadron Elektron Ring Anlage (HERA) has already played and continues to contribute an important role in this aspect. In the following section a brief overview of the machine itself and the ZEUS detector is presented. ZEUS is one of the two large detectors at HERA and is a collaboration of about 430 physicists representing 12 countries. A more detailed description of the ZEUS detector can be found in the 1993 Status Report[29].

4.1 HERA: Hadron Elektron Ring Anlage

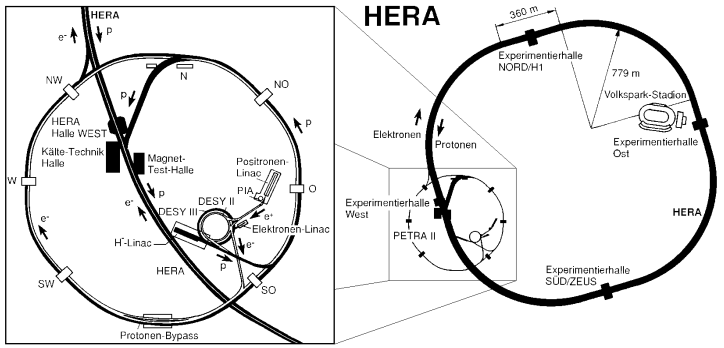

Figure 4.1: *Layout of the HERA accelerator complex and injection system.*

HERA Parameters	Design Values		1997 Values	
	electron	proton	electron	proton
Circumference (m)	6336			
Energy (GeV)	30	820	27.5	820
Magnetic Field (T)	0.165	4.65	0.165	4.65
Luminosity ($cm^{-2}s^{-1}$)	$1.6 \cdot 10^{31}$		$4.3 \cdot 10^{30}$	
Number of colliding bunches	210		174	
Bunch crossing time (ns)	96			
Current (mA)	58	160	30	55
Horizontal beam size				
σ_x (mm)	0.301	0.276	0.239	0.185
Vertical beam size				
σ_y (mm)	0.067	0.087	0.055	0.058
Longitudinal beam size				
σ_z (cm)	0.8	11	0.8	11
Energy loss per turn (GeV)	0.127	$1.4 \cdot 10^{-13}$	0.127	$1.4 \cdot 10^{-13}$
Injection Energy (GeV)	14	40	12	40
Injection time (min)	15	20	45	60

Table 4.1: *HERA design and 1997 running parameters.*

HERA is the world's first and only lepton proton collider and is located at the Deutsches Elektronen-SYnchrotron (DESY) laboratory in Hamburg, Germany. The HERA accelerator complex (figure 4.1) is designed to accelerate electrons to 30 GeV and protons to 820 GeV, yielding a center of mass energy of 314 GeV. The ring has a circumference of 6.3 km and runs 10-30 m below ground level. The design energy of the electron beam is limited by the radio frequency power required to compensate for energy lost due to synchrotron radiation, while the design energy of the proton beam is limited by the 4.65 T maximum magnetic field of the bending dipoles [30]. The counter-circulating electron and proton beams are contained in two evacuated storage rings and collide in the H1 and ZEUS experiments, which are situated in the north (NORD) and south (SÜD) experimental halls, respectively. The parameters used by HERA in 1997 are listed in table 4.1.

Figure 4.2 shows the accumulated luminosity of HERA since 1992. The improving performance can be seen in the increasingly steep slope year by year.

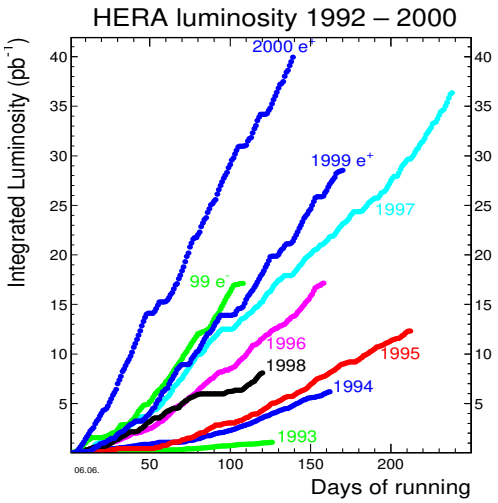

Figure 4.2: *The integrated luminosity recorded by HERA for 1992-2000.*

4.2 The ZEUS Detector

The ZEUS[1] detector at HERA is a general purpose detector and has been in operation since 1992. The detector has a large forward-backward asymmetry to accommodate the boost of the centre-of-mass in the direction of the proton beam, which is caused by the large asymmetry in the energies of the electron/positron and proton beams. The right-handed ZEUS coordinate system is aligned such that the z axis points in the proton beam direction with the origin at the nominal interaction point, and the x axis pointing toward the centre of the HERA ring. The angles θ and ϕ are measured relative to the z and x axes respectively. The ZEUS detector is made up of many components, of which only those of particular relevance to this analysis will be discussed, and is shown in figure 4.3.

[1] *ZEYΣ: Ζήτησις καθ' Ευρετής Υποκειμένης Συμμετρίας, Search to Elucidate Underlying Symmetry*

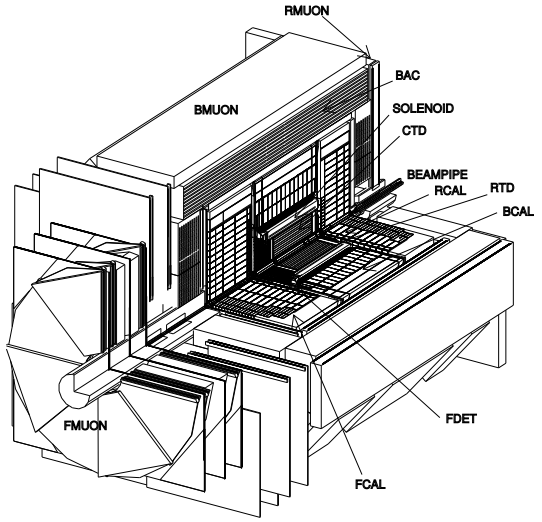

Figure 4.3: *Cutaway view of the ZEUS detector.*

4.2.1 The Central Tracking Detector

The central tracking detector (CTD) provides a measurement of the direction and momentum of charged particles with high precision [31, 32, 33]. It is a cylindrical drift chamber made up of 72 concentric layers divided into nine superlayers. The active volume of the CTD has a length of 205 cm, an inner radius of 18.2 cm and an outer radius of 79.4 cm. The CTD operates in a 1.43 T solenoidal magnetic field. Tracks are reconstructed in the angular range $15° < \theta < 164°$ and there is full coverage in azimuthal angle ϕ.

A gas mixture of Ar/CO_2/ethane and ethanol is used to fill the tracking volume. Argon, which is relatively inexpensive requires only a low intensity electric field for avalanche formation, forms the main component of the tracking chamber gas. Gases consisting of heavy organic molecules, such as carbon-dioxide and ethane, are known as 'quenchers' [34]. Such 'quencher' gases have many degrees of freedom and can efficiently absorb energy from the avalanche in order to stop it. The carbon-dioxide also lessens the flammability of the mixture [35]. The quenching process discussed above may occasionally lead to polymerization in which liquid or solid polymers deposit on the chamber wires, which seriously affects the operation of the drift chamber. A non-polymerizing agent like ethanol is added to reduce this effect. Charged particles traveling through the CTD ionize gas atoms. The emancipated

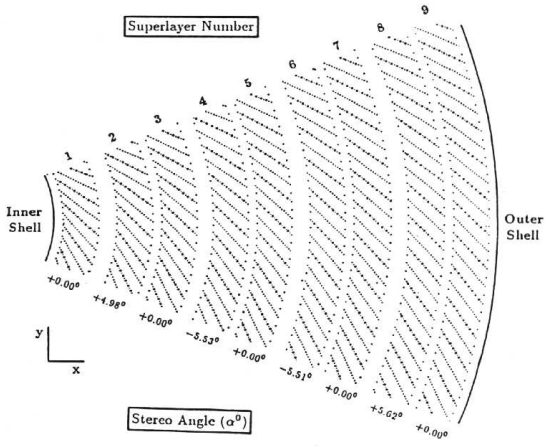

Figure 4.4: *One octant of the CTD showing the field and sense wires. The stereo angle for the stereo layers is also displayed.*

electrons then travel azimuthally to the anode sense wires where they avalanche and cause a measurable electric pulse.

The sense and field wires are divided into octants, one of which is shown in figure 4.4. The heavier dots indicate sense wires while the lighter dots represent field wires. Field wires are held at varying potentials to create a uniform electric field. In every other superlayer the wires are strung parallel to the beam axis, while the wires in the other superlayers are angled approximately five degrees from the beam axis in order to measure the z position of a track via a stereo effect. In total, the CTD consists of 4608 sense wires and 24192 field wires. Superlayers 1, 3 and 5 are instrumented with a z-by-timing system for trigger purposes and have z resolution of approximately 4 cm. The resolution of the CTD in $r-\phi$ is about 230 μm, resulting in a typical event-by-event interaction vertex resolution of 0.4 cm in z and 0.1 cm in the transverse plane. Although the z-by-timing system has a poorer resolution, it provides a fast signal to be used by the trigger system to reject beam related background. The transverse momentum (p_t) resolution for full-length tracks can be parameterized as $\sigma(p_t)/p_t = 0.0058p_t \oplus 0.0065 \oplus 0.0014/p_t$ [36], with p_t in GeV.

4.2.2 The Uranium Calorimeter

Calorimeters are devices which measure the total energy deposited by a particle or group of particles. The absorbed energy in the calorimeter is converted into a measurable signal

which is proportional to the energy of the incident particle. One class of calorimeters are sampling calorimeters which are composed of layers of active material interleaved with layers of an absorber. The incident particles interact with the materials in the absorber layers, producing secondary particles which in turn interact and lead to the development of a particle shower. The active layers 'sample' or measure the energy flow as a function of depth. The characteristic length of electromagnetic showers is smaller than that of hadronic showers of comparable energy. As a result, electromagnetic calorimeters are found in front of their hadronic counterparts.

Electromagnetic showers consist of electrons, positrons and photons. At energies above 1 GeV the following processes dominate an electromagnetic shower:

- Bremsstrahlung: The radiation of photons, from electrons and positrons, under the influence of the field surrounding heavy nuclei. The energy loss is proportional to $\sim Z^2$, where Z is the atomic number of the material traversed.

- Pair production: Photons with enough energy can produce an electron and positron pair under the influence of the field of nuclei. The cross section is proportional to Z^2.

At lower energies:

- Ionization: Electrons and positrons lose energy by ionizing the traversed medium. The energy loss is proportional to $Z \log Z$.

- Photo-electric effect: When the photon is absorbed by an atomic electron, the atom can be ionized. The cross section for this process is proportional to $Z^4 - Z^5$, dominating at lower photon energies.

The scale for electromagnetic showers can be expressed in terms of the radiation length, X_0, and is material dependent. X_0 is defined as the energy loss of electrons through bremsstrahlung at energies above 1 GeV:

$$\left(\frac{\mathrm{d}E}{\mathrm{d}x}\right)_{brems} = -\frac{E}{X_0}, \tag{4.1}$$

where x is the thickness of the material and E is the energy of the incident electron.

Incoming hadrons not only undergo electromagnetic, but also nuclear interactions. The hadronic shower is more complicated due to the enormous variety of processes. The secondaries, in hadronic showers, are mainly created in inelastic collisions with nuclei in the absorber material. The following processes contribute to the development of hadronic showers:

- production of charged hadrons that lose energy by ionization until a new strong interaction occurs.
- production of neutral hadrons that only undergo strong interactions.
- production of neutrinos which escape the calorimeter undetected.
- production of particles which shower electromagnetically.
- production of excited nucleons, which release low energy photons or nucleons or which undergo fission.

The hadronic shower starts to die out, when the energies of the shower particles become so small, that they are completely absorbed. The scale for hadronic showers can be expressed in terms of the nuclear interaction length, λ_{int}, or the mean free path between hadronic interactions. It is defined by:

$$\lambda_{int} = \frac{A}{\rho N_A \sigma_i}, \tag{4.2}$$

where A is the mass number of the absorber, ρ is the specific density, N_A is Avogadro's number and σ_i is the inelastic cross section [37].

The ZEUS calorimeter [38, 39, 40] is a sampling calorimeter which consists of alternating layers of 3.3 mm thick plates of steel-clad depleted uranium as the absorber and 2.6 mm thick plates of plastic scintillator as the active material. The ratio of the thickness of the uranium to the scintillator is chosen to achieve compensation, i.e. the response to hadronic and electromagnetic particles is equal ($e/h = 1.00 \pm 0.03$), and to give a good energy resolution for hadrons and jets. The energy resolution of the calorimeter is $\sigma(E)/E = 0.35/\sqrt{E(\mathrm{GeV})}$ for hadrons and $\sigma(E)/E = 0.18/\sqrt{E(\mathrm{GeV})}$ for electrons/positrons, as measured in a test beam. The calorimeter also provides an accurate timing measurement with a resolution of $\sigma(t) = 1.5/\sqrt{E(\mathrm{GeV})} \oplus 0.5$ ns in a single cell with energy above 3 GeV.

The calorimeter is divided into parts, with each part being longitudinally segmented into an electromagnetic (EMC) section and one or two hadronic (HAC) sections (figure 4.5). The forward calorimeter (FCAL) covers $2.2^\circ < \theta < 39.9^\circ$ and contains two hadronic sections. The barrel calorimeter (BCAL) covers $36.7^\circ < \theta < 129.1^\circ$ and also has two HAC sections. The rear calorimeter (RCAL) covers $128.1^\circ < \theta < 176.9^\circ$ and has only one HAC section, since hadrons individually have low energy in the RCAL due to the forward boost. The EMC sections are 25 radiation lengths thick and contain most of the energy of an electromagnetic shower. The total depth of the calorimeter ranges from 7 nuclear interaction lengths in FCAL to 4 interaction lengths in RCAL. The calorimeter is hermetic except for a 20×20 cm hole in FCAL and a 20×8 cm hole in RCAL to accommodate the HERA beam-pipe.

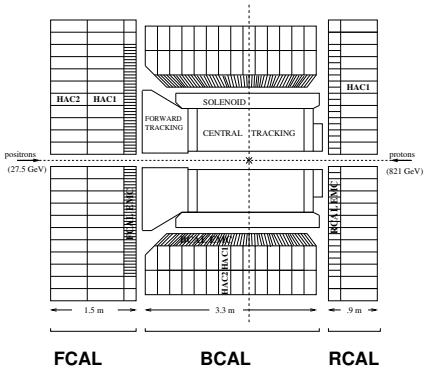

Figure 4.5: *The ZEUS calorimeter (y-z projection).*

The scintillator light, from each calorimeter cell, is read out by two wavelength shifter (WLS) light guides on opposite sides of the cell attached to photomultiplier tubes (PMT), providing redundant left/right readout. There are $\sim$ 10000 PMTs in the calorimeter.

The natural radioactivity of the depleted uranium provides a stable reference signal which is used for calibration of the calorimeter. Using this signal, the energy calibration of the calorimeter is precise to 1%.

4.2.3 Other Components

Other subdetectors of the ZEUS detector illustrated in figure 4.3 are briefly described here for completeness but were not central to the analysis which is described in this thesis. An instrumented-iron backing calorimeter[41] (BAC) measures energy leakage from the CAL. The muon chambers in the forward[29] (FMUON), rear (RMUON) and barrel[42] (BMUON) regions are used to measure muons in ep physics events and to identify and remove background events induced by cosmic-ray or beam-halo muons. The rear (RTD) and forward (FDT) tracking detectors are planar drift chambers which provide supplement tracking information which can be combined with the CTD to reconstruct particle tracks in the regions outside of the full-length track CTD acceptance. The FDET is a composed of three planar drift chambers, interleaved with two transition radiation detectors (TRD).

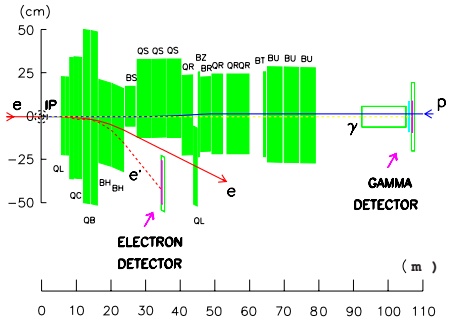

Figure 4.6: *The Layout of the ZEUS luminosity monitor as well as some of the HERA quadrapole (Q) and dipole (B) magnets.*

4.2.4 The Luminosity Monitor

In order to measure a cross section, the delivered luminosity must be determined. The luminosity for ZEUS is determined by measuring the rate of hard bremsstrahlung photons from the Bethe-Heitler process $ep \to ep\gamma$ [43], an electromagnetic process whose cross section is precisely known to an accuracy of 0.5%. Thus, a precise measurement of the photon rate allows for precise determination of the ep luminosity at HERA.

Photons from the Bethe-Heitler process with $\theta_\gamma < 0.5$ mrad exit the beam-pipe downstream of a large vertical bend in the proton beam line. The photons are then detected at $z = -107$ m by a lead/scintillator sampling calorimeter (LUMIG)[44] as shown in figure 4.6. A carbon/lead filtered is installed in front of the LUMIG detector to shield the detector from synchrotron radiation. The LUMIG detector has a resolution of $\sigma(E) = 0.23/\sqrt{E(\mathrm{GeV})}$. The luminosity is determined from the cross section, the counting rate of photons and the photon acceptance.

A small electromagnetic lead/scintillator calorimeter (LUMIE) at $z = -35$ m detects electrons between 7 and 20 GeV produced at $\theta_e < 5$ mrad with respect to the electron/positron beam direction. These electrons are deflected more by the HERA magnet system than electrons/positrons at the beam energy and leave the beam-pipe at $z = -27$ m and impact the LUMIE detector. The LUMIE detector has a resolution of $\sigma(E) = 0.18/\sqrt{E(\mathrm{GeV})}$. Coincidences of both the electron/positron and photon from the Bethe-Heitler process in the LUMIE and LUMIG detectors allow the LUMIG to be calibrated.

4.3 Trigger and Data Acquisition System

4.3.1 The First and Second Level Trigger

The HERA beam bunches cross once every 96 ns giving a beam crossing rate of 10.4 MHz. In contrast, interesting physics events occur at a rate of $\mathcal{O}(100)$ Hz and the output of recorded events is limited to a rate of $\mathcal{O}(10)$ Hz. The high background rates predominately consist of beam-gas events, which are largely caused by the proton beam interacting with the residual gas in the beam pipe and the walls of the beam pipe upstream of ZEUS. A sophisticated trigger decision is necessary to filter the interesting ep events out of the large background rate. Such a trigger decision cannot be made within the 96 ns between bunch crossings. Therefore, in order to minimize dead time, the ZEUS trigger uses a three level, pipelined trigger system as shown in figure 4.7. Even though it requires 0.3 s for all three levels of the trigger to analyze an event, the trigger is able to analyze every beam crossing due to the pipelining. Additionally, since each event contains roughly 100 KByte of information, only a small rate of events can be written to disk/tape and the trigger selects a manageable rate of less than 10 Hz from the 10.4 MHz beam crossing rate.

Each ZEUS subcomponent has its own first level trigger (FLT) electronics, the main FLT subcomponents being the calorimeter and CTD. These electronics have available to them very coarsely measured quantities which they analyze using pipelined logic and after approximately 25 bunch crossings they report their results to the global first level trigger (GFLT). The GFLT issues a global trigger decision based on various logical combinations of the information from the subcomponent FLTs. This final decision occurs 4.4 μs bunch crossings after the original event occurred. There is a small dead time from stopping the pipelines at the first level to read out the front end data from the components after the a first level trigger.

Data from events accepted by the GFLT are handed to each subcomponent's second level trigger (SLT) which analyzes the data using its own transputers and electronics. At the second level, the data are mostly digitized and are more precise than at the FLT. The global second level trigger (GSLT) uses transputers to process the information from the subcomponent SLTs and is able to use more complex algorithms which require more processing time than the GFLT when deciding to accept or reject an event.

4.3.2 The Third Level Trigger

Events accepted by the GSLT are handed to the event builder (EVB) which combines and formats the data before sending it to the third level trigger (TLT). The TLT is the first

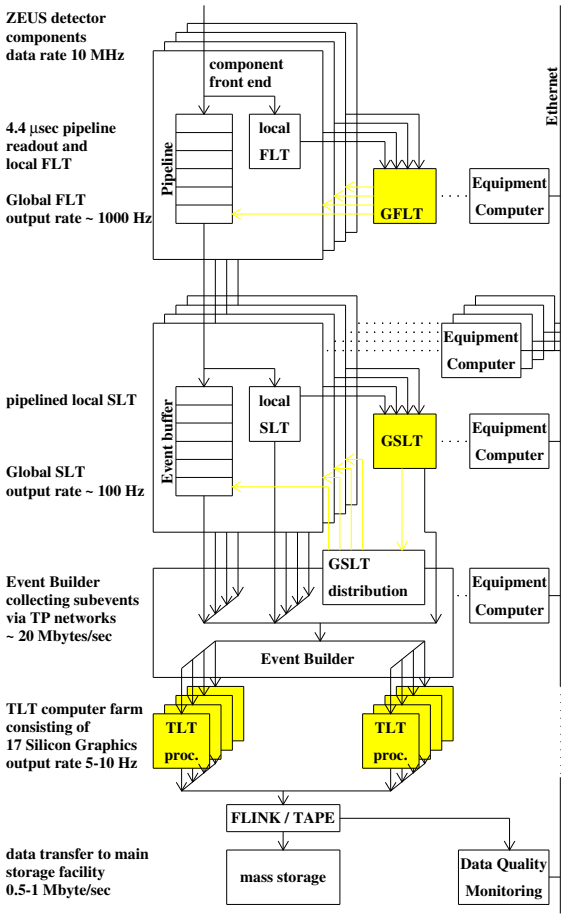

Figure 4.7: *Schematic diagram of the ZEUS trigger and data acquisition system.*

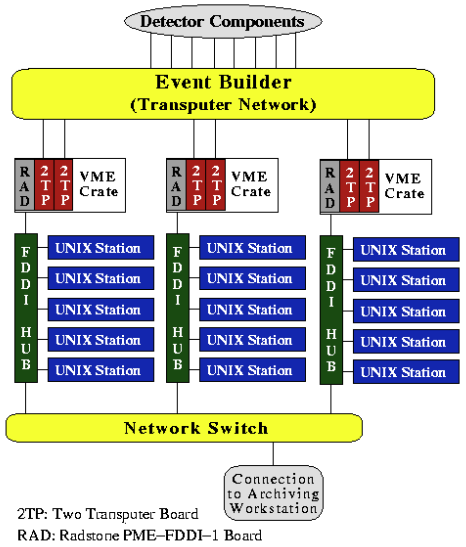

Figure 4.8: *The TLT hardware design.*

trigger level which has access to the complete data flow from all components of the detector and is able to use sophisticated algorithms to pick out specific physics channels from the data. The TLT is the first trigger level to have access to the complete raw event data and hence the global quantity of an event can be exploited. In principle any offline selection can be performed online, limited only by the CPU power. The TLT is designed to reduce an EVB rate of $\sim$ 100 Hz to $5 - 10$ Hz, and this is accomplished by running an optimized version of the reconstruction software. In particular, a track reconstruction package is run on the information from the CTD [45]. As of the start of 1997, the full tracking reconstruction code, the same one used offline in reprocessing, was used online at the TLT.

The Hardware Design

The TLT hardware design is depicted in figure 4.8. On a positive decision of the SLT, the EVB gathers all the component data and writes the whole event into VME memory. Two memories are read out over VMEbus by one PME-FDDI-1 board (manufactured by Radstone Technology PLC) on which WindRiver's operating system VxWorks is running. On request, the PME-FDDI-1 board sends events via fiber optic loop to a target UNIX workstation. The farm of workstations is composed of 14 Silicon Graphics Challenge S UNIX stations,

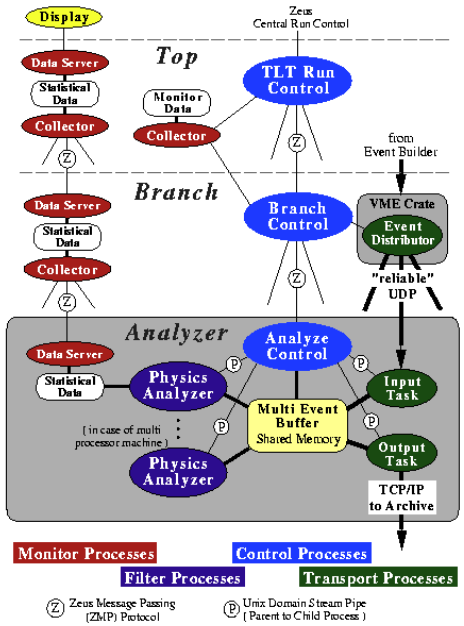

Figure 4.9: *The TLT software design.*

each containing an R4400 MIPS Technologies processor, and 3 Silicon Graphics Origin 200 UNIX workstations, each containing duel R10000 MIPS processors. The workstations are all connected via an FDDI loop and connected to a network switch, hence only outgoing packages to the archiving workstation cross the switch.

The Software Design

The TLT processes are divided into control, transport and monitor layers which operate independently from one another, apart from the interprocess communication. All processes in the system are event driven. Furthermore, the processes are ordered in a hierarchy as shown in figure 4.9. The TLT Run Control is the top level which interfaces with the ZEUS Central Run Control (CRC) and handles all state transitions of the TLT. The states are, *IDLE, READY* and *ACTIVE*. The next level in the hierarchy are the Branch Controllers which in turn are in charge of the Analyzers.

All processes of the control process layer deal with the state transitions. All control processes wait for messages from the appropriate processes in the hierarchy and are able to

synchronize through an exchange of state information. In this way, a restarted process can join the system in any state or state transition. The Analyze-Controller is the parent process of the Input and Output tasks and of the Physics Analyzer. There is one Analyze-Controller and Physics Analyzer per processor.

The transport layer handles the data from from the EVB to the workstations. The Event-Distributer, running on the PME-FDDI-1 board, sends events on request to the Input processes. The events are written to a multi-event-buffer on the assigned workstation from where, upon a positive decision of the physics filters, they are sent to the archiver.

The only process in the filter layer is the Physics Analyzer. While being analyzed, an event remains in the multi-event-buffer, and the results of the physics decision are appended only if the event is accepted. For monitoring purposes, the filter job keeps track of various statistical data during a run. The information is written to shared memory, where it can be accessed by the monitoring layer processes. The monitor processes have no impact on any of the other processes in the system but offer the only method of monitoring the performance and quality of the data.

The TLT Trigger Decision

The TLT trigger decision is made in three stages, shown in the flow chart in figure 4.10. By the time the data has reached the TLT, most of the non-ep backgrounds have been rejected. Nonetheless, a final strict rejection criteria against this non-ep background is performed in the first 2 stages of the TLT decision. At the TLT there are 4 classes of vetoes applied, which rely on the calorimeter and track reconstruction and muon identification. The vetoes were designed to reject "sparks", beam-gas and cosmic and halo muon events, and must provide fast rejection of background while maintaining a high efficiency for physics events.

A spark occurs when a calorimeter PMT housing at high voltage discharges to ground. The rate is low but significant for $\sim$ 10000 PMTs. In general, a spark occurs in only one PMT in a given cell and may be identified by a large left-right asymmetry in the cell energy. An event is classified as a spark if it satisfies:

$$E_L + E_R > 1.5 \text{ GeV} \quad \text{AND} \quad \left|\frac{E_L - E_R}{E_L + E_R}\right| > 0.9 \tag{4.3}$$

Events are rejected if they contain a single spark and less than 2 GeV elsewhere in the calorimeter.

In order to remove residual beam-gas events, the calorimeter timing information is used [46]. As illustrated in figure 4.11, particles coming from ep interactions at the interaction point (IP) arrive almost simultaneously at the calorimeter at $t = 0$.

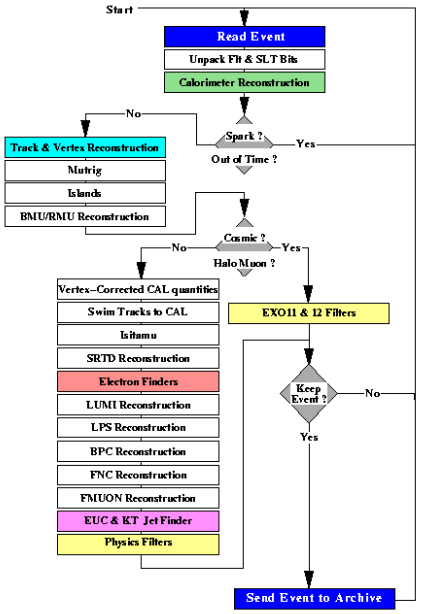

Figure 4.10: *Flow chart outlining the TLT trigger decision.*

The rejection algorithm calculates a weighted average time for the FCAL, RCAL and global regions (the entire CAL) using PMTs with at least 200 MeV. The TLT reads in a list of known bad channels from the calorimeter. Only those cells with two good PMTs with an asymmetry $\left|\frac{E_L-E_R}{E_L+E_R}\right| < 0.2$ are included in the time measurement. The error on the time of each PMT, σ_i, is parameterized as a function of the PMT energy, E_i:

$$\sigma_i(\text{ns}) = 0.4 + \left(\frac{1.4}{E_i(\text{GeV})}\right)^{0.65}. \tag{4.4}$$

The time average for any region can is given by:

$$t_{F/RCAL,global} = \frac{\sum_i (t_i/\sigma_i^2)}{\sum_i (1/\sigma_i^2)}, \tag{4.5}$$

with error

$$\sigma_{t_{F/RCAL,global}} = \left(\sum_i (1/\sigma_i^2)\right)^{-1/2}. \tag{4.6}$$

The energy thresholds for the calulations given in equations 4.4, 4.5, and 4.6 to be made, are 1 GeV in RCAL and the global calculations and 2 GeV for FCAL. An event is vetoed if

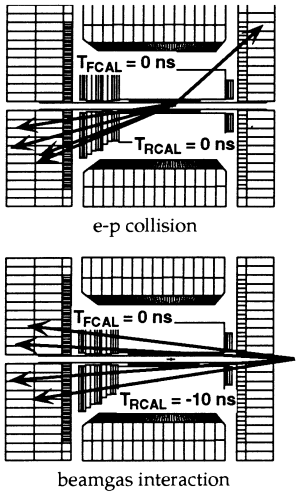

Figure 4.11: *Time measurements for ep and beam-gas interactions.*

there is sufficient energy in a region and if one of the following conditions are satisfied:

$$|t_{FCAL}| > \max(8 \text{ ns}, 3\sigma_{t_{FCAL}}) \tag{4.7}$$

$$|t_{RCAL}| > \max(8 \text{ ns}, 3\sigma_{t_{RCAL}}) \tag{4.8}$$

$$|t_{global}| > \max(8 \text{ ns}, 3\sigma_{t_{global}}) \tag{4.9}$$

$$|t_{FCAL} - t_{RCAL}| > \max(8 \text{ ns}, 3\sqrt{\sigma_{t_{FCAL}}^2 + \sigma_{t_{RCAL}}^2}) \tag{4.10}$$

Figure 4.12 shows how efficient the timing cuts are in separating the major beamgas background from the *ep* candidates.

If an event survives the spark and beam-gas vetoes, a muon rejection algorithm `MUTRIG`[47] is applied at the TLT, in order to reject cosmic muons or proton beam related halo muons which can traverse the detector. Examples of such events are given in figure 4.13. The rate of cosmic and halo muons is substantially lower than the beam-gas background but nevertheless can be of $\mathcal{O}(10)$ Hz. To be sure that no interesting events of possible new physics are being lost, vetoed events flagged as cosmic or halo muons are passed through two exotic physics triggers. EXO11 and EXO12 make use of the `GLOMU`[48] package, a more sophisticated muon identification routine to recover those events considered to be cosmic or halo muons with only a marginal probability.

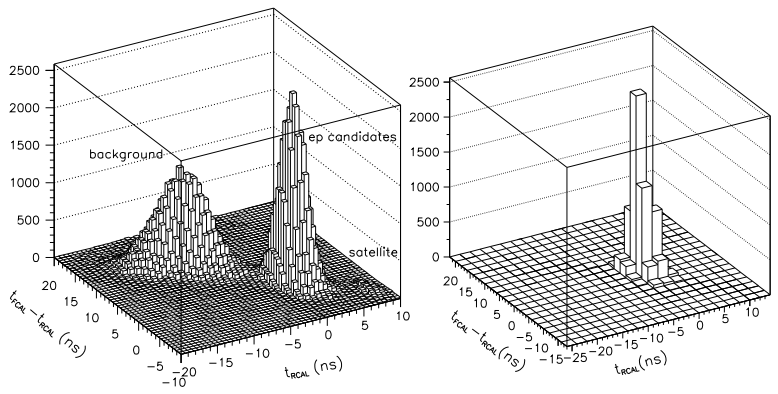

(a) (b)

Figure 4.12: *Time distributions of RCAL times versus the FCAL minus RCAL time (a) before and (b) after the TLT trigger decision.*

Finally, events are processed through the filters and are kept only if one of the physics triggers fires. A provision is made, at all levels of the data acquisition (DAQ) chain, to accept a certain rate of events which are simply passed through the trigger regardless of its decision. These are useful for rate studies for new triggers, upgrading existing ones, helping to determine trigger efficiencies and evaluating the data quality.

The Physics Filters

The current physics software is composed of over 50000 lines of predominantly `fortran` and some `C` code. There are 125 filter slots classified into five major groups relating the class of physics events selected. The groups are soft photoproduction (SPP), hard photoproduction (HPP), deep inelastic scattering (DIS), heavy flavour (HFL), exotic and rare phenomena (EXO) and muons (MUO). There are also an additional two slots, VTX01 which selects a control sample of events with a reconstructed vertex within $|z_{vtx}| < 75$ cm, and SAP01 which selects events tagged by the leading proton spectrometer.

The physics filters make use of all the reconstructed data which takes place at the TLT prior to the events being passed through the physics triggers. In particular, NC DIS events rely on the $e^{\pm}$ identification. Four separate algorithms are used at the TLT. The `LOCAL` algorithm searches for clusters of energy deposits in the calorimeter and cuts on the ratio of EMC/HAC energy [49]. `ELECT5`[50] sums the energy in a 11.5° cone around EMC cells. The

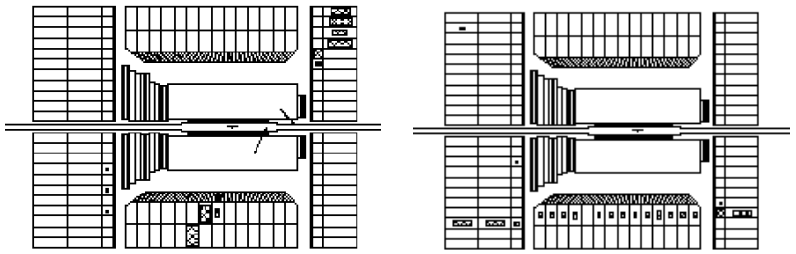

(a) Cosmic (b) Beam Halo

Figure 4.13: *Examples of cosmic and halo muons in the ZEUS detector.*

other two algorithms run online are more sophisticated. `SINISTRA`[51, 52] is a neutral net based finder and `EMILLE`[53] uses probability distributions of detector response for $e^{\pm}$ and is a variant of the $e^{\pm}$-finder used in this thesis (see section 5.4).

Jet-finding algorithms (see section 5.5) are also used online. Two jet-finders, `EUCELL`[54] and K_T, are employed online. The latter is the one used in this analysis.

The filter slots are the responsibility of the physics groups at ZEUS. The entire TLT filter code can be simulated offline using `tltzgana`. This code is available to all physics groups and is used to verify online trigger decisions and develop or upgrade filter slots. Unlike the FLT, a trigger slot is a software fabrication and the number of slots is not restricted and simply depends on the processing power required to meet the demands of the experiment.

Performance of the TLT

The TLT has been a crucial part of the ZEUS DAQ chain since the inaugural run in 1992. In 1995 the TLT hardware was redesigned and the old Fermilab Branch Bus system[55] was replaced with more modern and commercial technology. The writing of events from the PME-FDDI-1 board to the workstations operates at a sustained rate of 5.5 MByte/sec [56]. The hardware itself is able to write at a rate of 7 MByte/sec from its internal DRAM to the FDDI loop, but is limited by the data transfer speed over the VMEbus. Event transfers from the workstations to the archiver were measured[56] to be 11.5 MByte/sec. With the EVB writing out at rates of up to 30 Hz per VME memory at an average event size of 100 kBytes, one PME-FDDI-1 board keeps up reading out two memories, yielding a 60 Hz event rate per TLT branch.

Over the years more demand has been placed on the TLT to make more extensive event reconstruction in order to provide more refined and sophisticated trigger decisions. CPU

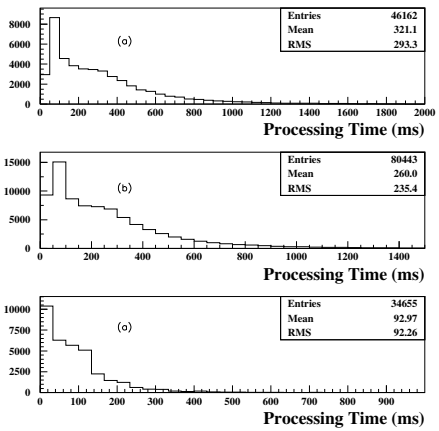

Figure 4.14: *The CPU processing time required by the TLT. (a) For R4400/150 MHz processors of which there are 7, (b) for R4400/250 MHz processors of which there are 7 and (c) for R10000 processors of which there are 5 used online.*

power has been added to meet this demand while maintaining the design requirement to handle 100 Hz input event rate. In the current configuration the input limit of the TLT has been estimated to be 103 Hz[57]. Typical CPU times are shown in figure 4.14. The distribution of total processing times in 1997 indicate a mean processing time of 237 ms, which is dominated by the vertex and track reconstruction processing time.

The system is extremely resilient, allowing processes to restart automatically during data taking. A process may crash for several reasons. For example, a hardware failure which could be repaired mid-run, a power glitch, memory resources maximized by system processes causing a reboot or network interruption causing multiple timeouts. The physics analyzer process may also crash due to a rare bug in the filter code. In this situation, the event which was being processed during the crash is dumped to disk, allowing the TLT expert to retrace the cause and remedy any programming anomaly. The communication processes are all based on standard network protocols which ensures good portability and maintainability. Any demand for more bandwidth or CPU power can easily be satisfied by adding more TLT branches and/or more workstations to the system. The separation of the filter layer and other TLT processes allows for easy modifications of the physics algorithms.

Chapter 5

HERA Kinematics and Event Reconstruction

5.1 Physics at HERA

5.1.1 Deep Inelastic Scattering (DIS)

Lepton-Hadron scattering has been a rich source of information in the past for understanding the structure of nuclei and nucleons. HERA continues this tradition by probing the structure of the proton at smaller distance scales than ever before. The process of a positron-proton interaction is shown in figure 5.1 to lowest order in perturbation theory.

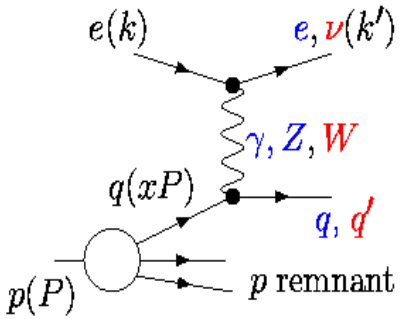

Figure 5.1: *A schematic view of the Deep Inelastic Scattering Process at HERA.*

Given the 4-vectors of the initial and final states, $k = (E_e, \vec{k})$, $p = (E_p, \vec{p})$ and $k' = (E', \vec{k'})$, $p' = (E_X, \vec{p'})$ respectively, one can derive four Lorentz invariant quantities which characterize DIS. The interaction is characterized by the constant centre of mass energy, $\sqrt{s}$, which is a function of the energies of the colliding beams:

$$s = (k + p)^2 \approx 4E_e E_p \tag{5.1}$$

Note that at HERA beam energies the beam particle masses can be neglected in the derivation of s. The other invariants are:

$$Q^2 = -q^2 = -(k - k')^2, \quad 0 \leq Q^2 \leq s \tag{5.2}$$

$$x = \frac{Q^2}{2p \cdot q}, \quad 0 \leq x \leq 1 \tag{5.3}$$

$$y = \frac{p \cdot q}{p \cdot k}, \quad 0 \leq y \leq 1 \tag{5.4}$$

Q^2 is the negative of the 4-momentum transfer squared between the initial and final state leptons and sets the scale of the interaction. At high Q^2 the positron-proton interaction is essentially a positron-quark interaction. The invariant x is the fraction of the proton's momentum carried by the struck quark. Finally, y, sometimes referred to as the *inelasticity*, can be interpreted as the fractional energy transfered from the positron to the proton vertex, in the rest frame of the proton. The scattering angle in the centre of mass frame, θ^*, is related to y via:

$$\cos\theta^* = 1 - 2y \tag{5.5}$$

The kinematics of this process is over constrained by x, y, and Q^2, since they are related by the equation:

$$Q^2 = sxy. \tag{5.6}$$

This thesis describes the search for a scalar particle s-channel resonance produced as shown in figure 5.2. The dynamics of production of such a particle and its subsequent decay are discussed in section 3.4.1. The mass of the resonance can be expressed in the following way:

$$M^2 = (k + xP)^2 \approx xs. \tag{5.7}$$

One other important experimental feature which is used in this thesis is the variable $\delta = E - P_z$, where E and P_z are the total energy and the total longitudinal momentum of an event. Since the ZEUS coordinate system defines the positive z (forward) direction to point in the direction of the outgoing proton, energy and longitudinal momentum for forward moving particles are essentially equal. Hence their contribution to δ cancels to zero. Particles moving in the rear direction have energy and longitudinal momentum of opposite

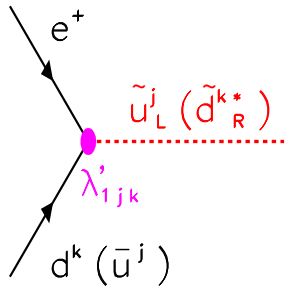

Figure 5.2: *A schematic view of the s-channel resonance production at HERA.*

sign and thus their contribution to δ is twice their energy. δ is a conserved quantity and hence if all possible particle losses in the forward and/or backward beamholes are ignored, δ can be calculated from the initial state and must be equal to that from the final state. By conservation of momentum and energy the difference between the total energy and the total z-component of the momentum is equal to twice the initial electron beam energy:

$$\delta = (E - P_z)_p + (E - P_z)_e \tag{5.8}$$

$$\approx (E_p - E_p) + (E_e - (-E_e)) \tag{5.9}$$

$$= 2E_e = 55 \text{ GeV}. \tag{5.10}$$

Note that particles which escape detection in the forward beam hole would given only a very small contribution to $E - P_z$.

Neutral Current (NC) DIS occurs through the exchange of a photon or Z^0 and is characterized by a positron in the final state. Charged Current (DIS) occurs through the exchange of a W^+ boson and is characterized by missing transverse momentum ($\not{P}_T$) due to the escape of the neutrino from the detector. The NC DIS cross section drops like $1/Q^4$ and the CC DIS cross section ($\frac{d\sigma}{dQ^2} \sim \frac{1}{(Q^2+M_W^2)^2}$) falls off even faster due to the mass of the W boson, M_W, in the cross section formula. This analysis is concerned with events which would populate the kinematic region of high Q^2.

At $Q^2 \sim 0$, the exchanged boson is a real or quasi-real photon, in a process called photoproduction. In such events, the scattered positron disappears into the rear beam pipe and cannot be measured in the main detector. Photoproduction events form the majority of HERA data.

DIS and photoproduction constitute the backgrounds for the physics being searched for in this thesis.

5.1.2 Reconstruction of Kinematical Variables

Table 5.1 defines the notation used in this thesis. Polar angles are measured with respect to the z-axis.

E'	Energy of the final state positron
θ_e	Polar angle of the final state positron
X	Energy of the struck quark
γ	Polar angle of the struck quark
E_e	Constant Energy of the initial positron (27.5 GeV)
E_p	Constant Energy of the initial proton (820 GeV)

Table 5.1: *Notation.*

The scattered positron in the final state provides a handle for recognizing NC DIS for triggering and reconstruction. The electron method[58] for reconstructing the kinematical variables defined in section 5.1.1 makes use of the scattered positron's energy (E') and angle (θ):

$$Q^2_{el} = 2E_eE'(1+\cos\theta_e), \tag{5.11}$$

$$x_{el} = \frac{E_e}{E_p}\frac{E'(1+\cos\theta_e)}{2E_e - E'(1-\cos\theta_e)}, \tag{5.12}$$

$$y_{el} = 1 - \frac{E'}{2E_e}(1-\cos\theta_e). \tag{5.13}$$

The kinematic variables can also be defined in terms of the angles θ_e and γ. This method, which is the method of choice in this analysis, is aptly called the double angle method[58]:

$$Q^2_{DA} = 4E_e^2\frac{\sin\gamma(1+\cos\theta_e)}{\sin\gamma+\sin\theta_e-\sin(\theta_e+\gamma)}, \tag{5.14}$$

$$x_{DA} = \frac{E_e}{E_p}\frac{\sin\gamma+\sin\theta_e+\sin(\theta_e+\gamma)}{\sin\gamma+\sin\theta_e-\sin(\theta_e+\gamma)}, \tag{5.15}$$

$$y_{DA} = \frac{\sin\theta_e(1-\cos\gamma)}{\sin\gamma+\sin\theta_e-\sin(\theta_e+\gamma)}. \tag{5.16}$$

This method has the great advantage that it is insensitive to uncertainties in the calorimeter energy scale to first order. The problem lies in the determination of the γ angle. It can be shown that γ can be calculated via

$$\cos\gamma = \frac{P^2_{T,h} - (E-P_z)^2_h}{P^2_{T,h} + (E-P_z)^2_h}. \tag{5.17}$$

The Jacquet-Blondel method[59] uses the hadronic energy flow of an event to reconstruct the kinematics:

$$y_{JB} = \frac{X(1-\cos\gamma)}{2E_e} = \frac{\Sigma_h(E-p_z)_h}{2E_e} = \frac{\Sigma_h\delta_h}{2E_e}, \tag{5.18}$$

$$Q^2_{JB} = \frac{X^2\sin^2\gamma}{1-y_{JB}} = \frac{(\Sigma_h P_{T,h})^2}{1-y_{JB}}, \tag{5.19}$$

$$x_{JB} = \frac{Q^2_{JB}}{sy_{JB}}. \tag{5.20}$$

where Σ_h is a sum over the hadronic energy in the event. The difficulty of this method is in the determination of X and γ. One does not experimentally directly measure these quantities. In this thesis, jets are used to reconstruct the hadronic final state and hence the summation index on Σ_h is the number of jets. Despite this drawback, the Jacquet-Blondel method provides the only way to reconstruct the kinematical variables for CC DIS and photoproduction where the scattered lepton goes undetected.

5.1.3 Reconstruction of Global Quantities

The following global event quantities are essential in the event selection. The longitudinal energy variable given in equation 5.10 is defined as follows:

$$\delta = E - P_z = \sum_i (E_i - p_{zi}), \tag{5.21}$$

where

$$E_i = \sqrt{p^2_{xi} + p^2_{yi} + p^2_{zi}}. \tag{5.22}$$

The $\not{P}_T$, referred to in the previous section, is magnitude of the vector sum of the transverse momentum and is calculated by

$$\not{P}_T = \sqrt{(\sum_i p_{xi})^2 + (\sum_i p_{yi})^2}, \tag{5.23}$$

and the scalar sum of the transverse energy deposited in the calorimeter is defined as

$$E_t = \sum_i \sqrt{p^2_{xi} + p^2_{yi}}. \tag{5.24}$$

The sums i are over all calorimeter objects. The smallest of such calorimeter objects is a calorimeter cell. However, cells can be clustered together to form islands or jets, which are described in following sections 5.4 and 5.5, and the above variables can defined in terms of those extended objects.

5.2 Track and Vertex Reconstruction

VCTRAK[45] is a fortran package which finds tracks, the primary vertex and secondary vertices for ZEUS events. Each reconstructed track makes use of data in the CTD although information from other tracking devices can also be exploited. For the purposes of this thesis the regular CTD-only tracking and vertexing version was used. VCTRAK is a component of the offline reconstruction program and an optimized version of the same code (limited to CTD only information for purposes of speed) is used online to do the vertex and track finding necessary for the online trigger decisions.

Tracks are first reconstructed in the (x, y) plane and then extended to the z dimension using the z-by-timing and z-stereo information from the CTD. Track candidates begin as a seed, consisting of three hits on an axial outer layer of the CTD, and are swum inward toward the nominal centre of $x = y = 0$. A fourth virtual hit is added at the beam line to aid the track as it is extrapolated inwards gathering additional hits resulting in increasing precision of the track parameters.

The primary vertex is found by first removing any tracks not compatible with originating on the beam line. An initial simple vertex fit is then performed on the remaining tracks which assigns a weight to the (x, y, z) origin of each track. A second and more comprehensive vertex fit is finally performed, in which the direction and curvature of each track are adjusted to the final vertex position.

5.3 Corrections

In the determination of event parameters the energy measurement and its reproducibility in the MC are essential. Energy corrections are necessary since particles originating from the ep collision traverse different materials before reaching the main calorimeter. The measured energy in the calorimeter would thus be reduced by the lost and unrecoverable energy within such material. Other reasons for energy correction include noise, back-splash and shifts in the calorimeter position between years of running.

Calorimeter Noise

The ZEUS calorimeter uses uranium as an absorber as described in section 4.2. The natural radioactivity of the uranium creates noise in the calorimeter and is measured along with the energies coming from the ep interaction. This noise is suppressed by an energy cut of 60(110) MeV for all EMC (HAC) cells [60, 61, 62].

CAL shift

A measured discrepancy between the BCAL and RCAL cell positions was observed between the data and MC and is corrected during reconstruction. The BCAL is shifted in the z-direction by +6.5 mm[63] and RCAL is shifted by +1.1 cm[64] in the z-direction from 1996.

Energy clustering and Island corrections

Measurement of global energy variables based on cells are corrected by factors which are parameterized as a function of some global quantities, usually the global energies themselves. Such a global correction is performed for the hadronic energy deposits in the CAL and corresponds to +5% in BCAL and +2.5% in RCAL (CALCORR[65]).

An improvement in energy resolution can be achieved if a correction were done for each particle [66]. Since each particle coming from the ep interaction can deposit energy in more than one cell, clustering of energy deposits starting from cells is performed. These clusters of calorimeter cells, called islands, gathered around a single local maximum approximate a particle shower in the calorimeter.

These clusters are the islands which were briefly mentioned in section 5.4. The clustering is performed separately in each of the F/B/RCAL and subsequent merging is performed between islands which are deemed to be connected or traverse two CAL sections [67].

One source of deviation from the true energy is loss in inactive material between the interaction point and the surface of calorimeter. As hadrons and electromagnetic particles are expected to behave differently, the islands are split into two categories and separate island corrections are developed based on dead material maps for the different years of ZEUS operation [68, 69]. Corrections are also performed for energy losses in the super-cracks between the F/BCAL and the R/BCAL sections.

Another source of correction arises from back-splash of particles rebounding off the face of the F/BCAL. This so-called albedo effect is illustrated in an event display of a CC MC event in figure 5.3. Albedo causes an enhancement in $(E - P_z)_h$ and thus in the hadronic angle, γ, in equation 5.17. This can have a significant effect on the absolute value and resolution of the kinematic variables, an effect on $(E - P_z)$ of $\mathcal{O}(1)$ GeV [69].

Regularization

The back-splash and energy corrections were not derived with the assumptions of any kinematic constraints. In particular, the following constraints were not imposed:

$$\delta_h = (E - P_z)_h \quad < \quad 2E_e, \tag{5.25}$$

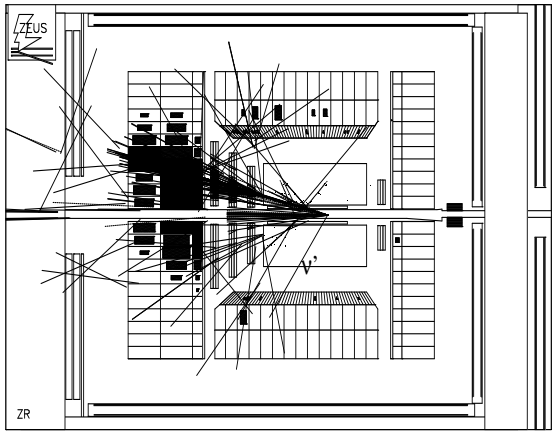

Figure 5.3: *Display of a CC MC event at* $Q^2 \approx 9200$ GeV^2, $y \approx 0.2$ *and* $x \approx 0.5$. *The MC tracks are overlayed.*

$$\frac{P_{T,h}^2}{1 - y_{JB}} \quad < \quad s. \tag{5.26}$$

As a result resolution effects can cause kinematic variables to be calculated, according to the Jacquet-Blondel method, with the previously discussed corrections applied, exceeding their limits. A procedure was developed along with the corrections (`corandcut`[69]) to restrict the Jacquet-Blondel variables to their kinematic limits. The δ_h and $P_{T,h}$ variables used in the subsequent event selection cuts are not regularized. Figure 5.4 illustrates the result of this regularization on the y_{JB} variable for a sample of CC MC events.

5.4 Electron/Positron Finding

A crucial aspect of this analysis is the electron/positron finding. For topologies which include a final state $e^{\pm}$ the need is obvious but in the case of a neutrino in the final state the observation of a $e^{\pm}$ candidate is useful in the reduction of backgrounds. Hence correct and efficient identification of $e^{\pm}$ and precise reconstruction of its position and energy are of vital importance to this search. The reconstruction algorithm used in this analysis is called `em` and is described in [53]. The `em` $e^{\pm}$ finder is based on detailed parameterizations of the detector response for electrons/positrons. Several variables are used to create sub-probability distributions for the calorimeter and CTD. Finally these sub-probabilities are combined into

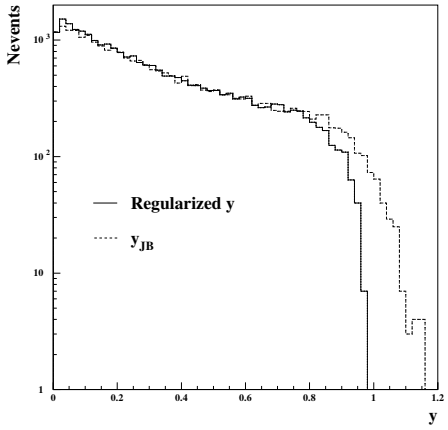

Figure 5.4: y_{JB} *as compared to* $y_{regularized}$ *for a high* Q^2 *CC MC sample.*

a grand probability distribution which can be used as a selection criterion.

The outline of the algorithm is as follows:

1. Cluster the calorimeter cells into islands.
2. Loop over islands and accept an island should it pass the following criteria:
   - The energy of the island is at least 4 GeV.
   - The energy fraction in the HAC section of the calorimeter must be less than 0.3 in FCAL and RCAL and less than 0.5 in BCAL.
   - The calorimeter probability must be greater than 10^{-5}.
3. If the polar angle of the island candidate satisfies $0.3 < \theta < 2.85$ then check for a matching track. Tracks must satisfy the following criteria to be considered:
   - $P_T > 0.1$ GeV
   - The distance of closest approach of the track to the beamline must be less than 2 cm.
   - The distance of closest approach of the track to the island must be less than 50 cm.

- $|\theta^{track} - \theta^{island}| < \pi/4$
- $|\phi^{track} - \phi^{island}| < \pi/4$
- The tracking probability must be greater than 10^{-3}.

4. The grand probability must be greater than 10^{-3}.

Figure 5.5 shows the performance of the EM finding efficiency compared to that of a neural network finder SINISTRA[1]. The finding algorithms are run on NC DIS and photoproduction MC simulations. It should be noted that the EM finder suffers from a slight inefficiency at the regions between the CAL sections. There is also a drop in efficiency outside the CTD acceptance as there is no tracking information to supplement the grand probability determination. In the FCAL and BCAL regions, with the exception of the region inbetween these two CAL sections, the EM finder has a an efficiency of over 97%.

5.5 Jet Finding

Jets are an abstract construction used to relate measurements made at the detector level to a primary particle of a hard scattering process. A large portion of the final states arising from a potential squark decay contains multiple quarks. Jet counting is central to this analysis and will be discussed further in chapter 7 which details the event selection. The number of jets may not directly correspond to the number of partons resulting from a squark decay. A lower number of jets than initial partons can be reconstructed when the energy deposits from two or more partons are not well separated spatially and more jets than partons may be reconstructed due to higher order QCD effects. The latter is the source of background for the multijet states.

The kinematics of the jet are defined by the following equations:

$$E_T^{jet} = \sum E_T^i, \tag{5.27}$$

$$\eta^{jet} = \frac{\sum \eta^i}{E_T^{jet}}, \tag{5.28}$$

$$\phi^{jet} = \frac{\sum E_T^i \phi^i}{E_T^{jet}}, \tag{5.29}$$

where E_T^{jet}, η^{jet} and ϕ^{jet} are the transverse energy, pseudorapidity[2] and azimuthal angle of the jet respectively. The sums can be performed on any calorimeter objects, from cells to

[1] SIRA 5 is a particular implementation of the SINISTRA finder.
[2] $\eta = -\ln\left(\tan\frac{\theta}{2}\right)$, where θ is the polar angle.

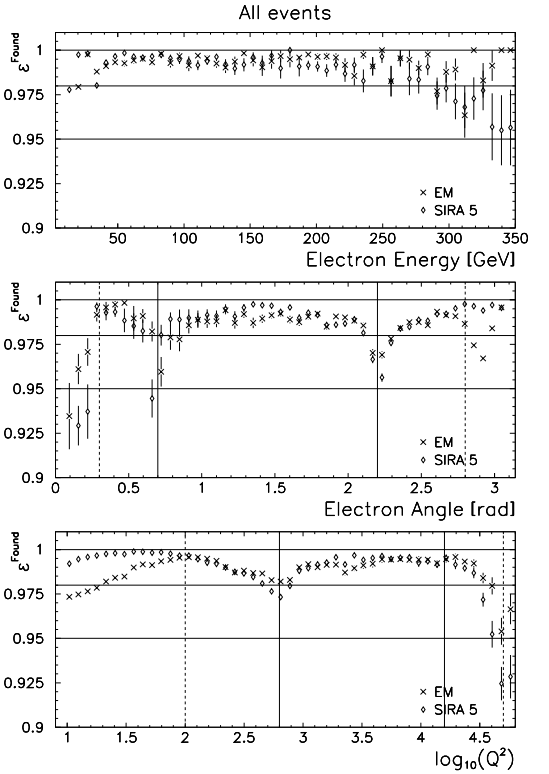

Figure 5.5: *The positron finding efficiency as a function of energy, polar angle and* $\log_{10}(Q^2)$*[70] of the true positron for EM (crosses) and SIRA 5 (diamonds). The inner vertical lines indicate the CAL limits and the outer vertical lines indicate the CTD limits.*

islands which belong to a particular jet. In this analysis, the jet finding is performed on the corrected islands.

The jet reconstruction algorithm used in this thesis is the longitudinally invariant K_T algorithm which is described in the literature [71, 72]. The algorithm works by calculating a distance measure,

$$d_{ij}^2 = (\Delta\eta_{ij}^2 + \Delta\phi_{ij}^2)\min(E_{Ti}, E_{Tj}), \tag{5.30}$$

and

$$d_i^2 = E_{Ti}^2 \tag{5.31}$$

for each pair of objects. The minimum of (d_{ij}^2, d_i^2) is found. If the minimum is d_i^2, then the object i is removed from the list and called a jet. Otherwise the objects i and j are merged by the E_T weighted recombination scheme given in equations 5.27-5.29.

5.6 Squark Mass Reconstruction

The squark mass reconstruction methods use reconstructed jets, which take the corrected islands described in section 5.3 as input to the jet algorithm. The longitudinal conservation of energy in equation 5.10, $\delta = 55$ GeV, is also assumed in their derivation.

5.6.1 Channels with a $e^{\pm}$ in the final state

The mass of the squark is reconstructed as follows:

$$\begin{aligned} M_{ejets}^2 &= (E - P_z)(E + P_z) && (5.32)\\ M_{ejets}^2 &= 2E_e(E + P_z), && (5.33)\end{aligned}$$

where $(E + P_z)$ is calculated using the $e^{\pm}$ candidate and the reconstructed jets and E_e is the initial e-beam energy.

5.6.2 Channels with a ν in the final state

The $\not{P}_T$ is attributed to the ν in the final state such that:

$$\begin{aligned} p_{x,\nu} &= -p_{x,\nu}^{meas}, && (5.34)\\ p_{y,\nu} &= -p_{y,\nu}^{meas}, && (5.35)\\ p_{t,\nu}^2 &= (p_t^2)^{meas}, && (5.36)\\ E_\nu - p_{z,\nu} &= 2E_e^{beam} - (E - p_z)^{meas}, && (5.37)\\ E_\nu &= \sqrt{p_{t,\nu}^2 + p_{z,\nu}^2}. && (5.38)\end{aligned}$$

The right hand side of equations 5.34, 5.35 and 5.37 are measured. Since the right hand side of equation 5.37 is a constant, A, for each event, then from equations 5.37 and 5.38, a relation for $p_{z,\nu}$ can be derived as follows:

$$\begin{aligned} p_{z,\nu} &= \sqrt{p_{t,\nu}^2 + p_{z,\nu}^2} - A && (5.39)\\ p_{z,\nu}^2 + A^2 + 2p_{z,\nu}A &= p_{t,\nu}^2 + p_{z,\nu}^2 && (5.40)\\ p_{z,\nu} &= \frac{p_{t,\nu}^2 - A^2}{2A} && (5.41)\\ p_{z,\nu} &= \frac{p_{t,\nu}^2 - (E_\nu - p_{z,\nu})^2}{2(E_\nu - p_{z,\nu})}. && (5.42)\end{aligned}$$

Hence the mass of the squark can derived:

$$\begin{aligned} M_{\nu jets}^2 &= (E^2 - p_z^2) && (5.43)\\ M_{\nu jets}^2 &= (E - p_z)(E + p_z) && (5.44)\\ M_{\nu jets}^2 &= 2E_e((E + p_z) + (E_\nu + p_{z,\nu})), && (5.45)\end{aligned}$$

where

$$\begin{aligned} (E_\nu + p_{z,\nu}) &= (E_\nu - p_{z,\nu}) + 2p_{z,\nu} && (5.46)\\ (E_\nu + p_{z,\nu}) &= A + \frac{2((p_t^2)^{meas} - A^2)}{2A} && (5.47)\\ (E_\nu + p_{z,\nu}) &= \frac{(p_t^2)^{meas}}{A} && (5.48)\\ (E_\nu + p_{z,\nu}) &= \frac{(p_t^2)^{meas}}{2E_e(1 - y)}. && (5.49)\end{aligned}$$

Substituting equation 5.49 into 5.45, the invariant mass of the ν and jets system can be expressed in terms of measurable quantities.

$$M_{\nu jets}^2 = 2E_e((E + P_z) + P_T^2/(2E_e(1 - y))), \tag{5.50}$$

where $(E + P_z)$ is calculated using the reconstructed jets and y is regularized, as described in section 5.3, to be less than 1.

Chapter 6

Monte Carlo Simulation

Monte Carlo (MC) simulations play an essential role in planning and analyzing high energy scattering experiments. It allows for the designing of selection cuts and calculation of the acceptances. A Monte Carlo generator simulates physics by creating events according to probabilities of the desired process cross section and provides event distributions based on an underlying theory. Since the experimental setup is not perfect and imposes cuts in phase space, which are in general quite complicated and cannot be treated analytically, MC techniques allow for the study of physics processes on a statistical basis. Generating events is but the first step of the complete simulation as other programs are subsequently used to simulate the interaction of the final state particles with the detector and the behaviour of the trigger.

6.1 Background Simulation

The dominant background to e^+q, $e^\pm qqq$, and $e^\pm qqqq$ final states is NC DIS. For the e^+q final state, the background is due to hard $2 \to 2$ scatters between the high-x quarks and the positron. Backgrounds to the multijet final states occur in NC DIS events with higher order QCD effects. The background to topologies containing an e^- is quite small, since it occurs only if the positron charge is wrongly reconstructed. Additional small backgrounds can come from photoproduction (γp or php) processes if a fake positron is identified in the hadronic final state.

The primary background to ν multijet topologies is CC DIS with again small additional background from photoproduction events for which the measured transverse momentum is large due to mismeasured jet energy, final state muons or neutrinos.

The background samples considered are summarized in the table 6.1.

HERACLES 4.5.2[73], which simulated electroweak radiative effects, interfaced with

Generator	Process	Generator Cut	Events Generated	Luminosity pb^{-1}
DJANGO	NC DIS	$Q^2 > 400$ GeV^2	137237	126.8
		$Q^2 > 1250$ GeV^2	24642	136.4
		$Q^2 > 2500$ GeV^2	11641	219.0
		$Q^2 > 5000$ GeV^2	11894	912.8
		$Q^2 > 10000$ GeV^2	11991	5173.4
DJANGO	CC DIS	$Q^2 > 10$ GeV^2	24742	596.0
		$Q^2 > 5000$ GeV^2	14842	5890.8
		$Q^2 > 10000$ GeV^2	4987	10396.1
		$Q^2 > 20000$ GeV^2	4913	151169.2
HERWIG	PHP Resolved	$P_t^{hard} > 8$ GeV, $E_T > 50$ GeV	14886	118.9
HERWIG	PHP Direct	$P_t^{hard} > 8$ GeV, $E_T > 50\ GeV$	9839	38.5

Table 6.1: *Summary of generated background Monte Carlo samples.*

DJANGO 6.24[74] to hadronization programs was used to simulate the backgrounds coming from NC and CC DIS. The hadronic final state is simulated using the Color-Dipole Model as implemented in ARIADNE[75] for the QCD cascade. The CTEQ4[76] parton density parameterizations were used. The parton densities are an essential part of the cross section calculation as in the cross section equation 3.11.

Photoproduction events were simulated using the HERWIG generator [77]. A distinction is made between two types of photoproduction, direct and recolved, both of which were simulated and illustrated in figure 6.1. In the direct case of photoproduction the all the energy of the photon participates in the hard scatter whereas in the resolved case only a fraction of the photon's momentum, associated a partonic constituent of the photon, participates in the hard subprocess.

6.2 SUSY Simulation

Over 400 signal MC sets were generated using a modified version of SPYTHIA[3] and SUSYGEN 3.0[78]. The decay $\tilde{q} \to e^+q$ was simulated with PYTHIA 6.2[79]. These sets are summarized in tables 6.2 and 6.3.

In an attempt to cover the SUSY phase space, several points were selected to generate as they encompassed the relevant gaugino mass space, as illustrated by figure 6.2. At each

Generator	M_2 (GeV)	μ (GeV)	$M_{\tilde{q}}$ Range (20 GeV intervals)	Topology
SPYTHIA 2.2	90	-200	100-280	$\tilde{q} \to q\tilde{\chi}_1^0 \to (e^{\pm}, \nu)qqq$
SPYTHIA 2.2	90	-200	120-280	$\tilde{q} \to q(\tilde{\chi}_2^0, \tilde{\chi}_1^{\pm}) \to (e^{\pm}, \nu)qqq(qq)$
SPYTHIA 2.2	190	-200	120-280	$\tilde{q} \to q\tilde{\chi}_1^0 \to (e^{\pm}, \nu)qqq$
SPYTHIA 2.2	190	-200	200-280	$\tilde{q} \to q(\tilde{\chi}_2^0, \tilde{\chi}_1^{\pm}) \to (e^{\pm}, \nu)qqq(qq)$
SPYTHIA 2.2	290	-200	160-280	$\tilde{q} \to q\tilde{\chi}_1^0 \to (e^{\pm}, \nu)qqq$
SPYTHIA 2.2	290	-200	220-280	$\tilde{q} \to q(\tilde{\chi}_2^0, \tilde{\chi}_1^{\pm}) \to (e^{\pm}, \nu)qqq(qq)$
SUSYGEN 3.0	100	-60	100-280	$\tilde{q} \to q\tilde{\chi}_1^0 \to (e^{\pm}, \nu)qqq$
SUSYGEN 3.0	100	-60	100-280	$\tilde{q} \to q(\tilde{\chi}_2^0, \tilde{\chi}_1^{\pm}) \to (e^{\pm}, \nu)qqq(qq)$
SUSYGEN 3.0	130	-200	100-280	$\tilde{q} \to q\tilde{\chi}_1^0 \to (e^{\pm}, \nu)qqq$
SUSYGEN 3.0	130	-200	160-280	$\tilde{q} \to q(\tilde{\chi}_2^0, \tilde{\chi}_1^{\pm}) \to (e^{\pm}, \nu)qqq(qq)$
SUSYGEN 3.0	310	-100	100-280	$\tilde{q} \to q\tilde{\chi}_1^0 \to (e^{\pm}, \nu)qqq$
SUSYGEN 3.0	310	-100	140-280	$\tilde{q} \to q(\tilde{\chi}_2^0, \tilde{\chi}_1^{\pm}) \to (e^{\pm}, \nu)qqq(qq)$
SUSYGEN 3.0	310	-140	140-280	$\tilde{q} \to q\tilde{\chi}_1^0 \to (e^{\pm}, \nu)qqq$
SUSYGEN 3.0	310	-140	180-280	$\tilde{q} \to q(\tilde{\chi}_2^0, \tilde{\chi}_1^{\pm}) \to (e^{\pm}, \nu)qqq(qq)$
SUSYGEN 3.0	310	-180	160-280	$\tilde{q} \to q\tilde{\chi}_1^0 \to (e^{\pm}, \nu)qqq$
SUSYGEN 3.0	310	-180	200-280	$\tilde{q} \to q(\tilde{\chi}_2^0, \tilde{\chi}_1^{\pm}) \to (e^{\pm}, \nu)qqq(qq)$

Table 6.2: *Summary of generated signal Monte Carlo samples with multijet final states.*

Generator	$M_{\tilde{q}}$ Range (20 GeV intervals)	Topology
PYTHIA 6.104	100-280	eq

Table 6.3: *Summary of generated signal Monte Carlo samples with single jet final states.*

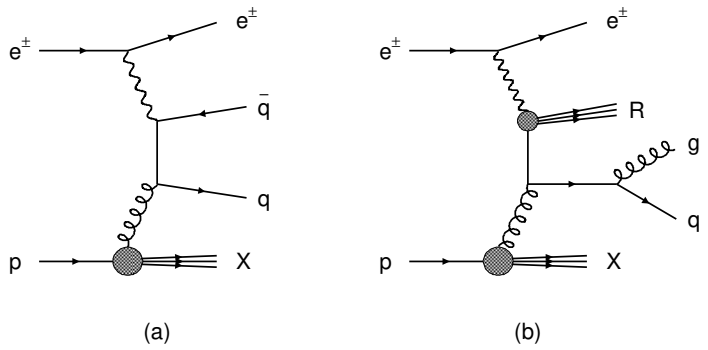

Figure 6.1: *Examples of leading order diagrams for (a) direct and (b) resolved photoproduction processes. The proton remnant is labelled R.*

selected phase space point, each topology was simulated at squark masses ranging from 100 GeV to 280 GeV. These simulations allowed the determination of the signal selection efficiencies. The efficiencies are sensitive to the masses of the particles potentially decaying in the ZEUS detector. Hence, by simulating each topology listed in table 3.3 for several squark masses, one can determine the efficiencies as a function of the squark mass. Moreover, by selecting points in the mass planes $(\tilde{\chi}_1^0, \tilde{\chi}_1^{\pm})$ and $(\tilde{\chi}_1^0, \tilde{\chi}_2^0)$ one can indirectly scan the SUSY parameter space of $(M_2, \mu, \tan\beta)$. Recall that the masses of the gauginos are fixed by a particular choice of M_2, μ and $\tan\beta$. Strategically choosing points to lie on the extremities of the possible mass states permits the interpolation of efficiencies at non-simulated points in the SUSY phase space. Hence, a scan in the SUSY phase space can be performed.

SPYTHIA

SPYTHIA is a subset of the PYTHIA 6.2 generator. SPYTHIA simulates particle production in the MSSM and does not include $\not{R}_p$ processes. Moreover there is no process for sparticle production at ep colliders. Fortunately, PYTHIA provides several ways for including new processes and/or new particles. PYTHIA contains the code to simulate the production of a scalar leptoquark through the fusion of an $e^{\pm}$ and a quark in ep collisions. This is the same process required to produce a squark via $\not{R}_p$ at HERA. This process is used and as PYTHIA facilitates the inclusion of new decay modes, the decays to SUSY particles are

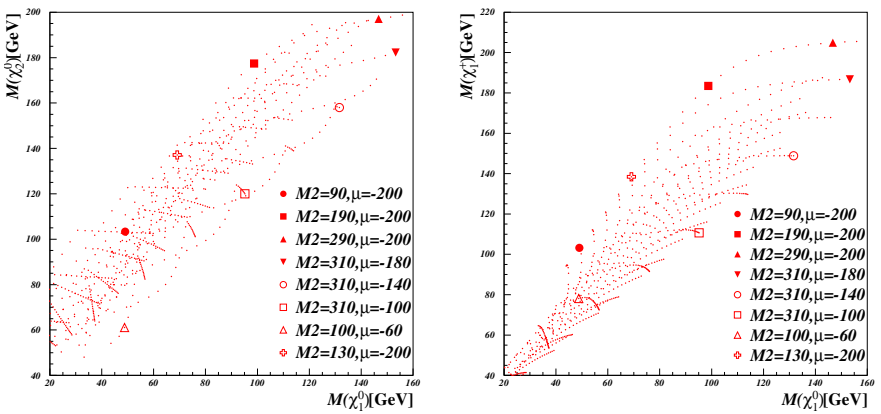

(a) (b)

Figure 6.2: *Each small dot represents a point in a grid which covers the* (M_2, μ) *region defined by* $|\mu| < 200$ GeV *and* 80 GeV $< M_2 < 310$ GeV *at* $\tan\beta = 2, 10$. *The large symbols indicate where signal Monte Carlo sets are generated. (a) In the* $M_{\tilde{\chi}_2^0}$ *vs* $M_{\tilde{\chi}_1^0}$ *plane and (b) in the* $M_{\tilde{\chi}_1^\pm}$ *vs* $M_{\tilde{\chi}_1^0}$ *plane.*

added. As SPYTHIA contains only MSSM decays the LSP was forced to be stable by setting the particle's width to zero. This was bypassed in the routine which initializes the SUSY sector of the generator.

All relevant information, such as widths, lifetimes and branching ratios must be provided in the form of supplementary particle data used to define new decays. This can be done using any number of other programs which calculate the needed information. SUSYGEN, which is briefly described in the following section, was used for such separate information. No special matrix element treatment code is provided to perform the $\not{R}_p$ decay. The decays are performed via phase space. The cross sections do not take into account the interference between different processes[3].

SUSYGEN

The SUSYGEN package, initially written to study SUSY events in e^+e^- colliders, was extended by E.Perez[80] to cover HERA's processes. Like SPYTHIA almost any process can be generated except that it performs all two or three body SUSY decays according to full

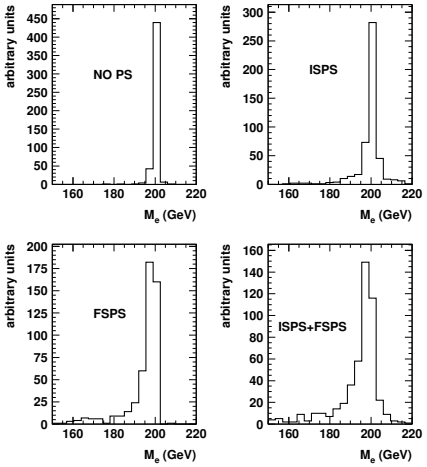

Figure 6.3: *Effect of initial and final state parton showers on the mass reconstruction of a* 200 *GeV squark undergoing the* $\not{R}_p$ *decay* $\tilde{q} \to eq$. *ISPS and FSPS refer to initial and final state parton showers respectively.*

matrix elements. The matrix elements for each hard subprocess are given in [78]. SUSYGEN provides useful routines to calculate the spectrum of SUSY particle masses, decay widths and cross sections. Also t-(u) channel slepton (squark) exchange in the $eq \to q + \tilde{\chi}_n^0$ process is included.

Both SPYTHIA and SUSYGEN implement initial and final state partons showers which have the effect of broadening the mass distribution M_e ($M_e = \sqrt{x_e s}$) of the squark as seen in figure 6.3.

Nevertheless, given the widths and branching ratios, SPYTHIA calculates the cross sections in agreement[3] with SUSYGEN, as shown in figure 6.4.

6.3 Detector Simulation

The generated events were input into the ZEUS detector simulation called MOZART[29] which is based on the GEANT 3.13[81] CERN package. It simulates the passage of particles though all the components of the ZEUS detector. Finally, the trigger is simulated by the ZGANA[82] package. The full offline reconstruction of an event is performed by the software package ZEPHYR[29], which takes all calibration constants into account and treats data and

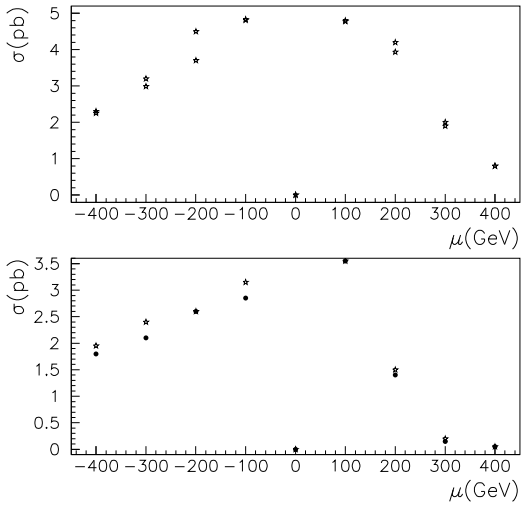

Figure 6.4: $\sigma(e^+d \to q\tilde{\chi}_1^0)$ *as a function of the SUSY parameter* μ. *Black points refer to SUSYGEN and open stars refer to SPYTHIA. Both plots keep* $M_{\tilde{q}} = 200$ *GeV tan*β*=2.0. Above:* $M_2 = 50$ *GeV. Below:* $M_2 = 100$ *GeV.*

Monte Carlo simulation in the same way.

Chapter 7

Event Selection

The analysis focused on two classes of events. One class contains a reconstructed electron or positron and hence will be called NC-like. In the other class of events, the final state lepton is a neutrino; thus the signature is characterized by missing transverse momentum ($\not{P}_T$) and this class will be called CC-like. In either case, one is searching for a high mass resonance and thresholds for cuts on E_T and $\not{P}_T$ can be set high, since high thresholds would not affect a potential signal while significantly reducing background contamination.

7.1 Search Strategy

After selecting high Q^2 NC and CC DIS topologies, the jet requirements are then of utmost importance. They provide the greatest discriminant between the signal and major background sources. The cascade squark decays contain three to five quarks which at the detector level translate into a sharp peak at two or more good jets (figure 7.1). Moreover, the jets have high E_T, whose mean increases with increasing squark mass. A good jet is defined to have $\eta < 2.5$ and $E_T > 10$ GeV. The NC and CC events peak at one reconstructed jet and fall sharply as shown in figure 7.2. Hence, the key cut in extracting the cascade squark decay topologies is to require at least two well reconstructed jets of significant E_T.

One would expect a peak at one good jet for direct $\not{R}_p$ squark decays (see figure 7.3), since there are only two partons in the final state: a positron and a quark. This is the same final state expected from NC DIS. However, the E_T of both partons will have higher E_T than their cascade counterparts.

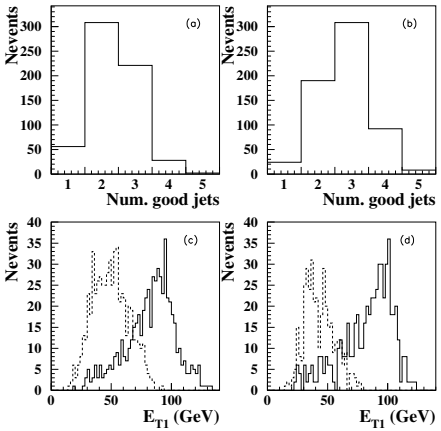

Figure 7.1: *Above: the number of good jets reconstructed in MC simulations for (a) the eqqq final state and (b) the eqqqqq final state. Below: the E_T distribution of the highest E_T jet for (c) the eqqq final state and (d) the eqqqqq final state. The dashed histogram represents squarks with a mass $M_{\tilde{q}} = 160$ GeV and the solid histogram represents squarks with a mass $M_{\tilde{q}} = 260$ GeV.*

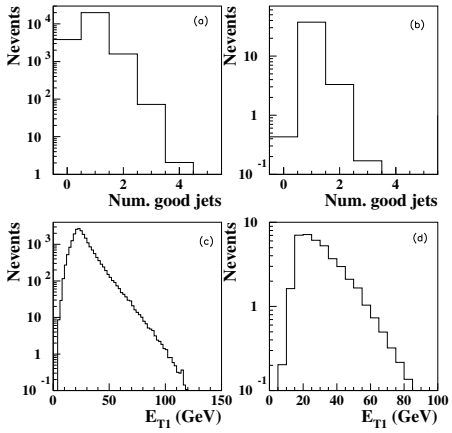

Figure 7.2: *The number of good jets reconstructed in MC simulations for NC and CC DIS are shown in (a) and (c) respectively. The E_T distributions of the highest E_T jet for NC and CC DIS are shown in (b) and (d) respectively.*

7.2 Cut Optimization

In the following event selection, described in the next sections, some cuts are said to be optimized. The optimized variables determine the final efficiency, ϵ, of a signal. They are set to maximize the acceptance of the signal while minimizing DIS background so that the best cross section limit, σ_{limit}, is obtained. The value of σ_{limit} depends on the number of data events. However, in deriving the cuts one must not be biased by foreknowledge of the data distributions, as one may formulate a cut to enhance or suppress a possible signal. The chosen variables must be optimized using only Monte Carlo simulation. The way in which this optimization occurs is by finding the average cross section limit, $< \sigma_{limit} >$:

$$< \sigma_{limit} > = \sum_{N_{obs}=0}^{\infty} P(N_{obs}, \mu)\sigma_{limit}(N_{obs}), \tag{7.1}$$

$$P(N_{obs}, \mu) = e^{-\mu}\frac{\mu^{N_{obs}} N_{obs}}{N_{obs}!}, \tag{7.2}$$

where N_{obs} is the number of observed events and μ is the number of expected events from background Monte Carlo simulation. The mean limit is a Poisson-weighted sum over all possible N_{obs} and is independent of the data. The $\sigma_{limit}(N_{obs})$ is the cross section limit which is discussed in chapter 8 and defined in equation 8.5. This procedure is repeated, for the

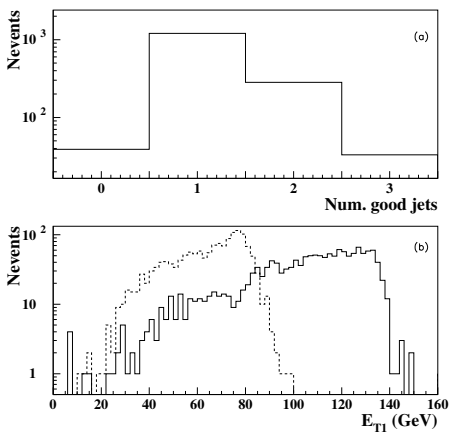

Figure 7.3: *(a) The number of good jets for an eq final state (b) The E_T of the highest E_T jet for an eq final state. The dashed histogram represents squarks of mass $M_{\tilde{q}} = 160$ GeV and the solid histogram represents squarks of mass $M_{\tilde{q}} = 260$ GeV.*

cut variable to be optimized, for each squark mass, resulting in a selection cut which is dependent on the reconstructed invariant mass in the detector.

7.3 NC-like

The NC-like events are selected primarily by the identification of a final state electron or positron and secondly by high global E_T. At the next level of selection the subsequent data set is segmented into multijet and single jet events. Finally, the charge of the $e^{\pm}$ candidate is used to partition the remaining sample.

7.3.1 Preselection

After events survive the three levelled trigger system, a process of reconstruction takes place. At this stage a new level of filters are applied to the data and the results are classified in Data Summary Tapes (DST). These DSTs form additional bits which can be used as a first selection or preselection requirement in offline analyses. The following selection cuts form the first pass over the data to select well reconstructed events of high E_T.

- DST (35 or 36) and 38
  DST bit 35 selects events with $E_T > 20$ GeV calculated from islands.
  DST bit 36 selects events with $E_T > 30$ GeV calculated from the UCAL cells.
  DST bit 38 selects events with $E_{RCAL} < 5$ GeV calculated from the RCAL cells.
  .

- Vertex requirement
  A tracking vertex is required, which must satisfy $|Z_{vtx}| < 50$ cm. This confines the vertex to the central region of the detector.

- $(E_T)_{uncorrected} > 40$ GeV and $(E - P_z)_{uncorrected} > 30$ GeV
  A preselection is made for events with high E_T and high $E - P_z$ in order to preferentially select high E_T NC DIS while removing a large fraction of photoproduction (php). These variables are calculated from the raw calorimeter energies without any corrections applied.

7.3.2 Further NC Selection

Having selected a high E_T event sample, the following cuts were applied to select high mass NC events:

- $(E - P_z) > 44$ GeV
  A harsh cut for removing photoproduction.

- A *good* electron/positron found
  - $E_e > 15$ GeV with an `em` probability > 0.001
  - $E_{iso}(R = 0.25) < 1$ GeV
    The candidate must be isolated. The energy inside a cone of radius $R = \sqrt{\Delta\eta^2 + \Delta\phi^2} = 0.25$ in (η, ϕ)-space not attributed to the electromagnetic cluster should be less than 1 GeV. This is a less strict isolation criteria than that used in a standard NC DIS $e^{\pm}$ search (see appendix A.2) because in a squark cascade decay the $e^{\pm}$ comes from a multiparton secondary decay of a gaugino.
  - $\theta_e > 0.3$ rad and a matching track with $P_T^{track} > 2$ GeV which has a distance of closest approach (DCA) to the energy cluster $DCA < 8$ cm
    OR
    $\theta_e < 0.3$ rad and $P_T^e > 30$ GeV

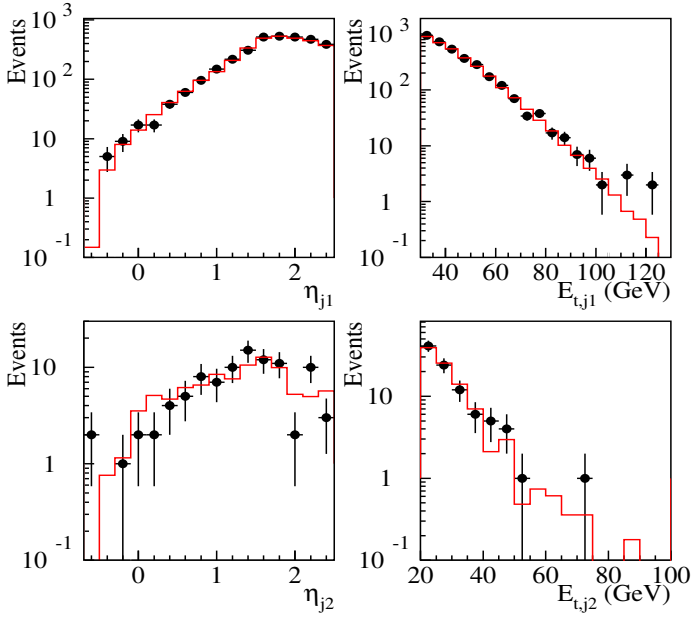

Figure 7.4: *Distributions of jet variables for the preselected sample. Above: the pseudorapidity (η) and transverse energy (E_T) for the highest E_T jet. Below: the pseudorapidity (η) and transverse energy (E_T) for the second highest E_T jet. The points with error bars are the data. The histogram is the total expected background (NC+php). The background histogram is normalized to the data luminosity.*

- Mass $>$ 100 GeV
  This analysis is only concerned with high mass events, as calculated by equation 5.33. This cut effectively removes low Q^2 NC DIS backgrounds.

The control plots 7.4 and 7.5 are made with an additional cut requiring at least one reconstructed jet with $\eta_{j1} < 2.5$ and $E_{T,j1} > 30$ GeV. In the data 3346 events were selected while 3270 events were expected from NC DIS and php backgrounds. The data shown in the control plots is in good agreement with expectations. As seen in figure 7.6, the observed invariant mass spectrum agrees with MC simulation reasonably well up to about 210 GeV, where there is somewhat of an excess. These events can be characterized as single jet events and low y.

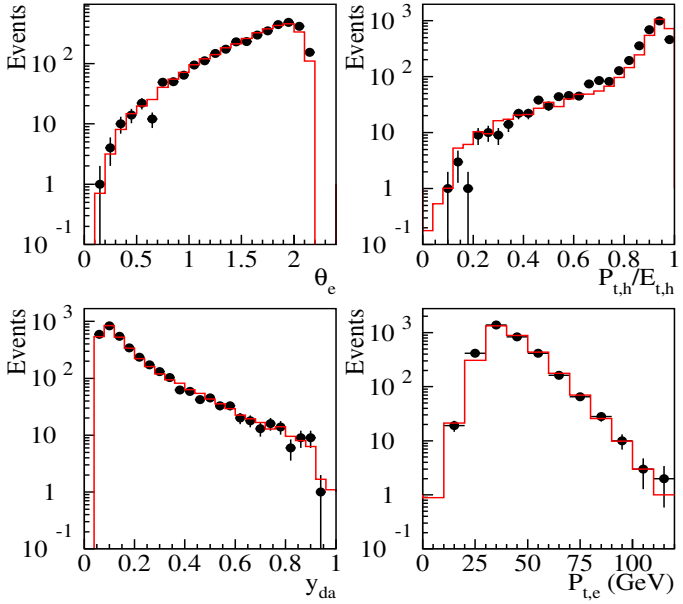

Figure 7.5: *Distributions of kinematic variables for the preselected sample. Above: the polar angle of the positron candidate (θ_e) and the ratio of the transverse momentum ($P_{T,h}$) to the transverse energy ($E_{T,h}$) for the hadronic final state. Below: the variable y, calculated using the double angle method (y_{DA}), and the transverse momentum of the electron candidate ($P_{T,e}$). The points with error bars are the data. The histogram is the total expected background (NC+php). The background histogram is normalized to the data luminosity.*

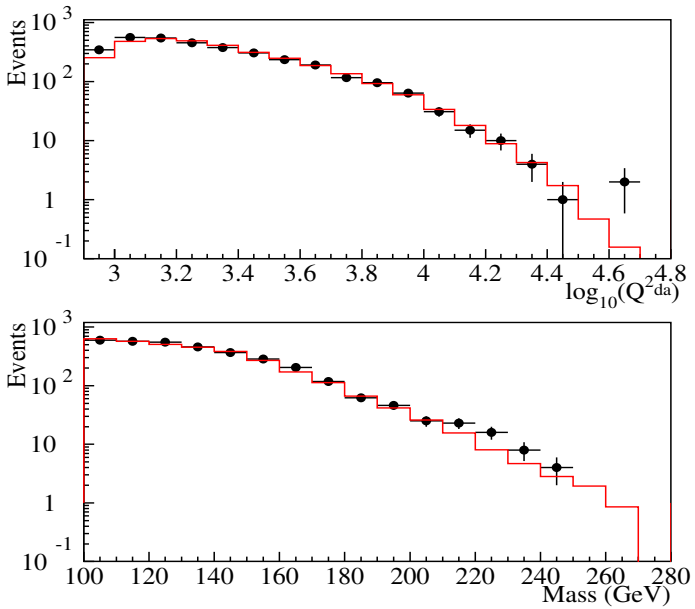

Figure 7.6: *Above: distribution of* $\log_{10}(Q^2)$*, calculated using the double angle method for the preselected sample. Below: the reconstructed mass distribution for the preselected sample. The points with error bars are the data. The histogram is the total expected background (NC+php). The background histogram is normalized to the data luminosity.*

7.3.3 Jet Cuts

As previously mentioned, most of the topologies under investigation contain more than two jets. Having selected a sample of high mass NC events, the jet signal characteristic is exploited in order to search for possible signals in the data beyond what is expected from the SM processes.

If the following cut is satisfied then the event is put in the e jets sample; otherwise, the event is placed in the e jet sample.

- At least two *good* jets are required.
  A good jet is defined to be one with $\eta > 2.5$ and at least 10 GeV in E_T.
  - $\eta_{j1} < 2.5$ and $E_{T,j1} > E_T(M_{inv})$
    The highest E_T jet has to pass an optimized jet cut as a function of the invariant mass of the e jet(s) system. The cut is illustrated in figure 7.7. It starts at $\sim$ 18 GeV at 100 GeV and reaches a plateau of $\sim$ 50 GeV above 200 GeV. The net affect of this cut is an increase in the acceptance for lower reconstructed invariant mass, in events with two or more jets.
  - $\eta_{j2} < 2.5$ and $E_{T,j2} > 15$ GeV
    The second highest E_T jet must have significant E_T.

With multiple jets in the final state the jets would tend to have lower E_T than in the single jet final state. Even if a real squark cascade decay does not pass the above criteria, it may nevertheless pass the e jet selection. In this way, cascade decays which do not pass the e jets selection may survive, thereby increasing the overall squark acceptance.

7.3.4 e jet Sample

A squark decaying via $\not{R}_p$ will optimally only have a positron and a jet in the final state. As a result, the E_T of the decay positron and jet will be very high. The cuts used for this sample were:

- At least 1 jet with $\eta_1 < 2.5$ and $E_{T,j1} > 30$ GeV
- $P_T^e > 30$ GeV
- $y_{DA} > y(M_{inv})$
  A scalar particle has a flat y distribution as seen in figure 7.8. This is an optimized cut to further suppress the NC background.

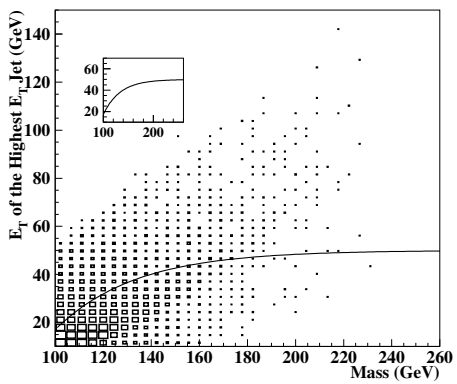

Figure 7.7: *The E_T distribution of the highest E_T jet as a function of the invariant mass of the e + jet(s) system. The curve indicates the optimized jet E_T cut. Events above the cut survive. The inlay depicts the cut for clarity.*

These cuts were derived from the search for a high mass e+jet leptoquark resonance search at ZEUS[83]. The events resulting in the excess mentioned earlier (see figure 7.6) fall into this e jet sample since they contain only one jet. Their y distribution, peaked at low y, is not consistent with that of the decay of a scalar resonance, which is flat. They are removed by the final optimized y (see figure 7.8) cut.

7.3.5 e jets Sample

In this category, the event contains at least two jets of high E_T and a high P_T $e^{\pm}$ candidate. The following additional cuts are designed to further promote multijet events:

- $P_T/E_T < 0.75$
  Single jet events peak at $P_T/E_T = 1$.

- $Q^2_{DA} > 800$ GeV^2
  Since the $e^{\pm}$ arising from a secondary decay of a gaugino is predominantly reconstructed in the BCAL or FCAL, the effective Q^2 due to the polar angle of the $e^{\pm}$ is very large. See figure 7.9. The mean effective Q^2 increases with the reconstructed squark mass.

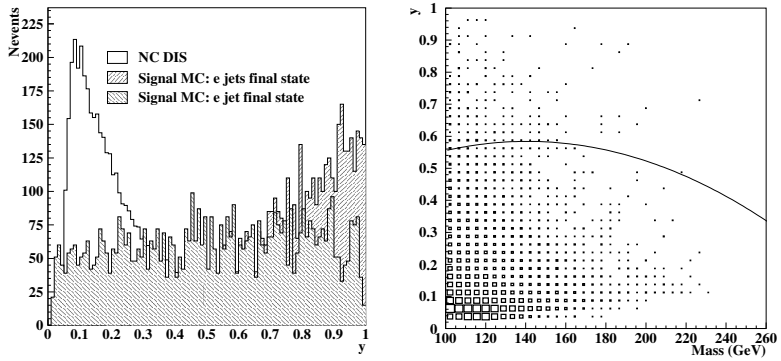

(a) (b)

Figure 7.8: *(a) The y distribution for NC DIS compared to a sample cascade decay (e jets) and a sample $\not{R}_p$ decay (e jet) with arbitrary normalizations. (b) The optimized y cut as a function of the invariant mass. Events above the curve survive.*

- $0.4 < y_{DA} < 0.95$
  As illustrated in figure 7.8(a), multijet events of high invariant mass peak at high y. Conversely, the main source of background, high Q^2 NC, peaks at low y, so the lower y acts as a very good discriminant between signal and background. The upper cut on y is applied to remove photoproduction events where fake $e^{\pm}$ candidates in the very forward region contaminate the sample.

The resulting data set is finally segmented by the charge of the identified lepton. Should the charge of the lepton candidate be identified as negative, it is classified as an e^-jets event, otherwise it is classified as an e^+jets candidate. A track is deemed to be negative if it should satisfy the following conditions:

- Vertex Refitted Track

- The track must have hits in at least the 1st superlayer and the 3rd superlayer
  If a track does not have hits in at least the first three superlayers, the curvature and momentum measurements from the CTD are no longer sufficiently accurate[84]. The longer the track the better several track properties become. For example, the momentum resolution improves with the square of the track.

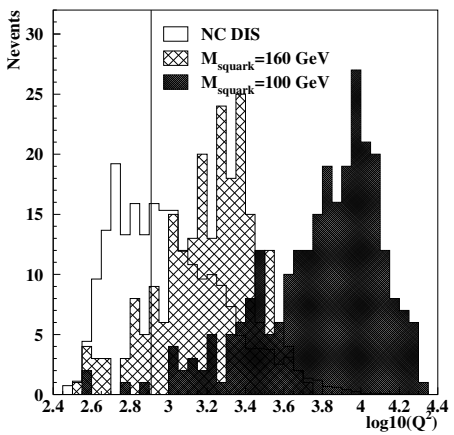

Figure 7.9: *The $\log_{10}(Q^2)$ distribution for NC DIS compared to that of a cascade squark with arbitrary normalization. The cut is indicated by the line in the figure.*

- The track charge must be negative at the 3σ level

No e^- candidate was selected from the data.

7.3.6 Selection Efficiencies and Squark Mass Resolutions

The efficiencies for cascade squark decays are illustrated in figure 7.10. They range from 30% to 60% from squark masses of 100 GeV to 280 GeV. The mass resolution (figure 7.11) for the cascade squark decays ranges from $3-7$ GeV, slightly larger than the $\not{R}_p$ squark decay resolutions which range from $2.5-4$ GeV.

7.3.7 Final NC-like Event Samples

The numbers of observed events in the three NC-like channels were in agreement with the expectations from SM background and are summarized in table 7.1. No overall excess of events is observed and no sign of a mass peak appears in figures 7.12 and 7.13, which show the invariant mass distributions for the e jet and e jets reconstructed channels respectively. These distributions are an important result. They show that the physics of the multijet topologies being considered is well described by the SM.

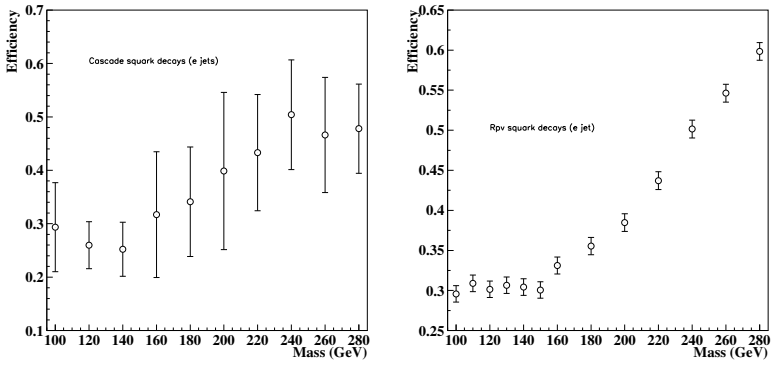

(a) (b)

Figure 7.10: *(a) The efficiencies for cascade squark decays into e jets as a function of the squark mass. (b) The efficiencies for the $\not{R}_p$ squark decays as a function of the squark mass. The range of efficiencies over the generated SUSY phase space points at each mass is shown.*

Reconstructed Channel	N_{obs}	N_{exp}
e jet	70	82 ± 6
e^+ jets	66	74.2 ± 5
e^- jets	0	0.20 ± 0.01

Table 7.1: *Summary of data sample event numbers compared to expected background from NC DIS (Ariadne) and php (Herwig Resolved and Direct $E_T > 50$ GeV).*

7.4 CC-like

The selection of CC-like events is not as clean as NC-like events. There is a lot of contamination from non-ep processes due to the requirement of an imbalance of energy ($\not{P}_T$). This background is comprised of cosmic and beam halo induced muons and events containing sparking calorimeter cells, and has already been discussed in section 4.3.2. The trigger itself rejects some of the more obvious background events, but rejection becomes complicated when these events overlap legitimate ep processes. In general, such events have an extremely localized large energy deposit, usually all in a single cell, creating the $\not{P}_T$.

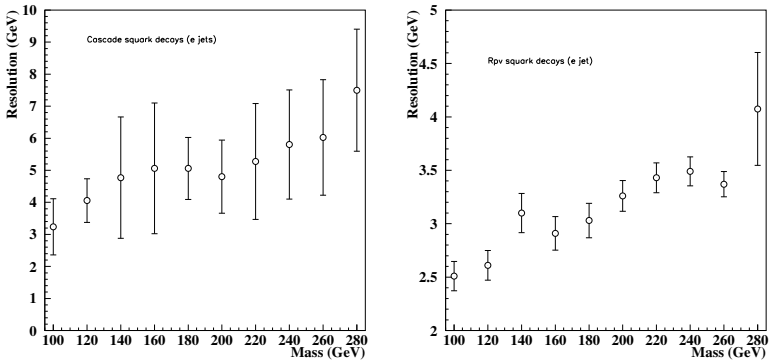

(a) (b)

Figure 7.11: *(a) The mass resolution for cascade squark decays into e jets as a function of the squark mass. (b) The mass resolution for the $\not R_p$ squark decays as a function of the squark mass. The range of resolutions over the generated SUSY phase space at each mass is shown.*

7.4.1 Cleaning cuts

This section details cuts which remove non-ep events. These are events arising from beam-gas, halo or cosmic muons or detector hardware problems, which are sufficiently like ep events to pass through the trigger and DAQ chain. The following cuts were used:

- $0.5 < \not P_T{}^{good} / \not P_T < 2$
  Sparks in cells overlapping with an ep process give a large $\not P_T$, and would become backgrounds. Isolated cells with a bad energy imbalance are removed from the $\not P_T$ calculation described in equation 5.23 and the remaining overall $\not P_T$ is designated $\not P_T{}^{good}$.

- $\not P_T{}^{high} / \not P_T < 0.8$
  Sparks can potentially cause a very large fake energy. Hence the event is rejected if the $\not P_T$ measured by the calorimeter cell with the highest individual energy ($\not P_T{}^{high}$) is more than 80% of the total $\not P_T$.

- HAC fraction cuts
  The particles emerging from genuine ep collisions in the interaction region must hit the

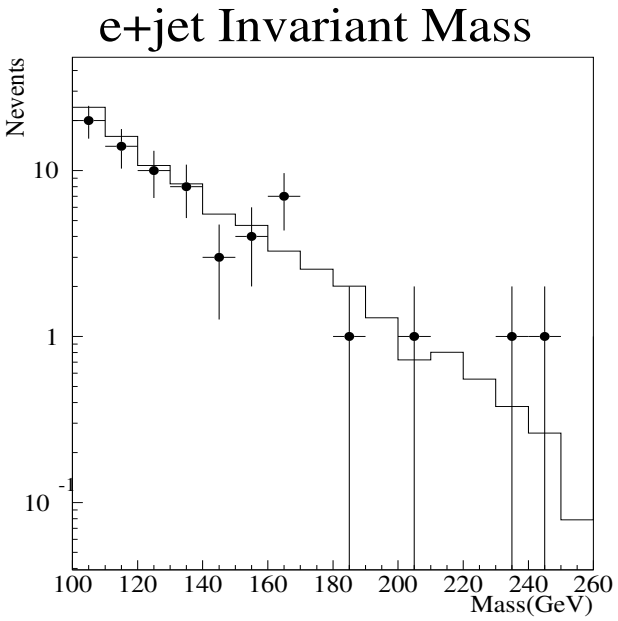

Figure 7.12: *The reconstructed mass distribution for the e* jet *final sample. The points with error bars are the data. The histogram is the total expected background (NC+php). The background histogram is normalized to the data luminosity.*

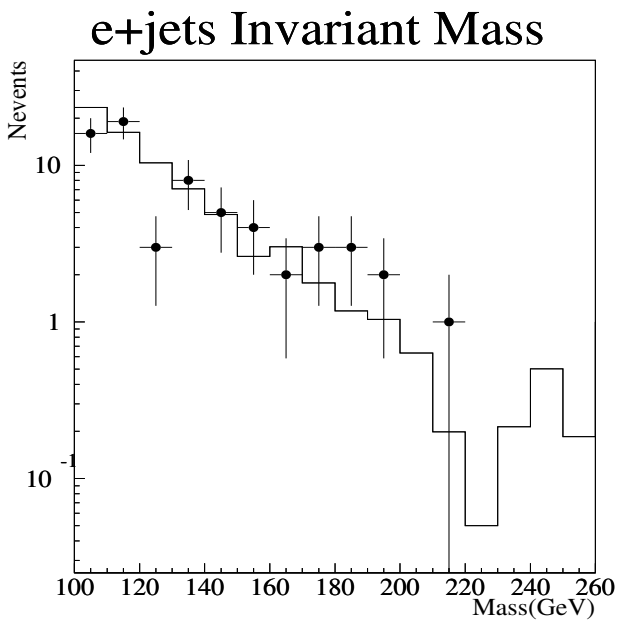

Figure 7.13: *The reconstructed mass distribution for the* e^+ jets *final sample. The points with error bars are the data. The histogram is the total expected background (NC+php). The background histogram is normalized to the data luminosity.*

EMC section before the HAC, so one would not expect these events to be completely hadronic. The following cuts reject cosmic and halo muons which could miss the EMC sections of the CAL.

- $E^{HAC}_{FCAL}/E_{FCAL} < 0.9$ .or. $E_{FCAL} < 5$ GeV
- $E^{HAC}_{BCAL}/E_{BCAL} < 0.9$ .or. $E_{BCAL} < 5$ GeV
- $E^{HAC}_{RCAL}/E_{RCAL} < 0.9$ .or. $E_{RCAL} < 5$ GeV

- $\not\!\!P_T \Delta\Phi(cal - ctd)$
  This variable is defined as the difference between the azimuthal angle of the $\not\!\!P_T$ as measured by the CAL and by the CTD. This requirement further reduces cosmic and halo muon backgrounds.
  - $\not\!\!P_T > 20$ GeV and $\Delta\Phi < 2$ radians
    OR
    $\not\!\!P_T < 20$ GeV and $\Delta\Phi < 1$ radians

- Cosmic and halo muon identification
  Pattern matching algorithms `MUTRIG`[47], `ISITAMU`, `ahalo` and `comcos`[85] are used to further suppress muon related non-ep backgrounds.

- Timing cuts
  Non-ep backgrounds may give a timing measurement which is inconsistent with an ep collision. The cuts performed at the TLT and described in equation 4.10 are repeated and tightened. See appendix A.1 for details.

7.4.2 Selection cuts

Analogous to the preselection performed in the NC-like case, this section outlines the first step in selecting a CC sample with high Q^2. For CC events, well reconstructed events with $\not\!\!P_T$ are preferentially chosen. Tracking and electron/positron finding, in order to remove any NC events, are important in the following event selection:

- DST (34 or 35 or 36) and 37
  Along with the high E_T or high island E_T trigger selections which were common to the NC-like selection, the CC DST bit 34 is also required. Additionally, DST bit 37, which demands a reconstructed or TLT vertex of -60 cm $< Z_{vtx} < 120$ cm, is required.

- Vertex Requirement
  A tracking vertex is required, which must satisfy $|Z_{vtx}| < 50$ cm.

- NC Rejection
  If a scattered $e^{\pm}$ is identified (em probability>0.001) in the calorimeter then the event is classified as a NC background and rejected. See appendix A.2.

- At least one good vertex track (Ngtrk)
  A good vertex track is one fitted to the vertex and has a $P_T > 0.2$ GeV in the angular range of $15° < \theta < 165°$, the CTD acceptance. Demanding a good track reduces non-ep backgrounds.

- Ngtrk > 0.25(Ntrk $- 20$)
  Ngtrk is the number of good vertex tracks, defined above, and Ntrk is the total number of reconstructed tracks. Beam-gas events typically have many tracks but only a few of them are assigned to the primary vertex. This cut effectively removes them. Figure 7.14 shows events in the (number of good tracks)-(number of all tracks) plane, excluding the cut for all final candidates with at least one good jet.

- $\not\!\!P_T(-1ir) > 12$ GeV
  $\not\!\!P_T(-1ir)$ is the net missing transverse momentum calculated from all cells in the calorimeter excluding the first ring of FCAL cells immediately surrounding the beam hole. This $\not\!\!P_T(-1ir)$ distribution is shown in figure 7.15(a), excluding the cut for all final candidates with at least one good jet.

- $\not\!\!P_T > 15$ GeV
  Significant net transverse momentum is the primary signature of a CC-like event. This cut was optimized for the ν jets topologies as a function of the squark mass. The optimal cut is slightly lower at squark masses below 120 GeV. A lower $\not\!\!P_T$ cut increases contamination from background, therefore this global cut was assumed for all masses and topologies. Figure 7.15(b) shows the $\not\!\!P_T$ distribution before applying the cut for all final candidates with at least one good jet. The $\not\!\!P_T$ distribution in figure 7.16 shows good agreement between data and MC background.

These cleaning and selection cuts for the CC DIS sample and their effect on the data sample are summarized in table 7.2.

The ZEUS high Q^2 CC analysis[66] applies all these cuts plus the kinematic cuts $Q^2 > 200$ GeV^2 and $y < 0.9$. By performing these cuts the same sample of events is selected and agreement between the data and MC background is observed, as seen in figures 7.16 and 7.17. This data sample contains 857 events, to be compared with 880.7 events expected from CC DIS and photoproduction backgrounds.

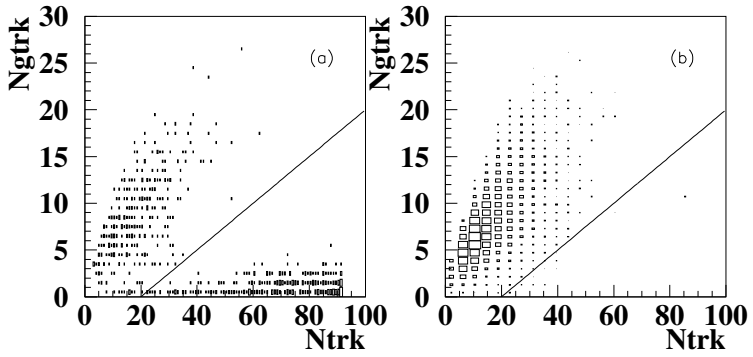

Figure 7.14: *Distributions of events in the (number of good tracks)-(number of all tracks) plane for (a) Data and (b) CC DIS MC simulations.*

Selection Cut	Events Selected	CC Efficiency %
DST Trigger	466028	100
CAL Timing	384922	100
non-ep: halo μ, cosmic μ	384524	99.7
$0.5 < \not\!\!P_T{}^{good} / \not\!\!P_T < 2$	337634	99.6
$\not\!\!P_T{}^{high} / \not\!\!P_T < 0.8$	281805	99.1
HAC fraction	259305	98.3
$\Delta\Phi(cal - ctd)$ match	151582	96.4
$\lvert Z_{vtx} < 50 \rvert$ cm	90911	92.9
NC Cut	89999	92.7
$Ngtrk >= 1$	70449	87.7
$Ngtrk > 0.25(ntrk - 20)$	41607	87.5
$\not\!\!P_T(-1ir) > 12$ GeV	3007	65.1
$\not\!\!P_T > 15$ GeV	1105	61.6

Table 7.2: *Summary of the cleaning and selection cuts for the CC DIS sample. The CC Efficiency is normalized to the DST trigger selection.*

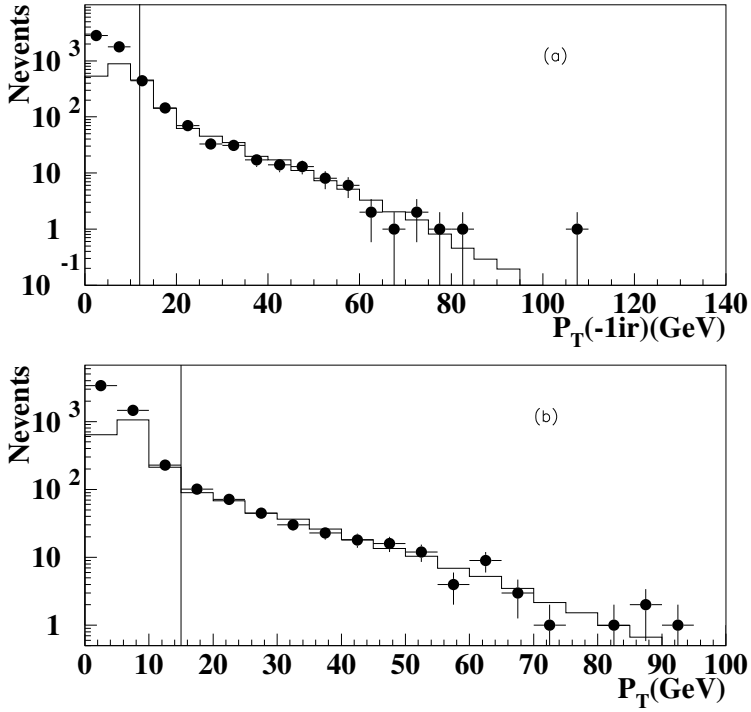

Figure 7.15: *The (a) $\not\!\!P_T(-1ir)$ and (b) $\not\!\!P_T$ distributions before the application of their selection. The points are the data and the histogram is the expectation from MC simulations normalized to the data luminosity. The cuts are indicated by the lines.*

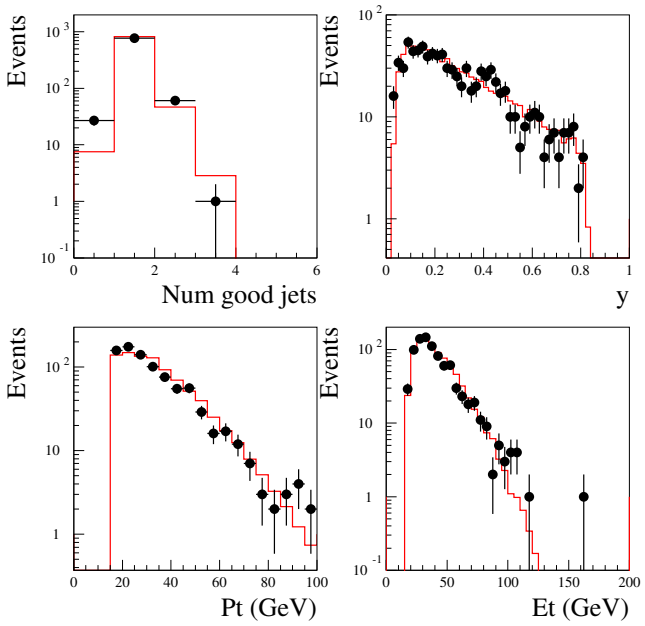

Figure 7.16: *Above: the number of good jets and y distributions after preselection. Below: the $\not\!\!P_T$ and E_T distributions after preselection. The points represent the data and the histogram represents the SM expectation (CC+php) normalized to the data luminosity.*

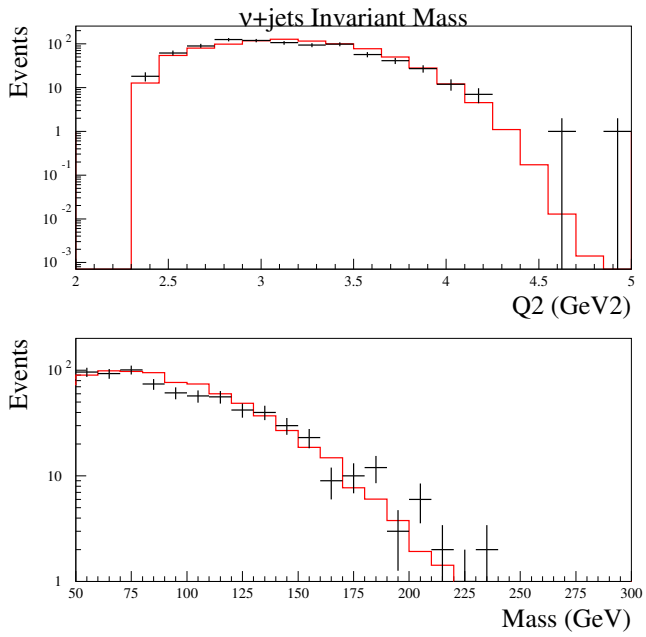

Figure 7.17: *The* $\log_{10}(Q^2)$ *and invariant mass after preselection.*

7.4.3 Signal Enhancement

Once a sample of high Q^2 CC events is isolated, one can take advantage of the high mass, high y, multijet characteristics of the topology that are being investigated. To enhance the acceptance in the high Q^2 CC DIS sample resulting from the cleaning and selection cuts, the following cuts were applied:

- Mass > 100 GeV
  As in the NC-like cases a high invariant mass of the ν jets system, as calculated by equation 5.50, is required.

- $y > 0.4$
  This cut is an effective cut on the $E - P_z$ of the entire event. A high y cut selects multijet events, as they are more likely to be spread out throughout the detector each contributing to a higher $E - P_z$ measurement and hence a higher y.

- Number of good jets ≥ 2
  Again as in the NC-like multijet topologies, squark decays with a ν in the final state are high y events with two or more good jets.

The effects of the cuts are displayed in figure 7.18(a) for the generated SUSY phase space points. Note that the range of efficiencies for the lowest two squark mass bins are noticeably smaller than the range for the corresponding squark masses above 120 GeV. This is the result of two effects. First, the $\not{P}_T$ cut dominates the efficiency at the lowest mass bins. Second, at lower squark masses, fewer topologies exist, as a consequence of the assumption that the LSP is the $\tilde{\chi}_1^0$. Hence, if $M_{\tilde{\chi}_1^0}$, which is determined by the choice of the SUSY parameters, is greater than the squark mass, then that phase space point will only contribute to the efficiencies at squark masses above the mass of the LSP.

Typical values of the efficiency for selecting squarks range from $\sim 35\%$ at $M_{\tilde{q}} < 120$ GeV to $\sim 50\%$ at $M_{\tilde{q}} > 120$ GeV. The mass resolution for cascade squark decays with a neutrino in the final state is roughly constant at 12 GeV as a function of the squark mass (figure 7.18(b)).

There are 35 events remaining after all cuts, in agreement with the SM expectation from MC background as summarized in table 7.3. Figure 7.19 shows the invariant mass spectrum of the selected events compared with the MC prediction. As for NC-like events, there is no evidence of a squark signal, and the data is well described by the SM.

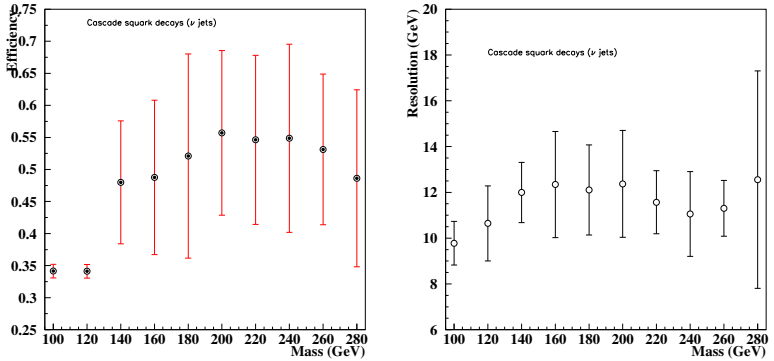

(a) (b)

Figure 7.18: *(a) The efficiencies and (b) resolutions for cascade squark decays into* ν jets *as a function of the squark mass. The range of efficiencies and resolutions over the generated SUSY phase space points at each mass is shown. The mass points below* 140 GeV *are dominated by the the* P_T *cut.*

Reconstructed Channel	N_{obs}	N_{exp}
νjets	35	36 ± 3

Table 7.3: *Summary of the number of events in the CC-like data sample compared to expected background from CC DIS (Ariadne) and php (Herwig Resolved and Direct* $E_T > 50$ *GeV).*

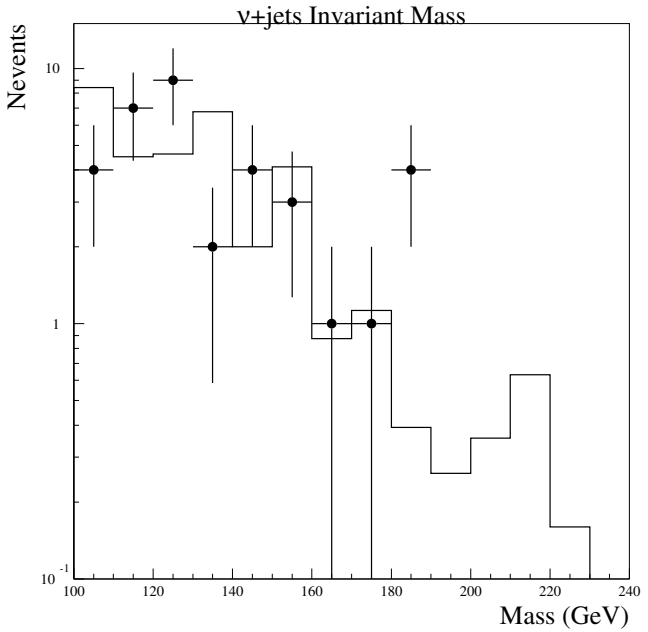

Figure 7.19: *The reconstructed mass distribution for the* ν jets *final sample. The points with error bars are the data. The histogram is the total expected background (NC+php). The background histogram is normalized to the data luminosity.*

Chapter 8

Limit Setting Procedure

For an integrated luminosity, $\mathcal{L}$, the expected differential mass distribution in analysis channel c is the sum of the background, $b_c(M)$, and the signal, $s_c(M;\sigma)$, where the rate of signal events is proportional to the squark production cross section, σ. The probability density in the mass for the events in a mass interval $[M_{low}, M_{high}]$ is given by

$$f_c(M;\sigma) = \frac{s_c(M;\sigma) + b_c(M)}{\int_{M_{low}}^{M_{high}} (s_c(M';\sigma) + b_c(M'))\mathrm{dM}'}. \tag{8.1}$$

The functions $b_c(M)$ were determined by fits to the background Monte Carlo. The total expected background for channel c is defined as $B_c = \int_{M_{low}}^{M_{high}} b_c(M)\mathrm{dM}$. The mass distribution for the signal, $s_c(M;\sigma)$, is taken to be a Gaussian with a root mean square (RMS) width which has been determined by fits to the signal Monte Carlo samples. The mass window $[M_{low}, M_{high}]$ is taken to be a $\pm 3\sigma$ window centered on $M_{\tilde{q}}$. The normalization of $s_c(m;\sigma)$ is given by $\mathcal{L}\epsilon_c\sigma = \int_{M_{low}}^{M_{high}} s_c(M;\sigma)\mathrm{dM}$, where ϵ_c is the probability that a squark will be accepted in channel c with $M_{low} < M < M_{high}$. It is computed as a sum over the decay modes, d, of the product of the branching ratio, β_d, and the cross efficiency, ϵ_c^d, which is the probability for a squark which decays via mode d to be accepted in channel c:

$$\epsilon_c = \sum_{d=1}^{N_{decays}} \beta_d \epsilon_c^d. \tag{8.2}$$

The likelihood to observe N_c^{obs} events in channel c in the mass interval $[M_{low}, M_{high}]$ is written as a product of the Poisson probability to observe N_c^{obs} events and the probability densities for the reconstructed masses M_i of each observed event:

$$L_c(\sigma) = e^{-(\mathcal{L}\epsilon_c\sigma + B_c)} \frac{(\mathcal{L}\epsilon_c\sigma + B_c)^{N_c^{obs}}}{N_c^{obs}!} \prod_{i=1}^{N_c^{obs}} f_c(M_i;\sigma). \tag{8.3}$$

The likelihood for all channels is then given by

$$L(\sigma) = \prod_{c=1}^{N_{chan}} L_c(\sigma). \tag{8.4}$$

The 95% confidence limit (CL) on the cross section is obtained by solving

$$\int_0^{\sigma_{limit}} \mathrm{d}\sigma L(\sigma) = 0.95 \int_0^{\infty} \mathrm{d}\sigma L(\sigma). \tag{8.5}$$

The upper limit on the coupling λ' is calculated using the relation

$$\lambda'_{limit} = \sqrt{\frac{\sigma_{limit}}{\sigma_{NWA}}}\lambda'_{NWA}, \tag{8.6}$$

where σ_{NWA} is the cross section calculated using the narrow width approximation (NWA) and λ'_{NWA} is the coupling used in the calculation of the σ_{NWA}. Since the branching ratios are functions of the coupling λ', the likelihoods are calculated iteratively given an initial guess for λ'.

8.1 Inclusion of systematic uncertainties

A systematic error can in incorporated in the limit procedure by convoluting a Gaussian with the Poisson probability and solving equation 8.5:

$$L(\sigma) \propto \int \frac{\mathrm{d}\gamma}{\sqrt{2\pi}\kappa} \exp\left[\frac{-(\gamma-1)^2}{2\kappa^2}\right] \frac{1}{n!} \exp\left[-\gamma(\mu_s+\mu_b)\right] \gamma^n (\mu_s+\mu_b)^n, \tag{8.7}$$

where $\mu_s = \mathcal{L}\epsilon\sigma$, $\mu_b = B$, $n = N^{obs}$ from equation 8.3 and κ is the fractional systematic uncertainty. The double integration over γ and μ_s (or alternatively σ) is achieved by performing a single integration along the contour which maximizes the integrand in 8.7 with respect to γ for a given μ_s[86]. The values of γ for which this is true at a given μ_s are the roots of the following equation:

$$\gamma^2 + [(\mu_s+\mu_b)\kappa^2 - 1]\gamma - n\kappa^2 = 0. \tag{8.8}$$

8.2 Interpolation and limits in the SUSY phase space

Limits on σ and λ' are derived at points on a grid of the SUSY parameters (μ, M_2) where $-200 < \mu < 200$ (in 20 GeV intervals) and $80 < M_2 < 310$ (in 10 GeV intervals). At each grid point the limits are derived as a function of $M_{\tilde{q}}$ from 100 to 280 GeV in 1 GeV intervals.

The masses of the gauginos are determined by the SUSY parameters. Monte Carlo data sets are generated as described in section 6.2 and not at each point of the limit grid. Eight phase space points were selected such that they encompass the mass space of the $M_{\tilde{\chi}_1^0}, M_{\tilde{\chi}_2^0}$ and $M_{\tilde{\chi}_1^\pm}$. The conjecture is made that the efficiencies, ϵ_c, and the cross efficiencies, ϵ_c^d, depend on the masses of the gauginos. Hence in order to determine the efficiencies at

a phase space point which has not been generated, a weighted linear combination of the generated point efficiencies is calculated. The weights, w_i, are proportional to the square of the difference in gaugino masses between the desired and generated SUSY phase space point such that

$$w_i \quad \alpha \quad 1/(\Delta M^2_{\tilde{\chi}^0_1} + \Delta M^2_{\tilde{\chi}^0_2} + \Delta M^2_{\tilde{\chi}^\pm_1}), \quad \text{and} \quad \Delta M^2 = (M_{\tilde{\chi}i} - M_{\tilde{\chi}})^2. \tag{8.9}$$

The weights are normalized such that $\sum_{i=1}^{N_{psp}} w_i = 1$. Hence, the probability for a squark which decays via mode d to be accepted in channel c given in 8.2 is now written

$$\epsilon_c = \sum_{d=1}^{N_{decays}} \beta_d \sum_{i=1}^{N_{psp}} w_i \epsilon^d_{c,i}. \tag{8.10}$$

8.3 Systematic Uncertainties

The systematic uncertainty considered in the derivation of the upper limit for $\not{R}_p$ squark production is estimated to be 13%. Systematic errors can affect factors in equation 8.3 such as the luminosity, the background distribution or selection efficiency. The following sources of systematic error were considered:

- Luminosity measurement
  The systematic uncertainty on the e^+p data sample collected during the years 1994-1997 is estimated to be 1.6%[87].

- Electron/Positron finding
  An estimate of the `em` finding efficiency is extracted by comparing `em` with the `SINISTRA` neural net electromagnetic cluster finder. The variation between the two $e^\pm$ finders is found to be less than 5%[70].

- Calorimeter Energy scale
  According to studies[88, 89, 90], the absolute energy scale of the calorimeter is unknown to $\pm 3\%$. This translates into a maximum change of 1.7% in the selection efficiency and is included in figure 8.1.

- Vertex
  The vertex requirement was varied by ± 15 cm, which changed the squark selection efficiency by 2% and is included in figure 8.1.

- Selection cuts
  All cuts based on CAL energies, E_e, E_T, $\not{P}_T$, jet E_T, δ and invariant mass were varied

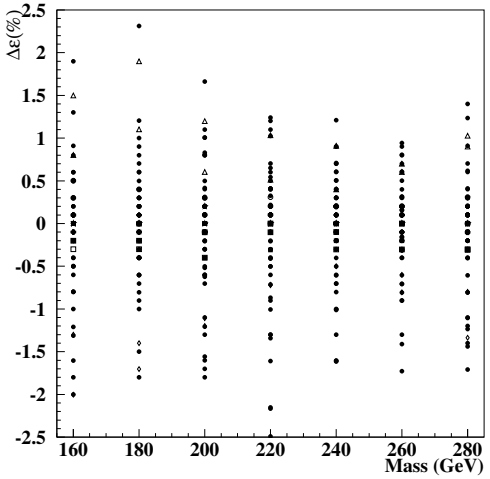

Figure 8.1: *The systematic uncertainty of variation of the selection cuts on the selection efficiency (ϵ). Each marker represents an individual cut variation and is taken to be the worst of any signal MC generated phase space point. There are 32 points at each mass bin corresponding to the positive and negative variation of the vertex and selection cuts (E_e, E_T, $\not{P}_T$, jet E_T, δ and M_{inv}) as well as the calorimeter energy scale for the NC and CC samples.*

Systematic	Uncertainty (%)
Luminosity	1.6
$e^{\pm}$ finding	5
CAL energy scale	2
Vertex	2
Selection Cuts	2
Interpolation	1
Background estimation	6.4
PDF	9.4
TOTAL	13

Table 8.1: *Summary of systematic uncertainties considered.*

by the uncertainty of energy scale (3%) individually. The effect was at most 2% in the signal selection. See figure 8.1.

- Interpolation
  The interpolation of the limits in the SUSY phase space described in section 8.2 was evaluated by using another weight. Instead of the weight ansatz used in equation 8.9 the following was used:

$$w_i \quad \alpha \quad 1/(|\Delta M_{\tilde{\chi}_1^0}| + |\Delta M_{\tilde{\chi}_2^0}| + |\Delta M_{\tilde{\chi}_1^{\pm}}|), \quad \Delta M = (M_{\tilde{\chi}i} - M_{\tilde{\chi}}). \tag{8.11}$$

  The effect on the limit was at most 1%.

- Background estimation
  The effect of an error on the background estimate used in the upper limit is difficult to assess as it depends also on the number of observed events. A simple estimate can be obtained by the difference between two MC background samples. The background MC MEPS was used as an alternative MC. The effect was determined to be 6.4%.

- Theoretical uncertainty.
  The parton density uncertainty should be taken into account. Changing the parton density function (PDF) used in the cross section calculation resulted in an uncertainty of 9.4%.

Table 8.1 summarizes the sources of systematic uncertainty taken into account. The various systematic errors are assumed to be uncorrelated and are added in quadrature to give the total systematic error of 13%.

Chapter 9

Results

The search for $\not{R}_p$ supersymmetric particles was performed using the 47.7 pb^{-1} of e^+p data collected between 1994 to 1997 at a centre of mass energy of 300 GeV. Squarks produced in e^+ quark fusion, via the $\not{R}_p$ coupling λ'_{1j1}, can decay to e-quark or gaugino-quark via a supersymmetric gauge decay, resulting in a final state with multiple jets and a lepton that could be a positron, electron or neutrino.

There was agreement between the data and the expectation from the SM backgrounds considered in all the reconstructed channels. The signal efficiency for any topology or SUSY phase space point ranges from $\sim 30\% - 60\%$. In the absence of any signal, limits are set on the $\not{R}_p$ coupling λ'_{1j1} as a function of the squark mass and the SUSY parameters $(M_2, \mu, \tan\beta)$. A systematic error of 13% was included in the determination of the limit as outlined in section 8.1.

9.1 Limits

Given a squark mass one can derive an upper limit on the coupling λ'_{1j1}. To obtain these limits one combines the different squark decay channels. Therefore, it is necessary to know the branching ratios for each channel. These depend on the mass of the squark, the coupling λ'_{ijk} and also on the SUSY parameters. Recall that the phenomenology depends on the nature of the LSP. The possible channels are the same whether the LSP is $\tilde{\gamma}$ dominated or $\tilde{Z}$ dominated, but the branching ratios are nevertheless different.

The search was performed at points on a grid in $(M_2, \mu, M_{\tilde{q}})$ in the region $80 \leq M_2 \leq 310$ GeV, $-200 \leq \mu \leq 200$ GeV and $100 \leq M_{\tilde{q}} \leq 280$ GeV. The grid spacings were 10 GeV, 20 GeV and 1 GeV for M_2, μ and $M_{\tilde{q}}$ respectively. Two values of $\tan\beta$ were considered, 2 and 10. Limits were only calculated at points where the LSP is the $\tilde{\chi}_1^0$ with a mass exceeding 40 GeV.

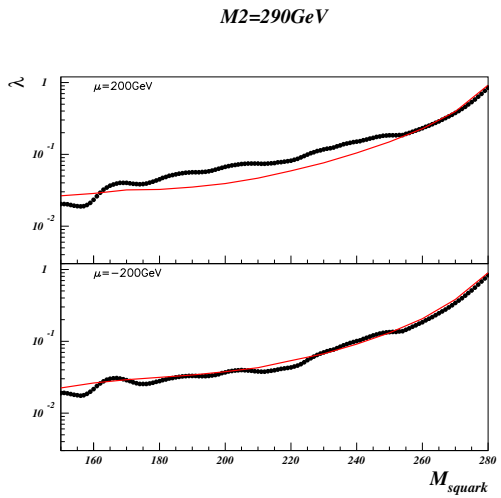

Figure 9.1: λ'_{1j1} *limits as a function of* $M_{\tilde{q}}$ *for fixed* $M_2 = 290$ GeV, $\mu = -200, 200$ GeV *and* $\tan\beta = 2$. *The thick curve represents the actual limit and the thin curve indicates the expected limit.*

The expected limits follow the actual 95% CL limits as seen in figure 9.1, which is another indication that there is no significant excess of data over the MC expectation in the range of masses concerned.

The limits do not vary greatly over the SUSY phase space. However, the limits are somewhat better when the $\tilde{\chi}_1^0$ is heavier (figure 9.2). Recall from figure 3.3 that $M_{\tilde{\chi}_1^0}$ scales with M_2.

One other point to note is that the branching ratio to e^+ jets is larger than to e^- jets because the $\tilde{\chi}_1^+$ can only decay into an e^+. Appendix B shows the branching ratios and efficiency curves for various phase space points.

The limits at large squark mass tend to converge to the same limit as illustrated by figure 9.3. This explains that at large mass we are not sensitive and set large upper limits on λ'_{1j1}. At large couplings, the cross section for $eq \to \tilde{q} \to eq$, is not dependent on the gaugino masses and hence the SUSY phase space.

No strong variation in the limits with M_2, μ, and $\tan\beta = 2, 10$ was observed. The 95% CL upper limits on the coupling λ'_{1j1} ranged from 0.01 for squark masses of 100 GeV to

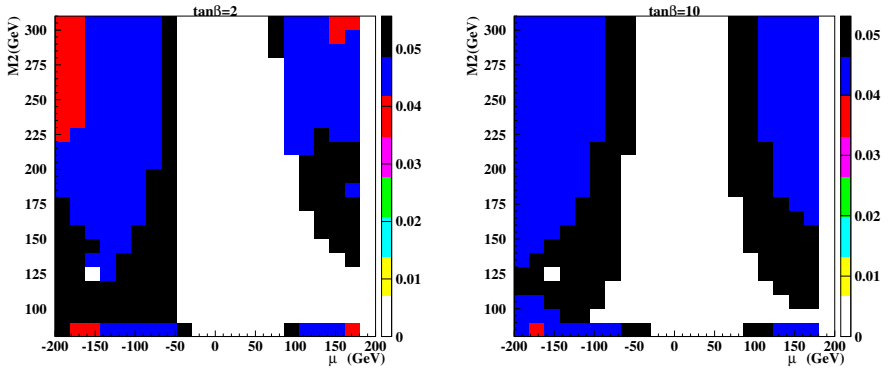

(a) (b)

Figure 9.2: *The 95% CL upper limit on* λ'_{1j1} *in the SUSY parameter* (M_2, μ) *space for* $M_{\tilde{q}} = 200$ GeV. *(a)* $\tan\beta = 2$. *(b)* $\tan\beta = 10$. *The scale on the range indicates the value of* λ'_{1j1}. *Recall that the mass* $\tilde{\chi}_1^0$*increases with increasing* M_2. *A limit was not set in the central white region. A region of phase space where the LSP is the lightest chargino.*

about 0.8 for squark masses of 280 GeV. If we select a $\lambda'_{1j1} = 0.3$ then we can rule out squarks below a mass of $254 - 262$ GeV depending on position in the SUSY phase space (figure 9.3).

9.2 Other experiments

While other HEP experiments have performed SUSY particle searches, HERA remains one of the most competitive with respect to the λ'_{ijk} $\not{R}_p$ coupling.

Extensive MSSM searches with R-parity conservation have been performed at HERA, LEP and the Tevatron, all of which resulted in the absense of a signal. Within ZEUS, a search for selectron-squark production via the diagram given in figure 9.4 was performed at ZEUS. That analysis excluded $(m_{\tilde{e}} + m_{\tilde{q}})/2 < 77$ GeV at 95% CL for $m_{\tilde{\chi}_1^0} = 40$ GeV and large MSSM parameter $|\mu|$ values[91]. However, these results, as with any other MSSM search with strict R-parity conservation, do not apply to the results presented in this thesis.

Both ZEUS[92] and H1[93] have performed lepton flavour violation searches, $eq \to \mu q, \tau q$. These searches whose results can be interpreted in terms of $\not{R}_p$ couplings λ'_{2jk} and λ'_{3jk} and limits are generally set on the product of the two couplings. These couplings do not fall into

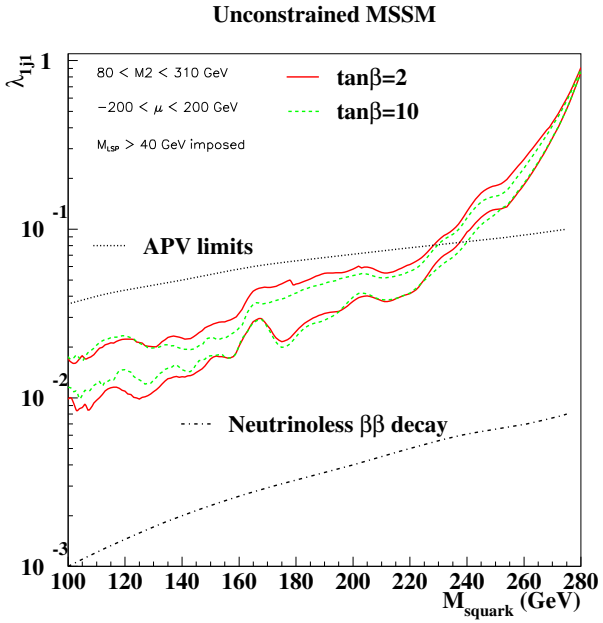

Figure 9.3: 95% *CL exclusion upper limits on the* $\not{R}_p$ *coupling* λ'_{ijk} *as a function of the squark mass. For each squark mass, a scan of the SUSY parameter space* (M_2, μ) *has been performed with the maximum (minimum) value of the coupling limit represented by the upper (lower) curves. The solid (dashed) line indicates the phase space scan with* $\tan\beta = 2$ (10). *Also plotted are the limits on* λ'_{111} *from neutrinoless* $\beta\beta$ *decay experiments and the limits on* λ'_{1j1} *from Atomic Parity Violation experiments. Regions above the curves are excluded.*

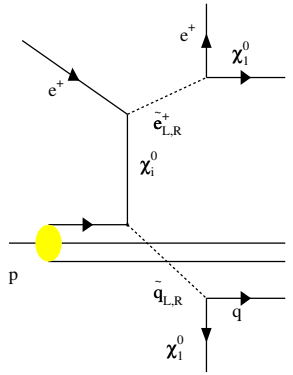

Figure 9.4: *Diagram for the selection squark production process at HERA.*

the scope of topologies covered in this thesis.

The LEP experiments influenced the consideration to set limits only where the $M_{\tilde{\chi}^0_1} > 40$ GeV due to their constraints on the SUSY parameter space in their gaugino searches[94].

The result obtained by this analysis is compared to the most stringent indirect limits in figure 9.3. The production of a $\tilde{u}$ squark via a λ'_{111} coupling is severely constrained by the non-observation of neutrinoless double beta decay[95]. Atomic Parity Violation[96] (APV) experiments set limits on $\tilde{c}$ (as well as $\tilde{t}$) but are only better than the ZEUS limits at the very high masses. Otherwise HERA provides the best limits on λ'_{1j1}, where $j = 2, 3$. The D0[97] and CDF[98] experiments at the Tevatron have performed searches for scalar leptoquarks which effectively rule out $\tilde{u}^i_L$ squark masses below 205 GeV as long as the branching ratio $\tilde{u}^i_L \to e^+q$ is greater than 50%. Since this $\not{R}_p$ branching ratio can be quite small, these constraints become weaker as the branching ratio via direct $\not{R}_p$ decreases.

The only true competitor for the ZEUS results come from the other collider experiment at HERA, H1. The H1 analysis[99] has roughly the same sensitivity and efficiency as this analysis and hence their results are comparable to those from this analysis.

All the searches discussed above have proven to be a further confirmation of the SM. Yet SUSY remains to be the favoured theory for physics beyond the SM by theorists. The difficulty in presenting limits from SUSY searches is that SUSY has a multidimensional phasespace but results can only be presented in at most three dimensions. The results given in figure 9.3 show the two variables, λ'_{1j1} and squark mass, which HERA can set the most stringent limits.

Chapter 10

Conclusion

A search for R-parity violating supersymmetric particles has been performed using 47.7 pb^{-1} of e^+p data taken using the ZEUS detector at HERA from 1994 to 1997. No evidence was discovered for squarks, which are produced via an $\not{R}_p$ coupling λ'_{1j1}, decaying into e jet, e jets or ν jets. Upper limits at 95% CL on the coupling λ'_{1j1} as a function of the squark mass from $100 - 280$ GeV are derived, for points in the SUSY parameter space $(M_2, \mu, \tan\beta)$. This analysis constitutes the first such search for ZEUS.

The limits were found not to vary greatly over the SUSY parameter space and typically range from 0.01 at a squark mass of 100 GeV to 0.8 at 280 GeV. At a fixed squark mass an upper limit on the coupling strength can be extracted or conversely at a given coupling strength, one can exclude squark masses below a certain limit, inferred from figure 9.3. For example, at a coupling strength on the order of the electromagnetic scale, $\lambda'_{1j1} = 0.3$, squarks below 254 GeV are excluded over the entire SUSY parameter space considered.

The invariant mass distributions in figures 7.12, 7.13 and 7.19 show that the SM explains the specific high mass multijet topologies considered in the context of this thesis.

HERA has a unique ability to directly search for couplings $L_iQ_j\bar{D}_k$ due to the lepton and quark flavours in the initial state. In 1998 and 1999, HERA operated with e^- rather than e^+. The analysis here forms a template for the search to be made in this data set, which opens up HERA's sensitivity to $\tilde{d}^j_R$ squark production. Moreover, the proton beam energy was increased in 1998 to 920 GeV, corresponding to the larger centre of mass energy of 318 GeV. Since the $\not{R}_p$ squarks are produced via the s-channel right up to the kinematical limit, the new data set will increase the mass reach of this search. The HERA facility was being upgraded to increase luminosity at the time this thesis was being written. With a five-fold increase in HERA's luminosity expected for the post lumi-upgrade of the machine, the potential for discovery will be much greater.

Appendix A

CC-like Cleaning Cuts

A.1 Calorimeter Timing cuts

The following timing cuts were applied to be consistent with ep collisions:

$$|t_{FCAL}| < 6 \text{ ns.or.} N_{FCAL} < 2 \text{.or.} E_{FCAL} < 0.6 \text{ GeV}$$
$$|t_{FCAL}| < 5 \text{ ns.or.} N_{FCAL} < 2 \text{.or.} E_{FCAL} < 10 \text{ GeV}$$
$$|t_{BCAL}| < 6 \text{ ns.or.} N_{BCAL} < 2 \text{.or.} E_{BCAL} < 0.6 \text{ GeV}$$
$$|t_{BCAL}| < 5 \text{ ns.or.} N_{BCAL} < 2 \text{.or.} E_{BCAL} < 10 \text{ GeV}$$
$$|t_{FCAL}| < 6 \text{ ns.or.} N_{FCAL} < 2 \text{.or.} E_{RCAL} < 0.6 \text{ GeV}$$
$$|t_{RCAL}| < 5 \text{ ns.or.} N_{RCAL} < 2 \text{.or.} E_{RCAL} < 10 \text{ GeV}$$
$$|t_{global}| < 6 \text{ ns.or.} N_{global} < 2 \text{.or.} E_{global} < 2 \text{ GeV}$$
$$|t_{global}| < 5 \text{ ns.or.} N_{global} < 2 \text{.or.} E_{global} < 10 \text{ GeV}$$
$$|t^{up}_{BCAL}| < 6 \text{ ns.or.} N^{up}_{BCAL} < 2 \text{.or.} E^{up}_{BCAL} < 10 \text{ GeV}$$
$$|t^{down}_{BCAL}| < 6 \text{ ns.or.} N^{down}_{BCAL} < 2 \text{.or.} E^{down}_{BCAL} < 10 \text{ GeV}$$

$|t_{FCAL} - t_{RCAL}| < 6$ ns.or.$|\min(N_{FCAL}, N_{RCAL}) < 2$.or.$\min(E_{FCAL}, E_{RCAL}) < 1$ GeV

$|t^{up}_{BCAL} - t^{down}_{BCAL}| < 6$ ns.or.$|\min(N^{up}_{BCAL}, N^{down}_{BCAL}) < 2$.or.$|\min(E^{up}_{BCAL}, E^{down}_{BCAL}) < 1$ GeV

N_X is the number of PMTs which are used in the time measurement for the region X.

A.2 NC positron/electron criteria

The candidate DIS $e^{\pm}$ had to satisfy the standard NC DIS $e^{\pm}$ criteria [100] with an energy greater then 4 GeV and $\delta > 30$ GeV. Other cuts were as follows:

- $E^e_{iso} < 5$ GeV
  The candidate had to be well isolated. The energy not assigned to the electromagnetic cluster within a cone of $R = 0.8$ in (η, ϕ)-space centred around the $e^{\pm}$ had to be less than 5 GeV.

- $\theta^e < 15^\circ \rightarrow E^e_T > 20$ GeV
  If found in the FCAL a large electron E_T is required.

- $15^\circ < \theta^e < 164^\circ \rightarrow P^e_{trk}/E^e > 0.25$
  If found within the CTD acceptance, a matching track (with a DCA of 8 cm) is required with the momentum as measured by the CTD (P^e_{trk}) to be consistent with the energy measured by the CAL.

- $\theta^e > 164^\circ \rightarrow E^e_T > 2$ Gev
  RCAL candidates are required to have a minimum E_T.

Appendix B

Branching Ratios and Signal Efficiencies

The branching ratios and signal efficiencies, for all the squark decays considered, are presented here for a few representative phase space points. The branching ratios and efficiencies are plotted as a function of the squark mass and are evaluated at the λ'_{1j1} limit for that squark mass and phase space point.

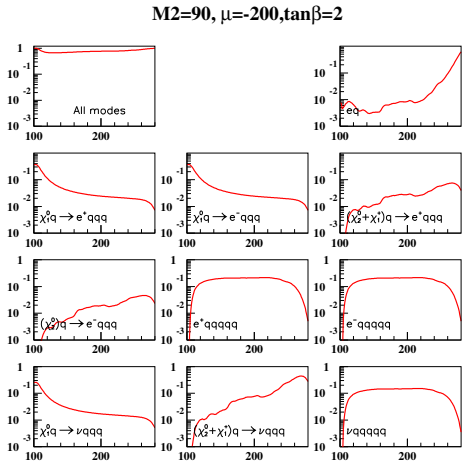

Figure B.1: *Branching ratios as a function of squark mass in* GeV.

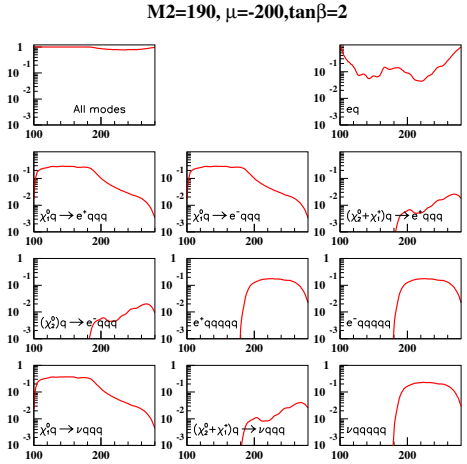

Figure B.2: *Branching ratios as a function of squark mass in* GeV.

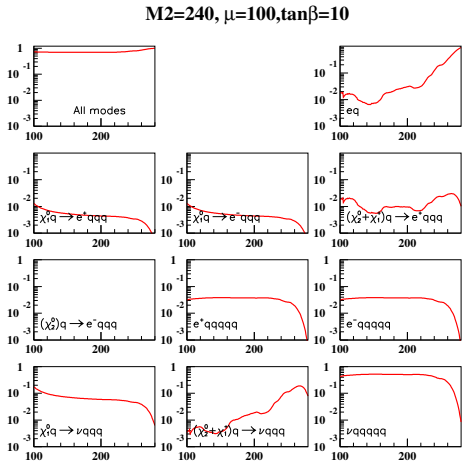

Figure B.3: *Branching ratios as a function of squark mass in* GeV.

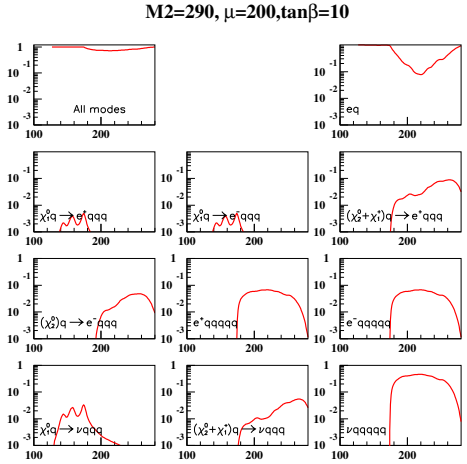

Figure B.4: *Branching ratios as a function of squark mass in* GeV.

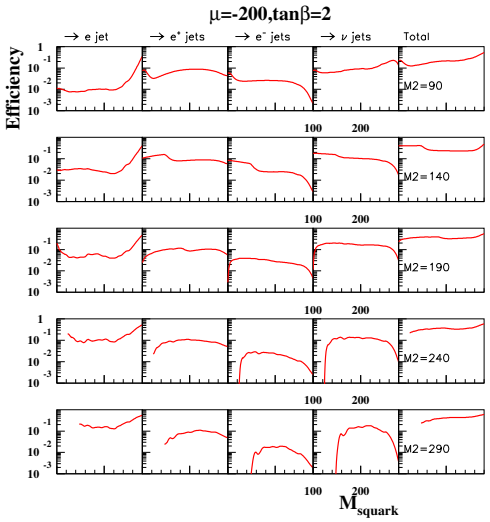

Figure B.5: *Efficiency as a function of squark mass in* GeV.

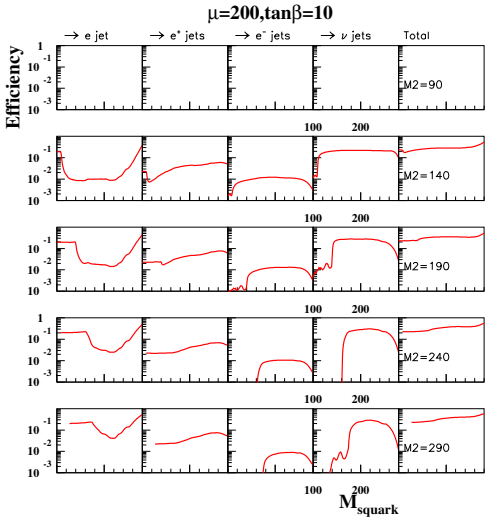

Figure B.6: *Efficiency as a function of squark mass in* GeV.

Appendix C

The ZEUS Collaboration

J. Breitweg, S. Chekanov, M. Derrick, D. Krakauer, S. Magill, B. Musgrave, A. Pellegrino, J. Repond, R. Stanek, R. Yoshida
Argonne National Laboratory, Argonne, IL, USA [p]

M.C.K. Mattingly
Andrews University, Berrien Springs, MI, USA

P. Antonioli, G. Bari, M. Basile, L. Bellagamba, D. Boscherini[1], A. Bruni, G. Bruni, G. Cara Romeo, L. Cifarelli[2], F. Cindolo, A. Contin, M. Corradi, S. De Pasquale, P. Giusti, G. Iacobucci, G. Levi, A. Margotti, T. Massam, R. Nania, F. Palmonari, A. Pesci, G. Sartorelli, A. Zichichi
University and INFN Bologna, Bologna, Italy [f]

C. Amelung[3], A. Bornheim[4], I. Brock, K. Coböken[5], J. Crittenden, R. Deffner[6], H. Hartmann, K. Heinloth[7], E. Hilger, P. Irrgang, H.-P. Jakob, A. Kappes[8], U.F. Katz, R. Kerger, E. Paul, J. Rautenberg,
H. Schnurbusch, A. Stifutkin, J. Tandler, K.C. Voss, A. Weber, H. Wieber
Physikalisches Institut der Universität Bonn, Bonn, Germany [c]

D.S. Bailey, O. Barret, N.H. Brook[9], B. Foster[1], G.P. Heath, H.F. Heath, E. Rodrigues[10], J. Scott, R.J. Tapper
H.H. Wills Physics Laboratory, University of Bristol, Bristol, U.K. [o]

M. Capua, A. Mastroberardino, M. Schioppa, G. Susinno
Calabria University, Physics Dept.and INFN, Cosenza, Italy [f]

H.Y. Jeoung, J.Y. Kim, J.H. Lee, I.T. Lim, K.J. Ma, M.Y. Pac[11]
Chonnam National University, Kwangju, Korea [h]

A. Caldwell, W. Liu, X. Liu, B. Mellado, S. Paganis, S. Sampson, W.B. Schmidke, F. Sciulli
Columbia University, Nevis Labs., Irvington on Hudson, N.Y., USA [q]

J. Chwastowski, A. Eskreys, J. Figiel, K. Klimek, K. Olkiewicz, K. Piotrzkowski[3], M.B. Przybycień, P. Stopa, L. Zawiejski
Inst. of Nuclear Physics, Cracow, Poland [j]

B. Bednarek, K. Jeleń, D. Kisielewska, A.M. Kowal, T. Kowalski, M. Przybycień, E. Rulikowska-Zarębska, L. Suszycki, D. Szuba
Faculty of Physics and Nuclear Techniques, Academy of Mining and Metallurgy, Cracow, Poland [j]

A. Kotański
Jagellonian Univ., Dept. of Physics, Cracow, Poland [k]

L.A.T. Bauerdick, U. Behrens, J.K. Bienlein, K. Borras, V. Chiochia, D. Dannheim, K. Desler, G. Drews, A. Fox-Murphy, U. Fricke, F. Goebel, S. Goers, P. Göttlicher, R. Graciani, T. Haas, W. Hain, G.F. Hartner, D. Hasell[12], K. Hebbel, S. Hillert, M. Kasemann[13], W. Koch[14], U. Kötz, H. Kowalski, H. Labes, L. Lindemann[15], B. Löhr, R. Mankel, J. Martens, M. Martínez, M. Milite, M. Moritz, D. Notz, M.C. Petrucci, A. Polini, M. Rohde[7], A.A. Savin, U. Schneekloth, F. Selonke, M. Sievers[16], S. Stonjek, G. Wolf, U. Wollmer, C. Youngman, W. Zeuner
Deutsches Elektronen-Synchrotron DESY, Hamburg, Germany

C. Coldewey, A. Lopez-Duran Viani, A. Meyer, S. Schlenstedt, P.B. Straub
DESY Zeuthen, Zeuthen, Germany

G. Barbagli, E. Gallo, A. Parenti, P. G. Pelfer
University and INFN, Florence, Italy [f]

A. Bamberger, A. Benen, N. Coppola, S. Eisenhardt[17], P. Markun, H. Raach, S. Wölfle
Fakultät für Physik der Universität Freiburg i.Br., Freiburg i.Br., Germany [c]

P.J. Bussey, M. Bell, A.T. Doyle, C. Glasman[18], S.W. Lee, A. Lupi, N. Macdonald, G.J. McCance, D.H. Saxon,
L.E. Sinclair, I.O. Skillicorn, R. Waugh
Dept. of Physics and Astronomy, University of Glasgow, Glasgow, U.K. [o]

I. Bohnet, N. Gendner, U. Holm, A. Meyer-Larsen, H. Salehi, K. Wick
Hamburg University, I. Institute of Exp. Physics, Hamburg, Germany [c]

T. Carli, A. Garfagnini, I. Gialas[19], L.K. Gladilin[20], D. Kçira[21], R. Klanner, E. Lohrmann
Hamburg University, II. Institute of Exp. Physics, Hamburg, Germany [c]

R. Gonçalo[10], K.R. Long, D.B. Miller, A.D. Tapper, R. Walker
Imperial College London, High Energy Nuclear Physics Group, London, U.K. [o]

U. Mallik
University of Iowa, Physics and Astronomy Dept., Iowa City, USA [p]

P. Cloth, D. Filges
Forschungszentrum Jülich, Institut für Kernphysik, Jülich, Germany

T. Ishii, M. Kuze, K. Nagano, K. Tokushuku[22], S. Yamada, Y. Yamazaki
Institute of Particle and Nuclear Studies, KEK, Tsukuba, Japan [g]

S.H. Ahn, S.B. Lee, S.K. Park
Korea University, Seoul, Korea [h]

H. Lim, I.H. Park, D. Son
Kyungpook National University, Taegu, Korea [h]

F. Barreiro, G. García, O. González, L. Labarga, J. del Peso, I. Redondo[23], J. Terrón, M. Vázquez
Univer. Autónoma Madrid, Depto de Física Teórica, Madrid, Spain [n]

M. Barbi, F. Corriveau, D.S. Hanna, A. Ochs, S. Padhi, D.G. Stairs, M. Wing
McGill University, Dept. of Physics, Montréal, Québec, Canada [a], [b]

T. Tsurugai
Meiji Gakuin University, Faculty of General Education, Yokohama, Japan

A. Antonov, V. Bashkirov[24], M. Danilov, B.A. Dolgoshein, D. Gladkov, V. Sosnovtsev, S. Suchkov
Moscow Engineering Physics Institute, Moscow, Russia [l]

R.K. Dementiev, P.F. Ermolov, Yu.A. Golubkov, I.I. Katkov, L.A. Khein, N.A. Korotkova, I.A. Korzhavina, V.A. Kuzmin, O.Yu. Lukina, A.S. Proskuryakov, L.M. Shcheglova, A.N. Solomin, N.N. Vlasov, S.A. Zotkin
Moscow State University, Institute of Nuclear Physics, Moscow, Russia [m]

C. Bokel, M. Botje, N. Brümmer, J. Engelen, S. Grijpink, E. Koffeman, P. Kooijman, S. Schagen, A. van Sighem, E. Tassi, H. Tiecke, N. Tuning, J.J. Velthuis, J. Vossebeld, L. Wiggers, E. de Wolf
NIKHEF and University of Amsterdam, Amsterdam, Netherlands [i]

B. Bylsma, L.S. Durkin, J. Gilmore, C.M. Ginsburg, C.L. Kim, T.Y. Ling
Ohio State University, Physics Department, Columbus, Ohio, USA [p]

S. Boogert, A.M. Cooper-Sarkar, R.C.E. Devenish, J. Große-Knetter[25], T. Matsushita, O. Ruske,
M.R. Sutton, R. Walczak
Department of Physics, University of Oxford, Oxford U.K. [o]

A. Bertolin, R. Brugnera, R. Carlin, F. Dal Corso, U. Dosselli, S. Dusini, S. Limentani, M. Morandin, M. Posocco, L. Stanco, R. Stroili, M. Turcato, C. Voci
Dipartimento di Fisica dell' Università and INFN, Padova, Italy [f]

L. Adamczyk[26], L. Iannotti[26], B.Y. Oh, J.R. Okrasiński, P.R.B. Saull[26], W.S. Toothacker[14] †, J.J. Whitmore
Pennsylvania State University, Dept. of Physics, University Park, PA, USA [q]

Y. Iga
Polytechnic University, Sagamihara, Japan [g]

G. D'Agostini, G. Marini, A. Nigro
Dipartimento di Fisica, Univ. 'La Sapienza' and INFN, Rome, Italy [f]

C. Cormack, J.C. Hart, N.A. McCubbin, T.P. Shah
Rutherford Appleton Laboratory, Chilton, Didcot, Oxon, U.K. [o]

D. Epperson, C. Heusch, H.F.-W. Sadrozinski, A. Seiden, R. Wichmann, D.C. Williams
University of California, Santa Cruz, CA, USA [p]

N. Pavel
Fachbereich Physik der Universität-Gesamthochschule Siegen, Germany [c]

H. Abramowicz[27], S. Dagan[28], S. Kananov[28], A. Kreisel, A. Levy[28]
Raymond and Beverly Sackler Faculty of Exact Sciences, School of Physics, Tel-Aviv University, Tel-Aviv, Israel [e]

T. Abe, T. Fusayasu, K. Umemori, T. Yamashita
Department of Physics, University of Tokyo, Tokyo, Japan [g]

R. Hamatsu, T. Hirose, M. Inuzuka, S. Kitamura[29], T. Nishimura
Tokyo Metropolitan University, Dept. of Physics, Tokyo, Japan [g]

M. Arneodo[30], N. Cartiglia, R. Cirio, M. Costa, M.I. Ferrero, S. Maselli, V. Monaco, C. Peroni, M. Ruspa, R. Sacchi, A. Solano, A. Staiano
Università di Torino, Dipartimento di Fisica Sperimentale and INFN, Torino, Italy [f]

D.C. Bailey, C.-P. Fagerstroem, R. Galea, T. Koop, G.M. Levman, J.F. Martin, A. Mirea, R.S. Orr, S. Polenz, A. Sabetfakhri, D. Simmons
University of Toronto, Dept. of Physics, Toronto, Ont., Canada [a]

J.M. Butterworth, C.D. Catterall, M.E. Hayes, E.A. Heaphy, T.W. Jones, J.B. Lane, B.J. West
University College London, Physics and Astronomy Dept., London, U.K. [o]

J. Ciborowski, R. Ciesielski, G. Grzelak, R.J. Nowak, J.M. Pawlak, R. Pawlak, B. Smalska, T. Tymieniecka, A.K. Wróblewski, J.A. Zakrzewski, A.F. Żarnecki
Warsaw University, Institute of Experimental Physics, Warsaw, Poland [j]

M. Adamus, T. Gadaj
Institute for Nuclear Studies, Warsaw, Poland [j]

O. Deppe, Y. Eisenberg, D. Hochman, U. Karshon[28]
Weizmann Institute, Department of Particle Physics, Rehovot, Israel [d]

W.F. Badgett, D. Chapin, R. Cross, C. Foudas, S. Mattingly, D.D. Reeder, W.H. Smith, A. Vaiciulis[31], T. Wildschek, M. Wodarczyk
University of Wisconsin, Dept. of Physics, Madison, WI, USA [p]

A. Deshpande, S. Dhawan, V.W. Hughes
Yale University, Department of Physics, New Haven, CT, USA [p]

S. Bhadra, C. Catterall, J.E. Cole, W.R. Frisken, R. Hall-Wilton, M. Khakzad, S. Menary
York University, Dept. of Physics, Toronto, Ont., Canada [a]

[1] now visiting scientist at DESY
[2] now at Univ. of Salerno and INFN Napoli, Italy
[3] now at CERN
[4] now at CalTech, USA
[5] now at Sparkasse Bonn, Germany
[6] now at Siemens ICN, Berlin, Germanny
[7] retired
[8] supported by the GIF, contract I-523-13.7/97
[9] PPARC Advanced fellow
[10] supported by the Portuguese Foundation for Science and Technology
[11] now at Dongshin University, Naju, Korea
[12] now at Massachusetts Institute of Technology, Cambridge, MA, USA
[13] now at Fermilab, Batavia, IL, USA
[14] deceased
[15] now at SAP A.G., Walldorf, Germany
[16] now at Netlife AG, Hamburg, Germany
[17] now at University of Edinburgh, Edinburgh, U.K.
[18] supported by an EC fellowship number ERBFMBICT 972523
[19] visitor of Univ. of Crete, Greece, partially supported by DAAD, Bonn - Kz. A/98/16764
[20] on leave from MSU, supported by the GIF, contract I-0444-176.07/95
[21] supported by DAAD, Bonn - Kz. A/98/12712
[22] also at University of Tokyo
[23] supported by the Comunidad Autonoma de Madrid
[24] now at Loma Linda University, Loma Linda, CA, USA
[25] supported by the Feodor Lynen Program of the Alexander von Humboldt foundation
[26] partly supported by Tel Aviv University
[27] an Alexander von Humboldt Fellow at University of Hamburg
[28] supported by a MINERVA Fellowship
[29] present address: Tokyo Metropolitan University of Health Sciences, Tokyo 116-8551, Japan
[30] now also at Università del Piemonte Orientale, I-28100 Novara, Italy
[31] now at University of Rochester, Rochester, NY, USA

[a] supported by the Natural Sciences and Engineering Research Council of Canada (NSERC)
[b] supported by the FCAR of Québec, Canada
[c] supported by the German Federal Ministry for Education and Science, Research and Technology (BMBF), under contract numbers 057BN19P, 057FR19P, 057HH19P, 057HH29P, 057SI75I
[d] supported by the MINERVA Gesellschaft für Forschung GmbH, the German Israeli Foundation, the Israel Science Foundation, the U.S.-Israel Binational Science Foundation, the Israel Ministry of Science and the Benozyio Center for High Energy Physics
[e] supported by the German-Israeli Foundation, the Israel Science Foundation, the U.S.-Israel Binational Science Foundation, and by the Israel Ministry of Science
[f] supported by the Italian National Institute for Nuclear Physics (INFN)
[g] supported by the Japanese Ministry of Education, Science and Culture (the Monbusho) and its grants for Scientific Research
[h] supported by the Korean Ministry of Education and Korea Science and Engineering Foundation
[i] supported by the Netherlands Foundation for Research on Matter (FOM)
[j] supported by the Polish State Committee for Scientific Research, grant No. 112/E-356/SPUB/DESY/P03/DZ 3/99, 620/E-77/SPUB/DESY/P-03/ DZ 1/99, 2P03B03216, 2P03B04616, 2P03B03517, and by the German Federal Ministry of Education and Science, Research and Technology (BMBF)
[k] supported by the Polish State Committee for Scientific Research (grant No. 2P03B08614 and 2P03B06116)
[l] partially supported by the German Federal Ministry for Education and Science, Research and Technology (BMBF)
[m] supported by the Fund for Fundamental Research of Russian Ministry for Science and Education and by the German Federal Ministry for Education and Science, Research and Technology (BMBF)
[n] supported by the Spanish Ministry of Education and Science through funds provided by CICYT
[o] supported by the Particle Physics and Astronomy Research Council
[p] supported by the US Department of Energy
[q] supported by the US National Science Foundation

Appendix D

Glossary

BAC : Backing Calorimeter.

BCAL : Barrel Calorimeter.

BMUON : Barrel Muon chambers.

CAL : Calorimeter.

CC : Charged Current.

CTD : Central Tracking Detector.

DAQ : Data Acquisition System.

DESY : Deutsches Elektronen Synchrotron, the German national high energy physics laboratory located in Hamburg, Germany.

DIS : Deep Inelastic Scattering.

DST : Data Summary Tape.

EMC : Electromagnetic section of the CAL.

EVB : Event Builder.

FCAL : Forward Calorimeter.

FDET : The combination of the FTD and TRD.

FMUON : Forward Muon chambers.

FTD : Forward Tracking Detector.

GFLT : Global First Level Trigger.

GSLT : Global Second Level Trigger.

HAC : Hadronic section of the CAL.

HERA : Hadron Elektron Ring Anlage.

LHC : Large Hadron Collider.

LSP : Lightest Supersymmetric Particle.

LUMIE : Part of the luminosity monitor for measuring Electrons from the Bethe-Heitler process.

LUMIG : Part of the luminosity monitor for measuring Gammas from the Bethe-Heitler process.

M_{Planck}**:** The Planck Scale. If distance scales become short enough (of atomic dimensions or smaller), the theory of quantum mechanics must be used. Therefore, as one extrapolates back in time to the beginning of the Universe, eventually one would reach a state of sufficient temperature and density that a fully quantum mechanical theory of gravitation would be required. This is called the Planck era, and the corresponding scales of distance, energy, and time are called the Planck scale.

MC : Monte Carlo.

MOZART : Monte Carlo for ZEUS Analysis, Reconstruction and Trigger.

MSSM : The Minimal Supersymmetric extension to the Standard Model of particle physics.

NC : Neutral Current.

NWA : Narrow Width Approximation.

PDF : Parton Density Function.

PHYTIA : Monte Carlo simulation implementing a string model for hadronization.

PMT : Photomultiplier Tube.

QCD : Quantum Chromo-Dynamics.

QFT : Quantum Field Theory.

RCAL : Rear Calorimeter.

RMUON : Rear Muon chambers.

RTD : Rear Tracking Detector.

SM : Standard Model of particle physics.

SPYTHIA : Supersymmetric extension of PYTHIA simulating supersymmetric particles and their interactions.

SUSY : Supersymmetry.

SUSYGEN : Monte Carlo simulation for SUSY interactions at e^+e^- and ep colliders.

TLT : Third Level Trigger.

TLTZGANA : The offline TLT simulation.

TRD : Transition Radiation Detector.

TOE : Theory of Everything.

UCAL : Uranium Calorimeter.

VCTRAK : CTD Track reconstruction package.

ZEUS/$ZE\Upsilon\Sigma$**:** $Z\acute{\eta}\tau\eta\sigma\iota\varsigma\ \kappa\alpha\theta'\ E\upsilon\rho\epsilon\tau\acute{\eta}\varsigma\ \Upsilon\pi o\kappa\epsilon\iota\mu\acute{\epsilon}\nu\eta\varsigma\ \Sigma\upsilon\mu\mu\epsilon\tau\rho\acute{\iota}\alpha\varsigma$. From Greek meaning Search to Elucidate Underlying Symmetry.

Bibliography

[1] R. Galea. Exotic searches with the zeus detector. *Nucl. Phys.*, B79:162–165, 1999.

[2] R. Galea. Searches beyond the standard model at hera. Proceedings to the Lake Louise Winter Institute, February 2000.

[3] A.T.Doyle et. al., editor. *Proceedings of the Workshop on Monte Carlo Generators for HERA Physics*, 1998-1999.

[4] F. Abe et al. Evidence for top quark production in anti-p p collisions at $\sqrt{s} = 1.8$ tev. *Phys. Rev.*, D50:2966–3026, 1994.

[5] FERMILAB. Tau neutrino discovery. Press Release, No preprint yet available., July 2000.

[6] L3 ALEPH, DELPHI and OPAL Collaborations. Searches for higgs bosons:preliminary combined results using lep data collected at energies up to 209 gev. Submitted to ICHEP'2000, Osaka, Japan, July 27 - August 2 2000.

[7] The ATLAS collaboration. Detector and physics performance technical design report. LHCC 99-14/15.

[8] Yuichi Oyama. K2k (kek to kamioka) neutrino oscillation experiment at kek-ps. 1998.

[9] C. Caso et al. Review of particle physics. *Eur. Phys. J.*, C3:1–794, 1998.

[10] S. Glashow. *Nucl. Phys.*, 22:579, 1961.

[11] S. Weinberg. *Phys. Rev. Lett.*, 19:1264, 1967.

[12] A. Salam. *Elementary Particle Theory: Relativistic Groups and Analyticity.* Nobel Symposium No. 8, ed. N. Svartholm (Almqvist and Wiskell, Stockholm.

[13] W. de Boer. Grand unified theories and supersymmetry in particle physics and cosmology. *Prog. Part. Nucl. Phys.*, 33:201–302, 1994.

[14] J.A. Bagger, editor. *Supersymmetry, Supergravity and SuperColliders*, 1997.

[15] Stephen P. Martin. A supersymmetry primer. 1997.

[16] Xerxes Tata. What is supersymmetry and how do we find it? 1997.

[17] J.F. Gunion and H.E. Haber. *Nucl. Phys.*, B272:1, 1986.

[18] Manuel Drees and Stephen P. Martin. Implications of susy model building. 1995.

[19] Luis E. Ibanez and Graham G. Ross. Discrete gauge symmetries and the origin of baryon and lepton number conservation in supersymmetric versions of the standard model. *Nucl. Phys.*, B368:3–37, 1992.

[20] D. E. Groom et al. Review of particle physics. *Eur. Phys. J.*, C15:1, 2000.

[21] S. Aid et al. A search for squarks of rp-violating susy at hera. *Z. Phys.*, C71:211–226, 1996.

[22] J. Butterworth and H. Dreiner. R parity violation at hera. *Nucl. Phys.*, B397:3–34, 1993.

[23] W. Buchmuller, R. Ruckl, and D. Wyler. Leptoquarks in lepton quark collisions. *Phys. Lett.*, B191:442, 1987.

[24] A search for squarks of r-parity violating susy at hera. Contributed to 29th International Conference on High-Energy Physics (ICHEP 98), Vancouver, Canada, 23-29 Jul 1998.

[25] Wuji Liu. Search for resonances decaying to e+jet and limits on first generation leptoquarks in e^+p interactions at hera. ZEUS-Note 00-018.

[26] Keith A. Olive. Introduction to supersymmetry: Astrophysical and phenomenological constraints. 1999.

[27] Emanuelle Perez. *Recherche de Particules Supersymétriques dans l'expérience H1*. PhD thesis, Université Paris VI, 1996.

[28] E. Perez. Extension of the susygen package to supersymmetry at *ep* colliders. Prepared for Workshop on Monte Carlo Generators for HERA Physics (Plenary Starting Meeting), Hamburg, Germany, 27-30 Apr 1998.

[29] ZEUS Collaboration. Status of the detector: Status report 1993. Technical report, DESY, 1993.

[30] B. Wiik and G. Voss. *Ann. Rev. Nucl. Part. Sci.*, 32:335, 1982.

[31] N. Harnew et. al. *Nucl. Instrum. Methods*, A279:290, 1989.

[32] B. Foster et. al. *Nucl. Phys. (Proc. Suppl.)*, 32:181, 1993.

[33] B. Foster et. al. *Nucl. Instrum. Methods*, A338:254, 1994.

[34] F. Sauli. Principles of operation of multiwire proportional and drift chambers. CERN 77-09, 1977.

[35] R. Fernow. *Introduction to Experimental Particle Physics*. Cambridge University Press, New York.

[36] J. Breitweg et al. Measurement of high-q^2 charged-current e^+p deep inelastic scattering cross sections at hera. *Eur. Phys. J.*, C12:411, 2000.

[37] Paul de Jong. *The Measurement of the Hadronic Energy Flow and Jet Production with the ZEUS Calorimeter in Deep Inelastic Scattering Events at HERA*. PhD thesis, University of Amsterdam, 1993.

[38] M. Derrick et. al. *Nucl. Inst. Methods*, A309:77, 1991.

[39] A. Bernstein et. al. *Nucl. Inst. Methods*, A336:254, 1994.

[40] A. Caldwell et. al. *Nucl. Instrum. Methods*, A321:356, 1992.

[41] H. Abramowicz et al. Intercalibration of the zeus high resolution and backing calorimeters. *Nucl. Instrum. Meth.*, A313:126–134, 1992.

[42] G. Abbiendi et al. The zeus barrel and rear muon detector. *Nucl. Instrum. Meth.*, A333:342–354, 1993.

[43] H. Bethe and W. Heitler. *Proc. Roy. Soc.*, A146:83, 1934.

[44] M. Derrick et. al. *Z. Phys.*, C63:391, 1994.

[45] G. Hartner. Vctrak briefing: Program and math. ZEUS-Note 98-058.

[46] Frédéric Bénard et al. The 1995 tlt filter software. ZEUS-Note 95-164.

[47] D. Bandyopadhyay. Mutrig: A third level trigger muon finder. ZEUS-Note 93-013.

[48] G. Abbiendi et. al. ZEUS-Note 93-120.

[49] R.J. Teuscher. *Charm and Charm-Strange Hadron Production in ep Collisions at HERA as probes of Confinement*. PhD thesis, University of Toronto, 1997.

[50]

[51] R. Sinkus. A novel approach to error function minimization for feed forward neural networks. *Nucl. Instr. and Meth.*, A361:290–296, 1995.

[52] R. Sinkus and T. Voss. Particle identification with neural networks using a rotational invariant momentum representation. *Nucl. Instr. and Meth.*, A391:360–268, 1997.

[53]

[54] L. Sinclair. *Hard Diffractive Scattering in Photoproduction at HERA*. PhD thesis, McGill University, 1995.

[55] ACP Group. Branch bus specifications. FERMILAB (1987).

[56] *A FDDI based processor farm for the ZEUS Third Level Trigger*, 1997.

[57] R. Galea and A. Mirea. Zeus trigger parallel session. ZEUS Collaboration Meeting in Toronto, June 2000.

[58] W. Buchmuller and G. Ingelman, editors. *Proceedings of the workshop on the physics at HERA*, 1991.

[59] U. Amaldi, editor. *Proceedings of the study of an ep facility for Europe*, 1979.

[60] J. Biltzinger. Uranium calorimeter noise of 1994 data. ZEUS-Note 95-072.

[61] S. M. Wang. ZEUS-Note 96-121.

[62] A. Savin. ZEUS-Note 98-007.

[63] C. Catterall and F. Pelucchi. Comparison of ctd and calorimeter measurement of the dis positron angle in high q^2 events. ZEUS-Note 97-056.

[64] Ali Sabetfakhri. *A Search for Electron and Neutrino Compositeness in ep Collisions at HERA*. PhD thesis, University of Toronto, 2000.

[65] J. Labs. Calcorr. ZEUS Phantom library (1996).

[66] Kunihiro Nagano. *Measurement of Charged-Current e^+p Deep Inelastic Scattering Cross Sections at $\sqrt{s} = 300$ GeV*. PhD thesis, University of Tokyo, 1999.

[67] Gennady M. Briskin. *Diffractive Dissociation in ep Deep Inelastic Scattering*. PhD thesis, Tel Aviv University, 1998.

[68] J. Grosse-Knetter. Energy correction for islands. ZEUS-Note 97-039.

[69] J. Grosse-Knetter. Corrections for the hadronic final state. ZEUS-Note 98-031.

[70] A. López-Durán Viani and S. Schlenstedt. Electron finder efficiencies and impurities: A comparison between sinistra95, em and emnet. ZEUS-Note 99-077.

[71] S.D. Ellis and D.E. Soper. Successive combination jetalgorithm for hadron collisions. *Phys. Rev. D.*, 48(7):3160.

[72] Yu. L. Dokshitzer et. al. Better jet clustering algorithms. Cavendish-HEP-97/06.

[73] A. Kwiatkowski, H. Spiesberger, and H. J. Mohring. Heracles: An event generator for e p interactions at hera energies including radiative processes: Version 1.0. *Comp. Phys. Commun.*, 69:155–172, 1992.

[74] K. Charchula, G. A. Schuler, and H. Spiesberger. Combined qed and qcd radiative effects in deep inelastic lepton - proton scattering: The monte carlo generator django6. *Comput. Phys. Commun.*, 81:381–402, 1994.

[75] Leif Lonnblad. Ariadne version 4: A program for simulation of qcd cascades implementing the color dipole model. *Comput. Phys. Commun.*, 71:15, 1992.

[76] H. L. Lai et al. Improved parton distributions from global analysis of recent deep inelastic scattering and inclusive jet data. *Phys. Rev.*, D55:1280–1296, 1997.

[77] G. Marchesini et al. Herwig: A monte carlo event generator for simulating hadron emission reactions with interfering gluons. version 5.1 - april 1991. *Comput. Phys. Commun.*, 67:465–508, 1992.

[78] N. Ghodbane et. al. Susygen 2.0/0.6: A monte carlo event generator for mssm sparticle production for e^-e^-, $\mu^+\mu^-$ and ep colliders. http://lyoinfo.in2p3.fr/susygen/susygen3.html.

[79] Torbjorn Sjostrand. High-energy physics event generation with PYTHIA 5.7 and JETSET 7.4. *Comput. Phys. Commun.*, 82:74–90, 1994.

[80] A.T.Doyle et. al., editor. *Proceedings of the Workshop on Monte Carlo Generators for HERA Physics*, 1998-1999.

[81] R. Brun *et al.* Geant 3.13. CERN DD/EE/84-1 (1987).

[82] Els de Wolf (editor) *et al.* Zgana: Zeus trigger simulation library.

[83] J. Breitweg et. al. Search for resonances decaying to $e^+ - jet$ in e^+p interactions at hera. *European Physical Journal*, C16:253–267, 2000.

[84] J. Hart and the CTD group. private communication.

[85] ZEUS Collaboration. http://www-zeus.desy.de/žarah/phantom/phantom.html.

[86] D. Acosta et. al. A search for excited fermions in e^p collisions. ZEUS-Note 96-110.

[87] S. Schlenstedt and the LUMI group. http://www-zeus.desy.de/physics/lumi/.

[88] B. Mellado A. Caldwell, W. Liu and B. Straub. Bcal electron studies-part i:mc and test beam energy studies. ZEUS-Note 98-002.

[89] W. Liu A. Caldwell and B. Straub. Electron studies-part ii:energy scale calibration. ZEUS-Note 98-018.

[90] A. Meyer H.J. Grabosch and S. Schlenstedt. x_0 determination and electron energy correction with the presampler. ZEUS-Note 98-045.

[91] J. Breitweg et al. Search for selectron and squark production in e+ p collisions at hera. *Phys. Lett.*, B434:214–230, 1998.

[92] M. Derrick et al. Search for lepton flavor violation in e p collisions at 300-gev center of mass energy. *Z. Phys.*, C73:613–628, 1997.

[93] C. Adloff et al. A search for leptoquark bosons and lepton flavor violation in e+ p collisions at hera. *Eur. Phys. J.*, C11:447–471, 1999.

[94] The ALEPH Collaboration. Search for charginos and neutralinos in e+e- collisions at centre-of-mass energies near 183 gev and constraints on the mssm parameter space. *European Physical Journal*, C11:193–216, 1999.

[95] M. Hirsch, H. V. Klapdor-Kleingrothaus, and S. G. Kovalenko. New constraints on r parity broken supersymmetry from neutrinoless double beta decay. *Phys. Rev. Lett.*, 75:17, 1995.

[96] Herbi Dreiner. An introduction to explicit r-parity violation. 1997.

[97] B. Abbott et al. Search for first generation scalar leptoquark pairs in p anti-p collisions at $\sqrt{s} = 1.8$ tev. *Phys. Rev. Lett.*, 80:2051–2056, 1998.

[98] F. Abe et al. Search for first generation leptoquark pair production in p anti-p collisions $\sqrt{s} = 1.8$ tev. *Phys. Rev. Lett.*, 79:4327, 1997.

[99] H1 Collaboration. A search for squarks of r-parity violating susy at hera. Submitted to ICHEP'2000, Osaka, Japan, July 27 - August 2 2000.

[100] J. Breitweg et. al. *Euro. Phys. J.*, C3:27, 427.